University of Nevada, Reno

Ab initio molecular dynamics simulations of lanthanide coordination structures in water and in faujasite

A dissertation submitted in partial fulfillment of the requirements for the degree of

Doctor of Philosophy in Chemical Engineering

By

Richard C Shiery

Dr. David C. Cantu/Dissertation Advisor

December, 2022

THE GRADUATE SCHOOL

We recommend that the dissertation
prepared under our supervision by

Richard C. Shiery

entitled

Ab initio molecular dynamics simulations of lanthanide coordination structures in water and in faujasite

be accepted in partial fulfillment of the
requirements for the degree of

Doctor of Philosophy

David Cantu, Ph.D.
Advisor

Ana de Bettencourt-Dias, Ph.D.
Committee Member

Vaidyanathan Subramanian, Ph.D.
Committee Member

Victor Vasquez, Ph.D.
Committee Member

Sergey Varganov, Ph.D.
Graduate School Representative

Markus Kemmelmeier, Ph.D., Dean
Graduate School

December, 2022

Abstract

Atomic and molecular resolution can provide unique insights into the ambiguous mechanisms by which lanthanum increases the hydrothermal stability of faujasite in cracking catalysts, as well as in cation exchange in faujasite. The structures of the lanthanide aqua ions were resolved with density functional theory calculations and *ab initio* molecular dynamics (AIMD) simulations within ~0.05 Å of experimental results. Reaction energies were quantified by predicting the first hydrolysis constant of lanthanide aqua ions within ~1.1 pK_a units using AIMD with rare event simulation techniques and electronic structure calculations. The capture of structural and reaction trends in the lanthanide aqua ion served as a benchmark for implementing similar methods in lanthanum-exchanged faujasite. In faujasite, AIMD simulation identified the preferred binding site of lanthanum. AIMD with a rare event simulation technique was used to quantity the free energy of faujasite aluminum tetrahedra deprotonation, with and without lanthanum exchanged in faujasite. The presence of lanthanum makes faujasite deprotonation energetically more favorable, thus making faujasite less hydrophilic. The local structure of water confined in faujasite was simulated with AIMD. The model faujasite structure was modified to produce a series of systems to study the influence of confinement, hydrophilicity, and cation exchanged on the local structure of water as quantified from radial distribution functions. Increases in hydrophilicity in hydrogen-exchanged faujasite disrupts the confined water structure. While lanthanum ions compensate for a larger magnitude of charge, equivalent number of sodium ions have a higher probability of occupying sites interacting with the supercage and thus disrupt the local structure of water more significantly than lanthanum.

Acknowledgments

I express my sincerest gratitude to Dr. David Cantu for his guidance and tutelage that culminated with the contributions detailed in this dissertation. The value of the mentorship he provided cannot be fully expressed in words. His patience is matched by his commitment to scientific excellence.

I extend my thanks to the members of my committee, Dr. Ana de Bettencourt-Dias, Dr. Vaidyanathan Ravi Subramanian, Dr. Sergey Varganov, and Dr. Victor Vasquez for their expertise and for challenging me to strive further within my field of research.

I would like to acknowledge Dr. John Kenney, whose unrivaled passion and enthusiasm for chemistry and physics serves as an inspiration for countless students, of which I consider myself to be lucky to be included as one.

I would like to thank Dr. John Fulton for his support and many collaborations as detailed in this dissertation.

I would like to thank Caio Cesar De Carvalho, Danil Kaliakin, Gerra Licup, Jesus Diaz Sanchez, Ravi O'Brien, Thomas Summers and Tim Mott. I could not ask for better colleagues to share a lab with.

Table of Contents

List of Tables

List of Figures

CHAPTER 1

Introduction

The lanthanide elements are essential in a myriad of technologies, such as catalysts,[1–6] medical contrast agents,[7–9] luminescent materials,[10–15] and single molecular magnets.[16,17] However, for most applications, lanthanides must be separated and purified.[18–28] Their important uses resulted in selected lanthanides to be listed as critical materials,[29,30] meaning the supply of lanthanides has the potential to impact the economies of nations that relay on importing them while having a low rate of reclaiming said materials. The chemical similarity of elements in the lanthanide series results in challenges during separations, as lanthanide-lanthanide separation and lanthanide-actinide separation remains a critical area of research since lanthanides occur together in nature, alongside actinides such as uranium and thorium.[31,32]

Lanthanide (Ln) ions have a common oxidization state of +3 and have large coordination spheres, with eight or nine coordination sites. The lighter lanthanide aqua ions are most commonly nine-coordinate, while the heavier are eight-coordinate. The middle lanthanides can have a coordination number between eight and nine. Lanthanide ions are reactive and they form ionic coordination bonds.[33] Increased reactivity causes lanthanide ions to form hydroxide and oxide bridges in aqueous solution,[34] which occurs when one of hydrogen atoms of the Ln aqua ion is removed, leading to a reaction with neighboring hydroxide. By exploiting the hydrolysis constant, a pK_a in water, one can target lanthanides to precipitate out. These characteristics are shared between the lanthanides and the actinides after plutonium.[35,36]

Ion exchange is a separation technique in which a porous material adsorbs particular ions from solution. The adsorption of lanthanides is of special interest in the case of lanthanum-exchanged faujasite (FAU), which is a key component of petroleum cracking catalysts.

Faujasite is a zeolite that has applications as a catalyst, molecular sieve, adsorbent, and ion exchanger. The applications of FAU as an ion exchanger range from the separation of radioactive elements from nuclear waste[37] to the removal of conventional heavy metal contaminants[38,39] and separations of rare earth metals.[40–44] Lanthanum has been exchanged into faujasite for decades as a part of fluid cracking catalyst to improve its hydrothermal stability, as faujasite is the principal catalytic component.[45,46] Cracking operates under harsh steam and heat conditions, which leads to the destabilization of the zeolite via the removal of structural aluminum by dealumination.[47–49] The destabilization of fluid cracking catalysts limits the lifetime of the catalyst and is a significant contributor to the production of gasoline.[50,51] The exchange of lanthanum into faujasite decreases dealumination in FAU,[2,39,52,53] yet the exact mechanism remains ambiguous. A potential mechanism is that lanthanum increases activation energy of dealumination reaction in faujasite.[3] Alternatively, other cations have been examined to hinder dealumination in similar zeolites.[54]

The effect of lanthanum in faujasite stability must be accounted for in terms of changes to the chemical properties of the zeolite, chiefly Brønsted acidity. The aluminum tetrahedra of hydrogen-exchanged faujasite provide Brønsted acid sites, which in turn provide the zeolite with catalytic acidity.[55–60] Yet, dealumination reactions also begin at the Brønsted acid sites.[61] As a result, to properly model lanthanum in faujasite, both the

structure and reactions must be quantified. An overview of the Methods used in this work: density functional theory (DFT) calculations, *ab initio* molecular dynamics (AIMD) simulations, electronic structure calculations, and X-ray absorption spectroscopy, is presented in Chapter 2.

The solution structures of the lanthanide aqua ions are well characterized[62–68] and provide a reliable benchmark to develop a computational protocol, based on AIMD simulations, for predicting the coordination structures in solution of all Ln ions. Chapter 3 describes the computational protocol, how experimental and predicted extended X-ray absorption fine structure (EXAFS) spectra were compared, as well as results that show agreement with experiment. Further, Chapter 4 demonstrates how the coordination structures of the lanthanide aqua ions vary with temperature, also using AIMD simulations and EXAFS measurements.

Beyond solution structures, the modeling of lanthanides in porous materials required thermodynamic properties, such as reaction energies, to be accounted for to accurately predict the properties of the zeolite. Lanthanide aqua ions undergo hydrolysis reactions, which is coordinated water molecules forming the hydroxide. The first, second, and third acidity constants of the lanthanide aqua ions are well characterized,[69–71] and provide a reliable benchmark to develop a computational protocol to calculate absolute and relative reaction energies. Chapter 5 describes the prediction of absolute values of the first Ln acidity constants using AIMD couples with a rare event simulation technique, and the quantification of the second and third Ln acidity constants from relative energies from electronic structure calculations.

With a computational approach with the ability to replicate Ln coordination structures and reaction energies, the binding of water and lanthanum ions in faujasite is determined to obtain insights on how lanthanum stabilizes faujasite. Chapter 6 describes how water molecules, which play a key role in dealumination, bind on hydrogen-exchanged faujasite on aluminum tetrahedra, and how lanthanum-exchange affects the Brønsted acidity of faujasite. Results are discussed in the context of the hydrothermal stability of lanthanum-exchanged faujasite as a cracking catalyst, where steam is present.

In the context of zeolites as ion exchangers, the structure of liquid water in faujasite is described in Chapter 7. The effect of the aluminum content in hydrogen-exchanged faujasite on the structure of water, as well as that of which cation is exchanged (sodium and lanthanum) is quantified. Finally, overall conclusions are presented in Chapter 8.

Chapter 1 References

(1) Rosid, S. J. M.; Toemen, S.; Iqbal, M. M. A.; Bakar, W. A. W. A.; Mokhtar, W. N. A. W.; Aziz, M. M. A. Overview Performance of Lanthanide Oxide Catalysts in Methanation Reaction for Natural Gas Production. *Environ. Sci. Pollut. Res.* **2019**, *26* (36), 36124–36140. https://doi.org/10.1007/s11356-019-06607-8.

(2) Roelofsen, W.; Mathies, H.; De Groot, R. L.; Van Woerkom, P. C. M.; Angad Gaur, H. Effect of Rare Earth Loading in Y-Zeolite on Its Dealumination during Thermal Treatment. In *Studies in Surface Science and Catalysis*; Elsevier Inc., 1986; Vol. 28, pp 337–344. https://doi.org/10.1016/S0167-2991(09)60891-0.

(3) Louwen, J. N.; Simko, S.; Stanciakova, K.; Bulo, R. E.; Weckhuysen, B. M.; Vogt, E. T. C. Role of Rare Earth Ions in the Prevention of Dealumination of Zeolite y for Fluid Cracking Catalysts. *J. Phys. Chem. C* **2020**, *124* (8), 4626–4636. https://doi.org/10.1021/acs.jpcc.9b11956.

(4) Cheng, Y.; Nan, H.; Li, Q.; Luo, Y.; Chu, K. A Rare-Earth Samarium Oxide Catalyst for Electrocatalytic Nitrogen Reduction to Ammonia. *ACS Sustain. Chem. Eng.* **2020**, *8* (37), 13908–13914. https://doi.org/10.1021/acssuschemeng.0c05764.

(5) Mikami, K.; Terada, M.; Matsuzawa, H. "Asymmetric" Catalysis by Lanthanide Complexes. *Angew. Chemie - Int. Ed.* **2002**, *41* (19), 3554–3572. https://doi.org/10.1002/1521-3773(20021004)41:19<3554::aid-anie3554>3.0.co;2-p.

(6) Yu, X.; Seo, S. Y.; Marks, T. J. Effective, Selective Hydroalkoxylation/Cyclization of Alkynyl and Allenyl Alcohols Mediated by Lanthanide Catalysts. *J. Am. Chem. Soc.* **2007**, *129* (23), 7244–7245. https://doi.org/10.1021/ja071707p.

(7) Raymond, K. N.; Pierre, V. C. Next Generation, High Relaxivity Gadolinium MRI Agents. *Bioconjug. Chem.* **2005**, *16* (1), 3–8. https://doi.org/10.1021/bc049817y.

(8) Thiele, N. A.; Woods, J. J.; Wilson, J. J. Implementing F-Block Metal Ions in Medicine: Tuning the Size Selectivity of Expanded Macrocycles. *Inorg. Chem.* **2019**, *58* (16), 10483–10500. https://doi.org/10.1021/acs.inorgchem.9b01277.

(9) Molloy, J. K.; Nonat, A. M.; O'Brien, J. E.; Brougham, D. F.; Gunnlaugsson, T. Self-Assembled Ln(III) Cyclen-Based Micelles and AuNPs Conjugates as Candidates for Luminescent and Magnetic Resonance Imaging (MRI) Agents. *Supramol. Chem.* **2020**, *0* (0), 1–10. https://doi.org/10.1080/10610278.2020.1742912.

(10) De Bettencourt-Dias, A. Lanthanide-Based Emitting Materials in Light-Emitting Diodes. *J. Chem. Soc. Dalt. Trans.* **2007**, No. 22, 2229–2241. https://doi.org/10.1039/b702341c.

(11) Eliseeva, S. V.; Bünzli, J. C. G. Lanthanide Luminescence for Functional Materials and Bio-Sciences. *Chem. Soc. Rev.* **2010**, *39* (1), 189–227. https://doi.org/10.1039/b905604c.

(12) Binnemans, K. Lanthanide-Based Luminescent Hybrid Materials. *Chem. Rev.* **2009**, *109* (9), 4283–4374. https://doi.org/10.1021/cr8003983.

(13) Monteiro, J. H. S. K.; De Bettencourt-Dias, A.; Sigoli, F. A. Estimating the Donor-Acceptor Distance to Tune the Emission Efficiency of Luminescent Lanthanide

Compounds. *Inorg. Chem.* **2017**, *56* (2), 709–712. https://doi.org/10.1021/acs.inorgchem.6b02637.

(14) Zanoni, K. P. S.; Ravaro, L. P.; De Camargo, A. S. S. Host-Guest Luminescent Materials Based on Highly Emissive Species Loaded into Versatile Sol-Gel Hosts. *Dalt. Trans.* **2018**, *47* (37), 12813–12826. https://doi.org/10.1039/c8dt02086h.

(15) Wang, J.; Suffren, Y.; Daiguebonne, C.; Freslon, S.; Bernot, K.; Calvez, G.; Le Pollès, L.; Roiland, C.; Guillou, O. Multi-Emissive Lanthanide-Based Coordination Polymers for Potential Application as Luminescent Bar-Codes. *Inorg. Chem.* **2019**, *58* (4), 2659–2668. https://doi.org/10.1021/acs.inorgchem.8b03277.

(16) Kitchen, J. A. Lanthanide-Based Self-Assemblies of 2,6-Pyridyldicarboxamide Ligands: Recent Advances and Applications as next-Generation Luminescent and Magnetic Materials. *Coord. Chem. Rev.* **2017**, *340*, 232–246. https://doi.org/10.1016/j.ccr.2017.01.012.

(17) Woodru, D. N.; Winpenny, R. E. P.; Lay, R. A. Lanthanide Single-Molecule Magnets. **2013**.

(18) Kronholm, B.; Anderson, C. G.; Taylor, P. R. A Primer on Hydrometallurgical Rare Earth Separations. *Jom* **2013**, *65* (10), 1321–1326. https://doi.org/10.1007/s11837-013-0718-9.

(19) Ferru, G.; Reinhart, B.; Bera, M. K.; Olvera De La Cruz, M.; Qiao, B.; Ellis, R. J. The Lanthanide Contraction beyond Coordination Chemistry. *Chem. - A Eur. J.* **2016**, *22* (20), 6899–6904. https://doi.org/10.1002/chem.201601032.

(20) Hall, G. B.; Holfeltz, V. E.; Campbell, E. L.; Boglaienko, D.; Lumetta, G. J.; Levitskaia, T. G. Evolution of Acid-Dependent Am3+ and Eu3+ Organic Coordination Environment: Effects on the Extraction Efficiency. *Inorg. Chem.* **2020**, *59* (7), 4453–4467. https://doi.org/10.1021/acs.inorgchem.9b03612.

(21) Qiao, B.; Muntean, J. V.; Olvera De La Cruz, M.; Ellis, R. J. Ion Transport Mechanisms in Liquid-Liquid Interface. *Langmuir* **2017**, *33* (24), 6135–6142. https://doi.org/10.1021/acs.langmuir.7b01230.

(22) Baldwin, A. G.; Ivanov, A. S.; Williams, N. J.; Ellis, R. J.; Moyer, B. A.; Bryantsev, V. S.; Shafer, J. C. Outer-Sphere Water Clusters Tune the Lanthanide Selectivity of Diglycolamides. *ACS Cent. Sci.* **2018**, *4* (6), 739–747. https://doi.org/10.1021/acscentsci.8b00223.

(23) Nakase, M.; Kobayashi, T.; Shiwaku, H.; Suzuki, S.; Grimes, T. S.; Mincher, B. J.; Yaita, T. Relationship Between Structure and Coordination Strength of N and N,O-Hybrid Donor Ligands with Trivalent Lanthanides. *Solvent Extr. Ion Exch.* **2018**, *36* (7), 633–646. https://doi.org/10.1080/07366299.2018.1532137.

(24) Werner, E. J.; Biros, S. M. Supramolecular Ligands for the Extraction of Lanthanide and Actinide Ions. *Inorg. Chem. Front.* **2019**, *6* (12), 2067–2094. https://doi.org/10.1039/c9qo00242a.

(25) Healy, M. R.; Ivanov, A. S.; Karslyan, Y.; Bryantsev, V. S.; Moyer, B. A.; Jansone-Popova, S. Efficient Separation of Light Lanthanides(III) by Using Bis-Lactam Phenanthroline Ligands. *Chem. - A Eur. J.* **2019**, *25* (25), 6326–6331. https://doi.org/10.1002/chem.201806443.

(26) Cheisson, T.; Schelter, E. J. Rare Earth Elements: Mendeleev's Bane, Modern

Marvels. *Science (80-.).* **2019**, *363* (6426), 489–493. https://doi.org/10.1126/science.aau7628.

(27) Cotruvo, J. A. The Chemistry of Lanthanides in Biology: Recent Discoveries, Emerging Principles, and Technological Applications. *ACS Cent. Sci.* **2019**, *5* (9), 1496–1506. https://doi.org/10.1021/acscentsci.9b00642.

(28) Liang, Z.; Bu, W.; Schweighofer, K. J.; Walwark, D. J.; Harvey, J. S.; Hanlon, G. R.; Amoanu, D.; Erol, C.; Benjamin, I.; Schlossman, M. L. Nanoscale View of Assisted Ion Transport across the Liquid–Liquid Interface. *Proc. Natl. Acad. Sci. U. S. A.* **2019**, *116* (37), 18227–18232. https://doi.org/10.1073/pnas.1701389115.

(29) Bauer, D.; Diamond, D.; Li, J.; Sandalow, D.; Telleen, P.; Wanner, B. US Department of Energy: Critical Materials Strategy, December 2010. *Agenda. https://doi. org/10.2172/1000846* **2010**.

(30) Massari, S.; Ruberti, M. Rare Earth Elements as Critical Raw Materials: Focus on International Markets and Future Strategies. *Resour. Policy* **2013**, *38* (1), 36–43. https://doi.org/10.1016/j.resourpol.2012.07.001.

(31) Amer, T. E.; El-Sheikh, E. M.; Gado, M. A.; Abu-Khoziem, H. A.; Zaki, S. A. Selective Recovery of Lanthanides, Uranium and Thorium from Rosetta Monazite Mineral Concentrate. *Sep. Sci. Technol.* **2018**, *53* (10), 1522–1530. https://doi.org/10.1080/01496395.2017.1405039.

(32) Gupta, B.; Malik, P.; Deep, A. Extraction of Uranium, Thorium and Lanthanides Using Cyanex-923: Their Separations and Recovery from Monazite. *J. Radioanal. Nucl. Chem.* **2002**, *251* (3), 451–456. https://doi.org/10.1023/A:1014890427073.

(33) Cotton, S. A. Lanthanides: Comparison to 3d Metals. In *Encyclopedia of Inorganic and Bioinorganic Chemistry*; American Cancer Society, 2012. https://doi.org/10.1002/9781119951438.eibc2013.

(34) Housecroft, C. E.; Sharpe, A. G. *Inorganic Chemistry*, Second.; Pearson Education Limited, 2005.

(35) Choppin, G. R. Structure and Thermodynamics of Lanthanide and Actinide Complexes in Solution. *Pure Appl. Chem.* **1971**, *27* (1–2), 23–42. https://doi.org/10.1351/pac197127010023.

(36) Seth, M.; Schwerdtfeger, P.; Dolg, M.; Fulde, P. Lanthanide and Actinide Contractions: Relativistic and Shell Structure Effects. *J. Am. Chem. Soc.* **1995**, *117* (24), 6597–6598. https://doi.org/10.1021/ja00129a026.

(37) Gu, B. X.; Wang, L. M.; Ewing, R. C. Effect of Amorphization on the Cs Ion Exchange and Retention Capacity of Zeolite-NaY. *J. Nucl. Mater.* **2000**, *278* (1), 64–72. https://doi.org/10.1016/S0022-3115(99)00224-X.

(38) Mekatel, H.; Amokrane, S.; Benturki, A.; Nibou, D. Treatment of Polluted Aqueous Solutions by Ni 2+, Pb 2+, Zn 2+, Cr +6, Cd +2 and Co +2 Ions by Ion Exchange Process Using Faujasite Zeolite. *Procedia Eng.* **2012**, *33* (2011), 52–57. https://doi.org/10.1016/j.proeng.2012.01.1176.

(39) Woltermann, G. M.; Magee, J. S.; Griffith, S. D. Chapter 4 Commercial Preparation and Characterization of FCC Catalysts. In *Fluid Catalytic Cracking: Science and Technology*; Magee, J. S., Mitchell, M. M. B. T.-S. in S. S. and C., Eds.; Elsevier, 1993; Vol. 76, pp 105–144. https://doi.org/https://doi.org/10.1016/S0167-2991(08)63827-6.

(40) Zuyi, T.; Quanchang, L. Studies on Ion Exchange Equilibria and Kinetics VII. Tb3+-Na§ Cation Exchange Equilibria and Kinetics in Zeolite-Y. **1997**, *223*, 173–176.
(41) Shy, D. S.; Chen, S. H.; Lievens, J.; Liu, S. Bin; Chao, K. J. Distribution of Cations in Lanthanum-Exchanged NaY Zeolites. *J. Chem. Soc. Faraday Trans.* **1991**, *87* (17), 2855–2859. https://doi.org/10.1039/FT9918702855.
(42) Rees, L. V. C.; Zuyi, T. Rare-Earth Ion Exchange in Zeolite Y. **1986**, *6* (July 1985), 201–205.
(43) Chen, S. H.; Chao, K. J.; Lee, T. Y. Lanthanum-NaY Zeolite Ion Exchange. 1. Thermodynamics and Thermochemistry. *Ind. Eng. Chem. Res.* **1990**, *29* (10), 2020–2023. https://doi.org/10.1021/ie00106a007.
(44) Sherry, H. S. Cation Exchange on Zeolites. **1974**, 350–379.
(45) Sie, S. T. Past, Present and Future Role of Microporous Catalysts in the Petroleum Industry. In *Advanced Zeolite Science and Applications*; Jansen, J. C., Stöcker, M., Karge, H. G., Weitkamp, J. B. T.-S. in S. S. and C., Eds.; Elsevier, 1994; Vol. 85, pp 587–631. https://doi.org/https://doi.org/10.1016/S0167-2991(08)60779-X.
(46) Groen, J. C.; Peffer, L. A. A.; Moulijn, J. A.; Pérez-Ramírez, J. Mesoporosity Development in ZSM-5 Zeolite upon Optimized Desilication Conditions in Alkaline Medium. *Colloids Surfaces A Physicochem. Eng. Asp.* **2004**, *241* (1), 53–58. https://doi.org/https://doi.org/10.1016/j.colsurfa.2004.04.012.
(47) Silaghi, M. C.; Chizallet, C.; Sauer, J.; Raybaud, P. Dealumination Mechanisms of Zeolites and Extra-Framework Aluminum Confinement. *J. Catal.* **2016**, *339*, 242–255. https://doi.org/10.1016/j.jcat.2016.04.021.
(48) Ravenelle, R. M.; Schübler, F.; Damico, A.; Danilina, N.; Van Bokhoven, J. A.; Lercher, J. A.; Jones, C. W.; Sievers, C. Stability of Zeolites in Hot Liquid Water. *J. Phys. Chem. C* **2010**, *114* (46), 19582–19595. https://doi.org/10.1021/jp104639e.
(49) Malola, S.; Svelle, S.; Bleken, F. L.; Swang, O. Detailed Reaction Paths for Zeolite Dealumination and Desilication From Density Functional Calculations. *Angew. Chemie Int. Ed.* **2012**, *51* (3), 652–655. https://doi.org/https://doi.org/10.1002/anie.201104462.
(50) Vogt, E. T. C.; Weckhuysen, B. M. Fluid Catalytic Cracking: Recent Developments on the Grand Old Lady of Zeolite Catalysis. *Chem. Soc. Rev.* **2015**, *44* (20), 7342–7370. https://doi.org/10.1039/C5CS00376H.
(51) Cerqueira, H. S.; Caeiro, G.; Costa, L.; Ramôa Ribeiro, F. Deactivation of FCC Catalysts. *J. Mol. Catal. A Chem.* **2008**, *292* (1–2), 1–13. https://doi.org/10.1016/j.molcata.2008.06.014.
(52) Akah, A. Application of Rare Earths in Fluid Catalytic Cracking: A Review. *J. Rare Earths* **2017**, *35* (10), 941–956. https://doi.org/10.1016/S1002-0721(17)60998-0.
(53) Zhang, L.; Qin, Y.; Zhang, X.; Gao, X.; Song, L. Further Findings on the Stabilization Mechanism among Modified y Zeolite with Different Rare Earth Ions. *Ind. Eng. Chem. Res.* **2019**, *58* (31), 14016–14025. https://doi.org/10.1021/acs.iecr.9b03036.
(54) Sun, J.; Fang, H.; Ravikovitch, P. I.; Sholl, D. S. Understanding Dealumination

Mechanisms in Protonic and Cationic Zeolites. *J. Phys. Chem. C* **2020**. https://doi.org/10.1021/acs.jpcc.9b09693.

(55) Noda, T.; Suzuki, K.; Katada, N.; Niwa, M. Combined Study of IRMS-TPD Measurement and DFT Calculation on Brønsted Acidity and Catalytic Cracking Activity of Cation-Exchanged Y Zeolites. *J. Catal.* **2008**, *259*.

(56) Xu, T.; Munson, E. J.; Haw, J. F. Toward a Systematic Chemistry of Organic Reactions in Zeolites: In Situ NMR Studies of Ketones. *J. Am. Chem. Soc.* **1994**, *116* (5), 1962–1972. https://doi.org/10.1021/ja00084a041.

(57) Arora, S. S.; Nieskens, D. L. S.; Malek, A.; Bhan, A. Lifetime Improvement in Methanol-to-Olefins Catalysis over Chabazite Materials by High-Pressure H2 Co-Feeds. *Nat. Catal.* **2018**, *1* (9), 666–672. https://doi.org/10.1038/s41929-018-0125-2.

(58) Koehle, M.; Zhang, Z.; Goulas, K. A.; Caratzoulas, S.; Vlachos, D. G.; Lobo, R. F. Acylation of Methylfuran with Brønsted and Lewis Acid Zeolites. *Appl. Catal. A Gen.* **2018**, *564*, 90–101. https://doi.org/https://doi.org/10.1016/j.apcata.2018.06.005.

(59) Ravi, M.; Sushkevich, V. L.; Knorpp, A. J.; Newton, M. A.; Palagin, D.; Pinar, A. B.; Ranocchiari, M.; van Bokhoven, J. A. Misconceptions and Challenges in Methane-to-Methanol over Transition-Metal-Exchanged Zeolites. *Nat. Catal.* **2019**, *2* (6), 485–494. https://doi.org/10.1038/s41929-019-0273-z.

(60) Li, S.; Zheng, A.; Su, Y.; Zhang, H.; Chen, L.; Yang, J.; Ye, C.; Deng, F. Brønsted/Lewis Acid Synergy in Dealuminated HY Zeolite: A Combined Solid-State NMR and Theoretical Calculation Study. *J. Am. Chem. Soc.* **2007**, *129* (36), 11161–11171. https://doi.org/10.1021/ja072767y.

(61) Kühl, G. H. The Coordination of Aluminum and Silicon in Zeolites as Studied by X-Ray Spectrometry. *J. Phys. Chem. Solids* **1977**, *38* (11), 1259–1263. https://doi.org/https://doi.org/10.1016/0022-3697(77)90025-7.

(62) Habenschuss, A.; Spedding, F. H. The Coordination (Hydration) of Rare Earth Ions in Aqueous Chloride Solutions from x-Ray Diffraction. III. SmCl3, EuCl3, and Series Behavior. *J. Chem. Phys.* **1980**, *73* (1), 442–450. https://doi.org/10.1063/1.439895.

(63) Habenschuss, A.; Spedding, F. H. The Coordination (Hydration) of Rare Earth Ions in Aqueous Chloride Solutions from x-Ray Diffraction. I. TbCI3, DyCI3, ErCI3, TmCI3, and LuCI3. *J. Chem. Phys.* **1979**, *70* (6), 2797–2806. https://doi.org/10.1063/1.437866.

(64) Habenschuss, A.; Spedding, F. H. The Coordination (Hydration) of Rare Earth Ions in Aqueous Chloride Solutions from x-Ray Diffraction. II. LaCI3, PrCI3, and NdCI3. *J. Chem. Phys.* **1979**, *70* (8), 3758–3763. https://doi.org/10.1063/1.437928.

(65) Persson, I.; D'Angelo, P.; De Panfilis, S.; Sandström, M.; Eriksson, L. Hydration of Lanthanoid(III) Ions in Aqueous Solution and Crystalline Hydrates Studied by EXAFS Spectroscopy and Crystallography: The Myth of the "Gadolinium Break." *Chem. - A Eur. J.* **2008**, *14* (10), 3056–3066. https://doi.org/10.1002/chem.200701281.

(66) D'Angelo, P.; Zitolo, A.; Migliorati, V.; Chillemi, G.; Duvail, M.; Vitorge, P.; Abadie, S.; Spezia, R. Revised Ionic Radii of Lanthanoid(III) Ions in Aqueous

Solution. *Inorg. Chem.* **2011**, *50* (10), 4572–4579. https://doi.org/10.1021/ic200260r.

(67) Yamaguchi, T.; Nomura, M.; Wakita, H.; Ohtaki, H. An Extended X-Ray Absorption Fine Structure Study of Aqueous Rare Earth Perchlorate Solutions in Liquid and Glassy States. *J. Chem. Phys.* **1988**, *89* (8), 5153–5159. https://doi.org/10.1063/1.455633.

(68) Allen, P. G.; Bucher, J. J.; Shuh, D. K.; Edelstein, N. M.; Craig, I. Coordination Chemistry of Trivalent Lanthanide and Actinide Ions in Dilute and Concentrated Chloride Solutions. *Inorg. Chem.* **2000**, *39* (3), 595–601. https://doi.org/10.1021/ic9905953.

(69) Guillaumont, R.; Desire, B.; Galin, M. Première Constante d'hydrolyse Des Lanthanides. *Radiochem. Radioanal. Lett* **1971**, *8* (3), 189–197.

(70) Yakubovich, Y. Y.; Alekseev, V. G. Hydrolysis Constants of Tervalent Lanthanum and Lanthanide Ions in 0.1 M KNO3 Solution. *Russ. J. Inorg. Chem.* **2012**, *57* (6), 911–915. https://doi.org/10.1134/S0036023612060265.

(71) Nazarenko, V. A.; Antonovich, V. P.; Nevskaya, E. M. Hydrolysis of Metal Ions in Dilute Solutions. *Moscow At.* **1979**.

CHAPTER 2

Overview of Methods

2.1 Synopsis

The prediction of physical and chemical properties is the goal of computational models; molecular resolution provides a unique advantage in the investigation of chemical phenomena such as the structure of lanthanide ions in porous materials, in which experimental probes would be difficult to implement. The structures of the lanthanide aqua ions, and of water in cation-exchanged faujasite (FAU), were quantified using *ab initio* molecular dynamics (AIMD) simulations and density functional theory (DFT) calculations. The AIMD simulations relied on the system reaching equilibrium and sampling the equilibrated trajectory to obtain average properties. From the equilibrated frames, radial distribution functions (RDF) were used to calculate the simulation-averaged distances between atoms, such as the average lanthanide - oxygen distance for the aqua ions and the average distance between the oxygen atoms of water molecules of the water confined in faujasite.

Extended X-ray absorption fine structure (EXAFS) spectra were generated from equilibrated frames to sample the conformations of the lanthanide aqua ions in solution. The predicted spectra from AIMD simulations were compared directly to experimental EXAFS as a means of verifying simulation with experiment. Experimental EXAFS spectra are generated by using X-rays to excite a photoelectron from an atom, the photoelectron is then scattered, and the spectra is a measurement of the scattering due to

the local environment. The distances between atoms for a given frame of a simulation can be used to generated EXAFS spectra via the EXAFS equation.

The quantification of chemical reaction energies required techniques beyond those implemented to quantify the structural aspects of lanthanides and faujasite. Bluemoon rare event sampling enabled the use of reaction coordinates to study specific reactions, such as the deprotonation of hydrogen-exchanged faujasite. The distance of the oxygen - hydrogen bond was constrained, and through a series of constrained AIMD simulations, an average force on that constraint was calculated, effectively modeling the deprotonation of either the lanthanide aqua ion or faujasite. The integration of the average force on the constraint produced a potential of mean force, from which the free energy is obtained.

Electronic structure calculations with relativistic effects were done for single point energies for the lanthanide aqua ion species that occur during the first, second and third hydrolysis. All electron calculations have higher computational costs but have higher accuracy to quantify thermodynamic properties.

2.2 Approach for structures in solution and porous materials: DFT and AIMD

Ab initio molecular dynamics simulations is an approach that can accurately model reactions of lanthanides in the condensed phase. It was used to study the hydrolysis reactions of lanthanide complexes, relevant as the formation of hydroxyl groups ultimately lead to lanthanides to precipitate out of solution.[1] The stability of lanthanide complexes are sensitive to changes in protonation,[2] which must be taken in account for medical contrast agents,[3,4] enzymatic reactions[5–8] and catalysts such as faujasite.

For lanthanide-containing systems, the results of AIMD simulations and DFT calculations depended on the accuracy of the lanthanide pseudopotentials and basis sets (LnPP1), which are Goedecker-Tetter-Hutter-type pseudopotentials optimized in a mixed Gaussian and plane wave scheme.[9] The LnPP1 pseudopotentials and basis sets that were utilized in the upcoming Chapters were benchmarked with redox reactions, the most stringent metric for transferability of basis sets.[10] The valence *f* electrons were uncontracted in the basis set. The LnPP1 pseudopotentials and basis sets were optimized using the PBE functional, which has acceptable accuracy for resolving solution structures of lanthanide containing systems with a reduced computational cost.[11] Electronic structure calculations with lanthanides are more accurate;[12] however, they lack periodicity and the required length scale and cannot be used to model solutions with explicit solvent molecules or extended material structures. Periodic conditions were required to study faujasite, as it enabled bulk properties, such as the effect of acidity on a zeolite.

The LnPP1 pseudopotential and basis sets were used to predict the structure of lanthanide aqua ions. DFT calculation and AIMD simulations were done using CP2K.[13] The PBE functional was utilized, core electrons were modeled with the GTH-pseudopotentials, valence electrons were modeled with a polarizable double zeta basis sets, LnPP1 was used for lanthanides, and van der Waals interactions were accounted for using Grimme's D3 correction. The AIMD simulation box was a cubic, periodic system containing a lanthanide ion in the +III oxidation state, three chloride anions, and explicit water molecules at different temperatures. Following a simulated annealing protocol, AIMD simulations were performed and analyzed to obtain RDFs, angle distribution

functions (ADF), root mean square deviations (RMSD) compared to ideal geometries, and EXAFS spectra.

The first peak of a lanthanide-oxygen RDF from lanthanide aqua ion simulations denoted the average distance between the lanthanide ion and the oxygen atoms of the water molecules, which was compared to experimental results produced from experimental X-ray diffraction measurements and experimental EXAFS spectra. The RMSD plots displayed a dynamic coordination structure, while EXAFS generated from the simulation and compared to experimental results displayed a significant degree of similarity in the scattering of photoelectrons.

The extended material structure of lanthanum-exchanged faujasite was simulated in gas-phase or liquid-phase water molecules. A model structure of faujasite was constructed for the DFT calculations and AIMD simulations, with the same level of theory as described above for the lanthanide aqua ions. The periodic cell dimensions were optimized when the Si/Al ratio of faujasite was modified. AIMD simulations were used to sample conformational space to determine the position of exchanged cations and the conformation of the water molecules. The amount of water molecules in the liquid phase was determined through a series of NVT simulations to calculate the box pressure, and selecting the number of water molecules that produced the lowest non-negative pressure.

2.3 Extended X-ray absorption fine structure

The EXAFS spectra of select lanthanide aqua ions was measured by collaborators and compared to spectra predicted from AIMD simulations. EXAFS spectroscopy relies on

the excitation of a photoelectron from the core of an atom (a lanthanide in this study), the photoelectron is then scattered by the surrounding atoms (the oxygen atoms of the water molecules are largest contributors). Thus, the EXAFS spectra is a measurement of the scattering of the photoelectron due to local environment as described by the EXAFS equation,[14] see **equation 2.1**.

$$\chi(k) = \sum_j \frac{N_j f_j(k) \mathrm{e}^{-2k^2\sigma^2} \mathrm{e}^{-2R_j/\lambda}}{kR_j^2} \sin\left[2kR_j + \delta_j(k)\right] \quad (2.1)$$

The variables that are a function of *k* are the scattering properties of the atoms neighboring the excited atom and are used to predict *R*, *N,* and σ^2, which are structural parameters for the distance to neighboring atom, number of neighboring atoms, and disorder in the distance from the neighbor respectively.

The EXAFS spectra were predicted from AIMD simulations from a sample of two hundred equally spaced frames using FEFF.[15] FEFF solves **equation 2.1** for a given set of atomic coordinates obtained from simulation. The $\chi(k)$ spectra were directly compared to the experimental EXAFS spectra. The AIMD spectra were generated from the lanthanide and oxygen coordinates, effectively modeling a photoelectron single-scattering process, where a photon would be excited out of the trivalent lanthanide and be scattered by surrounding oxygens atoms. Similarities in the AIMD-predicted and experimentally-measured spectra suggests a similar local environment.

2.4 Bluemoon ensemble rare event sampling

Bluemoon ensemble is a rare event simulation technique that enables the quantification of reactions in terms of free energy.[16,17] Similar to umbrella sampling which uses restraints, Bluemoon utilizes the average force on a constraint to obtain a potential of mean force. The use of constraints instead of restraints makes it accessible for AIMD simulations. The purpose of this technique was to cross energy barriers that would not occur during a molecular dynamics simulation. The deprotonation reaction of the lanthanide aqua ion, and the deprotonation of hydrogen-exchanged faujasite, were modeled using this method. The constraint used was the distance of an oxygen - hydrogen bond, this was the selected reaction coordinate. A series of constrained AIMD simulations were conducted, each had the constraint increased as the bound hydrogen was pulled from its initial position to a neighboring water molecule. Integration of the forces on the constraint was used to obtain a free energy profile for the reactions, then the Helmholtz free energies were obtained from the potential of mean force. Error in the free energy profile was estimated by calculating the difference between the potentials of mean force using the first half and the second half of the trajectory.

The hydrolysis reactions of the lanthanide aqua ions provided a well-known benchmark to determine a computational protocol for replicating lanthanide reaction energies.[18] The acidity constants of the lanthanide aqua ions are widely reported in literature, as the pK_a will determine the pH at which a lanthanide aqua ion will deprotonate and form bridges between hydroxyl groups and precipitate out of solution. The first acidity constant was determined from the potential of mean force. The O-H distance between a hydrogen atom on a Ln-coordinated water molecule and a neighboring water molecule was the reaction coordinate.

The Brønsted acidity of hydrogen-exchanged faujasite was determined through Bluemoon rare event sampling. The O-H distance between a protonated aluminum tetrahedra and a nearby water molecule, was constrained and served as a reaction coordinate. Simulations were conducted for each increment the proton was moved. The average force on the constraint was integrated over the reaction coordinate to obtain a potential of mean force, which was used to determine the free energy of proton transfer and the effect lanthanum had on the Brønsted acidity of faujasite.

Bluemoon rare event sampling was suitable to obtain a potential of mean force of the proton transfer reactions based solely on constraints.[19] More complex reaction coordinates may require other enhanced sampling techniques, such as metadynamics.[20]

2.5 Electronic structure calculations

The second and third hydrolysis constant of the lanthanide aqua ions were not determined using Bluemoon rare event sampling; instead, a higher level of theory was utilized to quantify reaction energies. The second and third hydrolysis constants were calculated relative to the first hydrolysis constant. All electron single point energy calculations for all species of the lanthanide aqua ion hydrolysis reactions were conducted. A single point energy calculation determined the energy of a structure a single conformation of nuclear coordinates, with the benefit of considering all electrons present, thus enabling the quantification of thermodynamic properties with greater accuracy. All electron calculations were challenging for lanthanides due to many nearly degenerate electronic states that are considered. The structures used for the single point energy were not

guaranteed to be at global minima, but represent the minima for a large conformational space as the structures were produced by AIMD simulation. These minima represented the most stable states the aqua ions reached over given time, but a global, or most stable state, is not guaranteed. The all electron calculations were done with ORCA[21] with the M06 functional.[22]

For all electron calculations with lanthanide elements, relativistic effects must be considered. The internal magnetic moment resulting from an electron having spin angular momentum was accounted to better quantify the behavior of moving electrons while accounting for relativity. The relativistic effects have a significant contribution for heavy atoms due to the number of electrons present; as a result, the relativistic contributions become non-negligible in all electron level calculations. The lanthanides are within this range of heavy atoms, and thus a relativistic Hamiltonian was used for its correction to the kinetic energy. In short, with lighter atoms with less electrons the relativistic effects were negligible in all electron level calculation, but the contribution increases with the number of electrons present.

Chapter 2 References

(1) Housecroft, C. E.; Sharpe, A. G. *Inorganic Chemistry*, Second.; Pearson Education Limited, 2005.

(2) Smith, R. M.; Martell, A. E. *Critical Stability Constants: Inorganic Complexes*; Springer, 1976; Vol. 4.

(3) Micskei, K.; Helm, L.; Brucher, E.; Merbach, A. E. Oxygen-17 NMR Study of Water Exchange on Gadolinium Polyaminopolyacetates [Gd(DTPA)(H2O)]2- and [Gd(DOTA)(H2O)]- Related to NMR Imaging. *Inorg. Chem.* **1993**, *32* (18), 3844–3850. https://doi.org/10.1021/ic00070a013.

(4) Lauffer, R. B. Paramagnetic Metal Complexes as Water Proton Relaxation Agents for NMR Imaging: Theory and Design. *Chem. Rev.* **1987**, *87* (5), 901–927.

(5) Fitriyanto, N. A.; Fushimi, M.; Matsunaga, M.; Pertiwiningrum, A.; Iwama, T.; Kawai, K. Molecular Structure and Gene Analysis of Ce3+-Induced Methanol Dehydrogenase of Bradyrhizobium Sp. MAFF211645. *J. Biosci. Bioeng.* **2011**, *111* (6), 613–617. https://doi.org/10.1016/j.jbiosc.2011.01.015.

(6) Hibi, Y.; Asai, K.; Arafuka, H.; Hamajima, M.; Iwama, T.; Kawai, K. Molecular Structure of La3+-Induced Methanol Dehydrogenase-like Protein in Methylobacterium Radiotolerans. *J. Biosci. Bioeng.* **2011**, *111* (5), 547–549. https://doi.org/10.1016/j.jbiosc.2010.12.017.

(7) Cook, E. C.; Featherston, E. R.; Showalter, S. A.; Cotruvo, J. A. Structural Basis for Rare Earth Element Recognition by Methylobacterium Extorquens Lanmodulin. *Biochemistry* **2019**, *58* (2), 120–125. https://doi.org/10.1021/acs.biochem.8b01019.

(8) Nakagawa, T.; Mitsui, R.; Tani, A.; Sasa, K.; Tashiro, S.; Iwama, T.; Hayakawa, T.; Kawai, K. A Catalytic Role of XoxF1 as La3+-Dependent Methanol Dehydrogenase in Methylobacterium Extorquens Strain AM1. *PLoS One* **2012**, *7* (11), 1–7. https://doi.org/10.1371/journal.pone.0050480.

(9) Goedecker. Separable Dual-Space Gaussian Pseudopotentials. *Phys. Rev. B - Condens. Matter Mater. Phys* **1996**, No. 54, 1703–1710.

(10) Lu, J. B.; Cantu, D. C.; Nguyen, M. T.; Li, J.; Glezakou, V. A.; Rousseau, R. Norm-Conserving Pseudopotentials and Basis Sets to Explore Lanthanide Chemistry in Complex Environments. *J. Chem. Theory Comput.* **2019**, *15*, 5987–5997. https://doi.org/10.1021/acs.jctc.9b00553.

(11) Grimmel, S.; Schoendorff, G.; Wilson, A. K. Gauging the Performance of Density Functionals for Lanthanide-Containing Molecules. *J. Chem. Theory Comput.* **2016**, *12* (3), 1259–1266. https://doi.org/10.1021/acs.jctc.5b01193.

(12) Cundari, T. R.; Stevens, W. J. Effective Core Potential Methods for the Lanthanides. *J. Chem. Phys.* **1993**, *98*, 5555–5565.

(13) Shiery, R. C.; Fulton, J. L.; Balasubramanian, M.; Nguyen, M.-T.; Lu, J.-B.; Li, J.; Rousseau, R.; Glezakou, V.-A.; Cantu, D. C. Coordination Sphere of Lanthanide Aqua Ions Resolved with Ab Initio Molecular Dynamics and X-Ray Absorption Spectroscopy. *Inorg. Chem.* **2021**, *60* (5), 3117–3130. https://doi.org/10.1021/acs.inorgchem.0c03438.

(14) Newville, M. *Fundamentals of XAFS*; 2014. https://doi.org/10.1515/9781614517863.33.

(15) Rehr, J. J.; Kas, J. J.; Prange, M. P.; Sorini, A. P.; Takimoto, Y.; Vila, F. Ab Initio Theory and Calculations of X-Ray Spectra. *C. R. Phys* **2009**, *10* (6), 548–559.

(16) Carter, E. A.; Ciccotti, G.; Hynes, J. T.; Kapral, R. Constrained Reaction Coordinate Dynamics for the Simulation of Rare Events. *Chem. Phys. Lett.* **1989**, *156* (5), 472–477. https://doi.org/https://doi.org/10.1016/S0009-2614(89)87314-2.

(17) Sprik, M.; Ciccotti, G. Free Energy from Constrained Molecular Dynamics. *J. Chem. Phys.* **1998**, *109* (18), 7737–7744. https://doi.org/10.1063/1.477419.

(18) Shiery, R. C.; Cooper, K. A.; Cantu, D. C. Computational Prediction of All Lanthanide Aqua Ion Acidity Constants. *Inorg. Chem. Under Rev.*

(19) Ciccotti, G.; Kapral, R.; Vanden-Eijnden, E. Blue Moon Sampling, Vectorial Reaction Coordinates, and Unbiased Constrained Dynamics. *ChemPhysChem* **2005**, *6* (9), 1809–1814. https://doi.org/10.1002/cphc.200400669.

(20) Barducci, A.; Bonomi, M.; Parrinello, M. Metadynamics. *Wiley Interdiscip. Rev. Comput. Mol. Sci.* **2011**, *1* (5), 826–843. https://doi.org/10.1002/wcms.31.

(21) Neese, F. Software Update: The ORCA Program System, Version 4.0. *Wiley Interdiscip. Rev. Comput. Mol. Sci.* **2018**, *8* (1), 4–9. https://doi.org/10.1002/wcms.1327.

(22) Zhao, Y.; Truhlar, D. G. The M06 Suite of Density Functionals for Main Group Thermochemistry, Thermochemical Kinetics, Noncovalent Interactions, Excited States, and Transition Elements: Two New Functionals and Systematic Testing of Four M06-Class Functionals and 12 Other Function. *Theor. Chem. Acc.* **2008**, *120* (1–3), 215–241. https://doi.org/10.1007/s00214-007-0310-x.

CHAPTER 3

The coordination sphere of lanthanide aqua ions resolved with ab initio molecular dynamics and X-ray absorption spectroscopy

Richard C. Shiery[1], John L. Fulton[2], David C. Cantu[1]

[1]*Department of Chemical and Materials Engineering, University of Nevada, Reno*

[2]*Physical Sciences Division, Pacific Northwest National Laboratory*

An excerpt of a paper published paper in *Inorganic Chemistry*, 60, 3117 – 3130.

Title of full paper: The coordination sphere of lanthanide aqua ions resolved with ab initio molecular dynamics and X-ray absorption spectroscopy

Authors of full paper: Richard C. Shiery[a], John L. Fulton[b*], Mahalingam Balasubramanian[c], Manh-Thuong Nguyen[b], Jun-Bo Lu[d], Jun Li[d], Roger Rousseau[b], Vassiliki-Alexandra Glezakou[b], David C. Cantu[a]

[a] *Chemical and Materials Engineering, University of Nevada, Reno*

[b] *Physical Sciences Division, Pacific Northwest National Laboratory*

[c] *Advanced Photon Source, Argonne National Laboratory*

[d] *Department of Chemistry, Tsinghua University*

3.1. Introduction

Resolving lanthanide (Ln) solution structures, at atomic resolution, is relevant for rare earth separation and purification,[1,2,11,3–10] medical contrast agents,[12–14] single molecule magnets,[15–19] luminescent materials,[20–25] to mention only a few applications. The most common oxidation state of Ln is +III and are characterized by large coordination spheres that can accommodate seven to nine coordination sites. They are often more reactive than transition metal ions,[26] and they form labile, largely ionic coordination bonds with ligands or solvent molecules. As a result, Ln^{3+} ions, with highly reactive and dynamical coordination structures, have a large conformational space, which poses challenges in determining the coordination structures of lanthanide ions, both computationally and experimentally. In this work, we focus on the solution structures of the Ln^{3+} aqua ions for all lanthanides, from lanthanum to lutetium, which has been a matter of considerable discussion for decades.[27,28,37–46,29,47–54,30–36]

X-ray diffraction (XRD)[28–30] and extended x-ray fine absorption structure[37,42,47,53] (EXAFS) measurements have been used to determine average Ln-O distances and coordination numbers (CNs) of lanthanide elements, except for Pm due to its radioactivity. X-ray diffraction methods were used to determine that the early Ln^{3+} ions (La – Nd) favor a coordination of nine (nona-aqua ions), the later Ln^{3+} ions (Tb – Lu) are eight-coordinate (octa-aqua ions), and the middle lanthanides are in transition from nine to eight, likely in equilibrium between eight and nine CNs.[28–30] It is widely accepted that that the contraction of Ln^{3+} radii with increasing atomic number results in a slight decrease in the CN of the first hydration sphere. EXAFS measurements have shown a gradual change in CN across the lanthanide series.[42]

A classification of the molecular geometry of the first coordination sphere remains elusive to this day, due to the labile nature of coordination bonds between water molecules and Ln^{3+} ions. Recent EXAFS measurements suggest a tricapped trigonal prism for the lighter lanthanides while stability shifts in favor of the square antiprism across the series.[42,47] Conventional spectroscopic methods such as X-ray diffraction, nuclear magnetic resonance, infrared spectroscopy, or ultraviolet-visible spectroscopy have little or no sensitivity for local symmetry about solutes in disordered systems. In contrast, EXAFS multiple scattering analysis ―due to its exquisite sensitivity to many-body correlations―has the potential to elucidate the local symmetry and structure, thereby shining light on these long-standing unresolved structures of the lanthanide series. Additionally, the geometric complexities of Ln^{3+} – first-shell water structure provide an ideal test case for comprehensive multiple scattering analysis. The ability to discriminate different types of hydration symmetry using multiple scattering can be ascribed to several key factors: i) there is a very strong angular dependence of the photoelectron multiple scattering processes;[55] ii)in particular, the collinear multiple scattering paths provide greatly enhanced EXAFS signals due to strong re-focusing (or lensing) for photoelectron return paths that transit the absorber;[56,57] iii) the single scattering contributions from second- and higher-shells can be readily differentiated from overlapping multiple scattering contributions since the EXAFS phase and amplitude functions are quite different,[58] and iv) the use of L_3- and L_1-edges (dominated by $p \rightarrow d$ versus $s \rightarrow p$ dipole-allowed transitions) provides key independent information that disentangles overlapping EXAFS contributions due to the different geometrical

dependence of the L_3- and L_1-edge multiple scattering, dictated by transition matrix element.[59,60]

The ability of *ab initio* molecular dynamics (AIMD) to predict EXAFS multiple scattering spectra up to about R = 5.0 Å directly from the atom coordinates has been previously demonstrated for the 3*d* transition elements.[58] This can be achieved by sampling configurations from AIMD trajectories and generating ensemble-averaged EXAFS spectra with codes, like FEFF.[61–63] It is possible to extend these distances up to about 8.5 Å wherein a single ejected photoelectron is subsequently scattered by up to six or more atoms before the photoelectron returns to the central absorbing Ln^{3+} ion. These long-distance processes are efficient for Ln^{3+} due to the relatively low disorder of water molecules in the first shell (vide infra) and are key to fingerprinting the coordination symmetry.

Classical molecular dynamics (MD) simulations, with fitted Ln^{3+} non-bonding parameters, have been widely used to simulate the Ln aqua ions.[27,32,48–52,64,65,33,36,38,40,43–46] Careful parametrization of the Ln^{3+} non-bonded force field parameters, based on either electronic structure calculations or experimental data, have resulted in classical MD simulations that can replicate Ln-O distances. Consistent with EXAFS measurements, a study reports that the lighter lanthanides favor a tricapped trigonal prism geometry with a coordination number of nine, while the heavier lanthanides with a coordination of eight oscillate between square antiprism and bicapped trigonal prism[45]. Another study shows that the middle lanthanides had non integer coordination numbers and that fluctuations between geometries are common between Tb and Dy.[43] A more recent study reported stable first-sphere geometries where, in particular, Lu^{3+} had a square antiprism

geometry.[52] Classical MD simulations have an advantage in that they can access larger time and length scales, thereby allowing the simulation to elucidate water exchange mechanisms[36,40,48] and ion association events.[65] However, classical MD force fields are based on fitted parameters that may not accurately predict the Ln coordination structure for chemical systems that are different from those of the parametrization conditions, and when concurrent reactive events are not considered because the electronic structure is not explicitly included.

Recent studies of nona-aqua Ln^{3+} ions that were based on electronic structure calculations, postulate that the bond strength decreases with bond length across the series for the capped geometries,[66,67] which offers a potential explanation of why the middle lanthanides display varying CNs of eight or nine. Although electronic structure studies of Ln^{3+} aqua ions do not capture dynamic effects, relevant properties regarding typical Ln-O distances can be revealed and the lanthanide contraction can be quantified.[54] Therefore, a computational approach that combines the advantages of MD (molecular sampling) and electronic structure (reactivity, no fitted parameters) is needed to determine the molecular structure in Ln^{3+} aqua ions in solution without prior assumptions.

We recently optimized the complete set of highly transferable Goedecker, Teter, and Hutter (GTH)-type[68] pseudopotentials for all the lanthanide elements, and their corresponding basis sets, specifically optimized for generalized gradient approximation (GGA) calculations in a mixed Gaussian−plane wave scheme.[69] Our complete set of lanthanide pseudopotentials and accompanying basis sets[70] enable us to perform density functional theory (DFT) calculations and *ab initio* molecular dynamics (AIMD) simulations of lanthanide ions in explicit water boxes with periodic conditions. This

combines the advantages of electronic structure (reactivity, lanthanide coordination bond formation) and molecular dynamics simulations (sampling structures with explicit solvent molecules) to resolve the solution structure of lanthanide ions in solution. Other types of lanthanide pseudopotentials (i.e. effective core potentials) and basis sets were known,[71–77] but can be employed in only electronic structure calculations with lanthanide systems containing $\sim 10^2$ atoms,[78,79] and without molecular dynamics sampling. Thus, simulating the solution structure of Ln^{3+} ions, considering the electronic structure, combined with molecular dynamics sampling that explicitly includes solvent molecules, was not possible until recently.

We have two goals in this study: i) demonstrate that our pseudopotentials and basis sets (LnPP1) with AIMD simulations can replicate and predict the structures of lanthanide ions in solution, and ii) resolve the structural dynamics of lanthanide aqua ions with AIMD simulations and EXAFS studies that includes analysis of the multiple scattering contributions in a detailed and judicious manner. Previously, we showed[70] that our LnPP1 pseudopotentials and basis sets can replicate lanthanide oxidation reactions, heats of formation, and ionization potentials (i.e. reactivity). In this work, we show that our pseudopotentials and basis sets with AIMD simulations also replicate the solution structure of Ln^{3+} aqua ions within 0.05 Å comparing to experimental measurements. We reveal that Ln^{3+} aqua ions have a highly dynamic first coordination sphere with no fixed molecular geometry. Further, we directly compare $\chi(k)$spectra from EXAFS measurements with $\chi(k)$ spectra from AIMD simulations to verify our simulation results. By means of a coupled approach (measured EXAFS and simulated AIMD-EXAFS), we take full advantage of the sensitivity to many-body structural correlations via multiple

scattering processes, and we employ a comprehensive EXAFS multiple scattering analysis for the first time to evaluate the local molecular geometry and inherent dynamics of the first sphere of Ln^{3+} aqua ions. The much smaller core-hole lifetime broadening at the L-edges of even the late lanthanides in contrast to the corresponding K-edge is indispensable to help directly capture the high-frequency signals that encode the local geometry in the XAFS signal.[47,80] This work extends multiple scattering analysis to much higher distances, R ~ 6.5 Å, and demonstrates enhanced sensitivity for the fine details of hydration structure from a multitude of different photoelectron scattering processes that emanate from scattering within the first solvent shell. Our approach, which considers coordination bond formation concurrently with solvent molecule dynamics, is uniquely suited to resolve elusive solution structures.

3.2. Methods

3.2.1 Ab initio molecular dynamics simulations and analysis

We independently simulated each Ln aqua ion with 64 explicit water molecules, including hydrogen atoms, in a cubic periodic box having a length of 12.42 Å. All Ln ions were simulated in the +III oxidation state and for this reason 3 Cl^- ions were added to the simulation box to provide the neutral system with closed-shell chlorine anions and with lanthanide cations including all the spin density. The Ln^{3+} multiplicities, assigned with Hund's rule, are presented in the Supporting Information (SI). All the atoms in the AIMD simulation boxes were modelled with DFT.

All DFT calculations and AIMD simulations were conducted in the PBE functional,[81] which has been well-tested for both water[82,83] and lanthanides,[84,85] using the CP2K package.[86,87] Core electrons were modeled with norm-conserving GTH pseudopotentials,[68] valence electrons were modelled with polarizable double-zeta basis sets,[88] and our LnPP1 pseudopotentials and basis sets[70] were used for the Ln^{3+} ions. Long range electrostatic terms were determined with a supplementary plane wave basis set, using a 500 Ry cutoff for La – Gd, 800 Ry for Tb – Tm, and 1000 Ry for Yb – Lu. Larger density cutoff values were used for later lanthanides because we adopted medium-core pseudopotentials for Tb to Lu.[70] Grimme's D3 corrections[89] were used to account for van der Waals interactions within a 6.0 Å radius in all simulations.

All AIMD simulations were done in the NVT ensemble at room temperature, in 12.42 Å cubic boxes. Our initial simulation was with the Eu^{3+} ion where the Eu and Cl atoms were randomly placed in a 64-water box (density of water at room temperature) with sufficient spacing between them to avoid ion pair formation in the AIMD time scale. Cl^- anions were chosen as counter ions due to AIMD simulation box size limitations. We observed the formation of an 8-coordinate water environment around the Eu^{3+} after > 20 ps of AIMD. Due to computational resources, all further simulations started from the formed the octa-aqua Ln^{3+} ion coordinates. We replaced the Eu^{3+} ion with each La – Lu independently, and then undertook the following protocol for each Ln^{3+} ion: i) an initial geometry optimization, ii) 1ps of NVT simulation at 500K with 1 fs time steps to ensure proper mixing and to test the stability of the Ln^{3+} aqua ion, iii) slow annealing to 0K over 2 ps, iv) a final geometry optimization. The final geometry optimized step was the starting point for production NVT simulations at room temperature. Initially, a 0.5 fs time

step was chosen, but we subsequently observed that a 1 fs time step is sufficient. We ran the production NVT AIMD simulations for > 15 ps, until we observed at least 10 ps of simulation with a stable potential.

Eu – Lu were simulated as octa-aqua ions: starting from the initial Eu simulation, we replaced Eu^{3+} with each Ln^{3+} ion, and following the protocol described above. An additional water molecule was added to La – Sm to simulate nona-aqua ions with the protocol described. The ninth water left the Sm^{3+} first coordination shell, so Eu^{3+} and all subsequent Ln^{3+} ions were simulated as 8-coordinate. Sm^{3+} was simulated as both 8- and 9-coordinate independently for > 10ps, but the Ln-O distances of the nona-aqua had better agreement with experiment. Therefore, La – Sm were simulated as 9-coordinate, starting from the initial Eu octa-aqua ion geometry with the addition of the ninth water molecule to the Ln^{3+} first coordination sphere, then following the protocol described.

At least 10 ps of stable production AIMD simulations were used to analyze Ln^{3+} aqua ion dynamics. Simulation analysis began with calculating the Ln-O radial distribution functions (RDFs) to quantify frame-averaged Ln-O pair distances (SI). Ln-O distances can be directly compared with experimental measurements in the literature. The maximum of centroid of the first peak of each RDF was used as the average distance between each Ln^{3+} ion and its first sphere oxygen atoms of the surrounding water molecules. O-Ln-O angles were extracted from the equilibrated AIMD simulations to construct angle distribution functions (ADFs). No ion pairs were observed since Cl^- ions do not come within 4 Å of Ln^{3+} ions (SI). The distant starting position diffusionally isolates it from the cation over the course of the AIMD trajectory.

The average Ln-O distances were used to generate reference molecular geometries for each Ln^{3+} ion: square, square antiprism, trigonal dodecahedron (DDH), and bicapped trigonal prism (BTP), for the lanthanides with a coordination number of eight;[90,91] and capped square antiprism, capped square, and tricapped trigonal prism (TTP) for lanthanides with a coordination number of nine. The O coordinates of these reference molecular geometries were used to calculate the root mean square deviation (RMSDs). A single RMSD value is derived from the distances between the eight (or nine) oxygen atoms of the reference molecular geometry and the corresponding eight (or nine) oxygen atoms that form the first coordination sphere in an AIMD simulation frame. We calculated the RMSD between each AIMD frame and all reference molecular geometries and then averaged these over the entire AIMD trajectory to quantify which reference molecular geometry each Ln^{3+} ion is most similar to.

3.2.2 Experimental measurement of extended X-ray absorption fine structure spectra

Experimental measurements were done by Mahalingam Balasubramanian and John Fulton, see details in the published paper: Shiery et al., *Inorganic Chemistry*, **2021**, 60, 3117 - 3130.

3.2.3 Extended X-ray absorption fine structure spectra from ab initio molecular dynamics

The general method of MD-XAFS has been previously described.[92] Comparing predicted and measured EXAFS spectra is particularly well suited to resolve the coordination

structure of heavy elements.[93] We generated $\chi(k)$ spectra from AIMD trajectories,[94] using FEFF8.5,[62] to directly compare with experimentally generated EXAFS spectra. From the equilibrated AIMD trajectory of each Ln^{3+} ion, we extracted 200 equispaced frames, and retrieved the Ln and O coordinates, to generate ensemble average spectra. An AIMD-EXAFS spectrum[92,94,95] is generated for each AIMD snapshot, or frame. The EXAFS computation accumulated ~10^5 single- and multiple-scattering paths (up to 8.5 Å) from a single AIMD frame. Then, an ensemble-average spectrum was generated from 200 frames for each case (Ln^{3+}, $L_{\#}$ edge). The final spectrum is then comprised of approximately 10^7 scattering paths. Within FEFF8.5 the significance-threshold (CRITERIA) for any given paths was set to zero to be sure that small contributions from hundreds of paths that might contribute to a high-R feature are all included in the calculation. A further FEFF8.5 adjustment was to change the default value of 1200 total paths to include up to 35,000 paths in order to include all the atom backscattering out to about 8.5 Å. Only Ln and O atoms were included in the FEFF calculations because the inclusion of H atoms results in a too large number of scattering paths that fail to converge. Also, H atoms are expected to contribute approximately 5% to the total scattering signal in the R-plot regions between 2 to 2.5 Å, which is below the region for the multiple scattering signal that is the focus of this paper. The Hedin-Lundqvist exchange-correlation potential (default for FEFF8.5) was used with no SCF.

The EXAFS photoelectron single-scattering process provides a simple and accurate measure of the first-shell Ln-O distances. On the other hand, photoelectron multiple scattering processes for the various colinear and triangular paths provide information about the symmetry of water in the first hydration shell. The sequential series

of scattering by up to six or more atoms were included for a single ejected photoelectron. A detailed interpretation of the multiple scattering features for pure octahedral symmetry of the first-row transition metals has been previously reported.[58] While it is relatively easy to manually apply a multiple scattering analysis to systems having octahedral symmetry, where there is a limited degree of path degeneracy, such manual fitting of more complex symmetries (CN > 6) is intractable due to their complexity. Here, the AIMD-EXAFS method generates an accurate and comprehensive representation of the entire sets of photoelectron scattering processes. If the simulated structure faithfully reproduces the symmetry of the experimental structure, then all aspects of the single- and multiple-scattering contributions will be quantitatively reproduced. The phase and amplitude functions at the two edges, L_3 and L_1, depend not only on the symmetry/structural geometry that determines the multiple scattering contributions, but also on the nature of the final state electronic wave function governed by the dipole-allowed selection rule. Hence, the multiple scattering portions of L_3- and L_1-edge spectra give independent and enhanced information on the local symmetry, instead of being mere, redundant measurements.[59]

A single adjustable parameter, the edge energy or E_0, of the experimental spectra is adjusted to match the spectra created via FEFF8.5 calculations. The main criterion is that the primary oscillations in $\chi(k)$ plots of the experiment and simulated spectra converge as k approaches zero. As a further test, the E_0 setting was applied to the multiple scattering paths. For instance, the set of multiple scattering peak that lies between approximately 3.5 to 4.5 Å was windowed in R-space and then back-transformed to $\chi(q)$ where the same convergence of oscillations at low q was confirmed.

Overall, we find that the E_0 parameter is only weakly correlated with Ln-O distances and Debye-Waller factor.

It is possible to use the AIMD trajectory to decompose the total EXAFS spectra into the relative contributions from: i) single scattering or multiple scattering paths, ii) individual first, second, or higher shell contributions, and iii) from the individual contributions from sets of molecular geometries that are present in equilibrium. This can be achieved by varying FEFF input parameters, by isolating sets of atoms in certain shells, or by sorting MD trajectory frames using appropriate order parameters, respectively. For the multiple scattering, the contributions up to 8.5 Å are appropriate since they are derived from only the first-shell structure that is well represented by AIMD. We compared the single scattering paths (NLEG=2, RPATH = 8.5) to multiple scattering (NLEG=8, RPATH 8.5) paths for one case in order to show the relative contribution of multiple scattering paths to the total spectral signal. The single scattering contributions beyond 4.5 Å are quite weak due to high disorder while the multiple scattering contributions are relatively high due to the very low disorder in the first shell.

3.3. Results & Discussion

3.3.1. First coordination sphere structure predicted with AIMD matches experiment

We independently simulated with AIMD all Ln^{3+} ions (**Figure 3-1**), and calculated their Ln-O radial distribution functions (RDFs), see details in the Methods Section 2.1, to obtain Ln-O distances in solution at room temperature. The first peak of the Ln-O RDFs

for each Ln^{3+} ion are reported in **Table 3-1**, and graphically represented in **Figure 3-2**, alongside the experimental Ln-O distance values reported in the literature.[28–30,37,42,47,53]

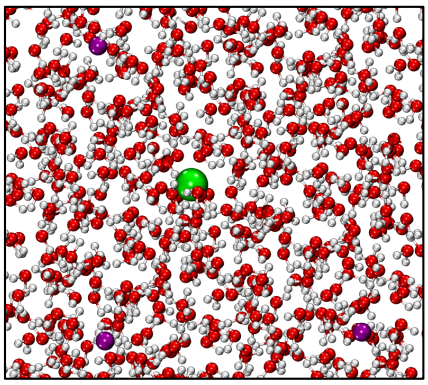

Figure 3-1. Example of an all-AIMD, periodic simulation box, includes a Ln^{3+} ion (green), 3 Cl^- anions (purple), and 64 water molecules with oxygen (red) and hydrogen (white) atoms.

Table 3-1. The Ln-O (Å) RDFs from the AIMD simulations, alongside measured Ln-O distances (Å), and the mean average deviation for each element. This data is graphed in **Figure 3-2**. *References A*: Habenschuss and Spedding, *J. Chem. Phys*. 1979, 70, 3758–3763; Habenschuss and Spedding, *J. Chem. Phys*. 1979, 70, 2797–2806; Habenschuss and Spedding, *J. Chem. Phys*. 1980, 73, 442–450. *Reference B*: Persson et al., *Chem. Eur. J*. 2008, 14, 3056–3066. *Reference C*: D'Angelo et al., *Inorg. Chem*. 2011, 50, 4572–4579. *Reference D*: Yamaguchi et al., *J. Chem. Phys*. 1988, 89, 5153–5159. *Reference E*: Allen et al., *Inorg. Chem*. 2000, 39, 595–601.

	Our AIMD Results	XRD References A	EXAFS Reference B	EXAFS Reference C	EXAFS Reference D	EXAFS Reference E	Mean Average Deviation
La	2.57	2.580	2.542	2.600	-	2.54	0.02
Ce	2.56	-	2.538	2.570	-	2.52	0.02
Pr	2.53	2.539	2.503	2.550	-	-	0.02
Nd	2.53	2.513	2.488	2.525	2.51	2.49	0.02
Pm	2.47	-	-	-	-	-	-
Sm	2.45	2.474	2.455	2.490	2.45	-	0.02
Eu	2.44	2.450	2.424	2.470	2.43	2.43	0.02
Gd	2.43	-	2.415	2.455	2.41	-	0.02
Tb	2.42	2.409	2.390	2.440	2.39	-	0.02
Dy	2.42	2.396	2.373	2.425	2.37	-	0.03
Ho	2.39	-	2.359	2.405	-	-	0.02
Er	2.38	2.369	2.350	2.390	2.34	-	0.02
Tm	2.36	2.358	2.334	2.375	2.33	-	0.02
Yb	2.38	-	2.317	2.360	-	2.32	0.05
Lu	2.34	2.338	2.310	2.345	2.31	-	0.02

Our Ln-O distances from the RDFs of the AIMD simulations are consistent with the experimentally measured Ln-O distances using EXAFS,[37,42,47,53] as well as XRD.[28–30] All simulated Ln-O distances are within 0.05 Å of experimental measurements, with a maximum mean average deviation of 0.05 Å reported for Yb. Replicating Ln-O distances is a strong indicator that the AIMD protocol employed with our LnPP1 pseudopotentials and basis sets can accurately predict the structure of Ln^{3+} ions in solution, without fitting any parameters.

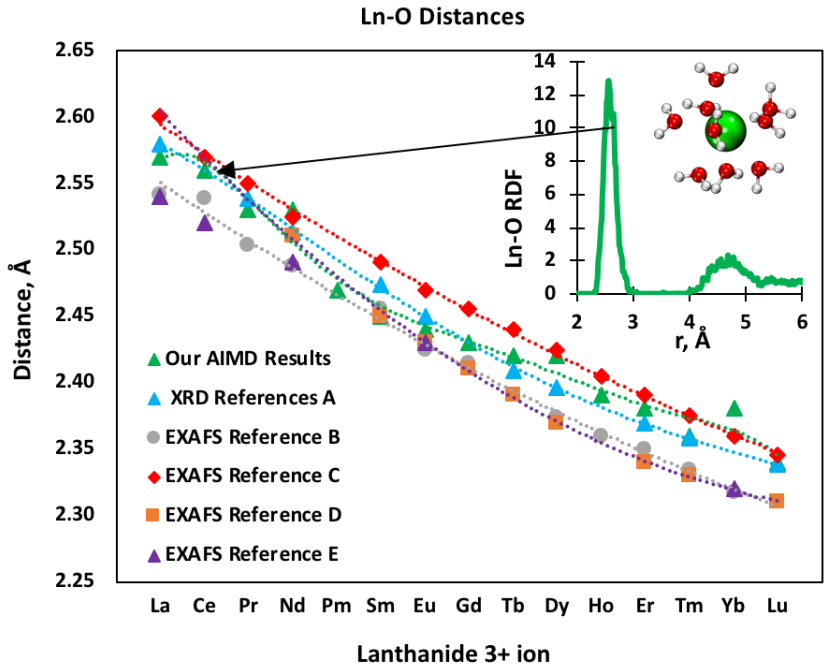

Figure 3-2. The Ln-O distances from AIMD RDF values (green triangles), for all Ln^{3+} ions, overlaid with data from literature (left). A sample RDF (Ce^{3+}-O, right) to show how average Ln-O distances were calculated. Top left shows the first coordination sphere (rest of water molecules excluded for clarity) of Ce^{3+} (green), water oxygen (red) and hydrogen (white) atoms. Ytterbium has the highest deviation when compared to experimental results, which is within 0.05 Å of the experimental results. *References A*: Habenschuss and Spedding, *J. Chem. Phys*. 1979, 70, 3758–3763; Habenschuss and Spedding, *J. Chem. Phys*. 1979, 70, 2797–2806; Habenschuss and Spedding, *J. Chem. Phys*. 1980, 73, 442–450. *Reference B*: Persson et al., *Chem. Eur. J*. 2008, 14, 3056–3066. *Reference C*: D'Angelo et al., *Inorg. Chem*. 2011, 50, 4572–4579. *Reference D*: Yamaguchi et al., *J. Chem. Phys*. 1988, 89, 5153–5159. *Reference E*: Allen et al., *Inorg. Chem*. 2000, 39, 595–601.

Experimental measurements of the EXAFS spectra at the L edges of Nd, Dy, Er, and Lu were performed, as described in the Methods Section 2.2. We also generated spectra from the AIMD trajectories, as described in Section 2.3, for direct comparison to the experiment. **Figure 3-3** provides this comparison between the experimentally measured EXAFS spectra with those that have been calculated directly using the atomic coordinates from the AIMD trajectories and scattering from FEFF8.5. **Figure 3-3** contains both the L_3- and L_1-edge spectra for Nd^{3+} and for Er^{3+}. For Nd^{3+}, the $k^3\chi(k)$ plots show very good agreement for overall frequency, the shape and amplitudes of the oscillations as would be expected from an accurate prediction of the Nd-O first shell distance by the AIMD simulation. This is further confirmed in the Fourier transform results in **Figure 3-3** for $Re[\chi(R)]$ showing an excellent match of the first-shell peak structure at about 1.8 Å. Further, the features at about 4Å arising from multiple scattering, and especially well-defined in the L_1-edge spectra, are faithfully reproduced by the AIMD simulations. For the experimental Nd EXAFS there are known artifacts from multi-electron excitation contributions[96] at about 6 $Å^{-1}$ in both the L_3- and L_1-edge spectra. While these have little effect on determining the first-shell distances, they do introduce a non-structural contribution into the longer range structure for R > 2.5 Å, especially for the L_3 spectra. For early- to mid-lanthanides, multi-electron excitations are a concern because they have spectral features that can include (i) step changes, (ii) slope changes, (iii) and strong white-line features that are very apparent in the lanthanide series.[97] For lanthanides, the magnitude of the multi-electron edges is very large with respect to the EXAFS contribution.[96] In addition, there are a series of multi-electron

edges that occur at increasingly high energies exciting lower valance electrons, whose spacing can be coincident with the EXAFS oscillations. Since the $\chi(k)$ range is finite, the manifestation of these artifact occurs in different ways in the Fourier transform, including termination effects that are present in the experimental data. In contrast, for the later lanthanides these multi-electron features are much weaker.[96]

Figure 3-3 also shows the corresponding set of EXAFS spectra for Er^{3+}. For Er^{3+}, Dy^{3+} and Lu^{3+}, the spectral features are not as quantitatively reproduced by AIMD as for Nd^{3+}, with the simulated Ln-O distance being approximately 0.07 Å longer than the experiment. If the theoretical EXAFS spectra are rescaled to correct for the 0.07Å distance overestimation (approximately 3%) excellent agreement with experimental spectra is seen. Empirical potentials that are used in classical MD can be quite accurate[47] since they are parametrized to fit XRD or EXAFS measurements. However, the agreement that we are reporting for the Ln^{3+} ions is one of the first using DFT/AIMD simulations and thus represents an excellent result for this level of theory (using generalized gradient approximation with exchange correlation functionals). Unlike fitted potentials used in classical MD, our AIMD simulations are completely independent of experimental measurements, and they are accurately reproducing the structure of the first coordination sphere of Ln^{3+} aqua ions. Going forward, the ability of DFT/AIMD methods to model systems with high chemical complexity sets it apart from mostly chemically-unresponsive empirical potential models, since it allows to concurrently simulate the reactivity and solution structure Ln-containing systems, for example in separation chemistry or solution-phase catalysis.

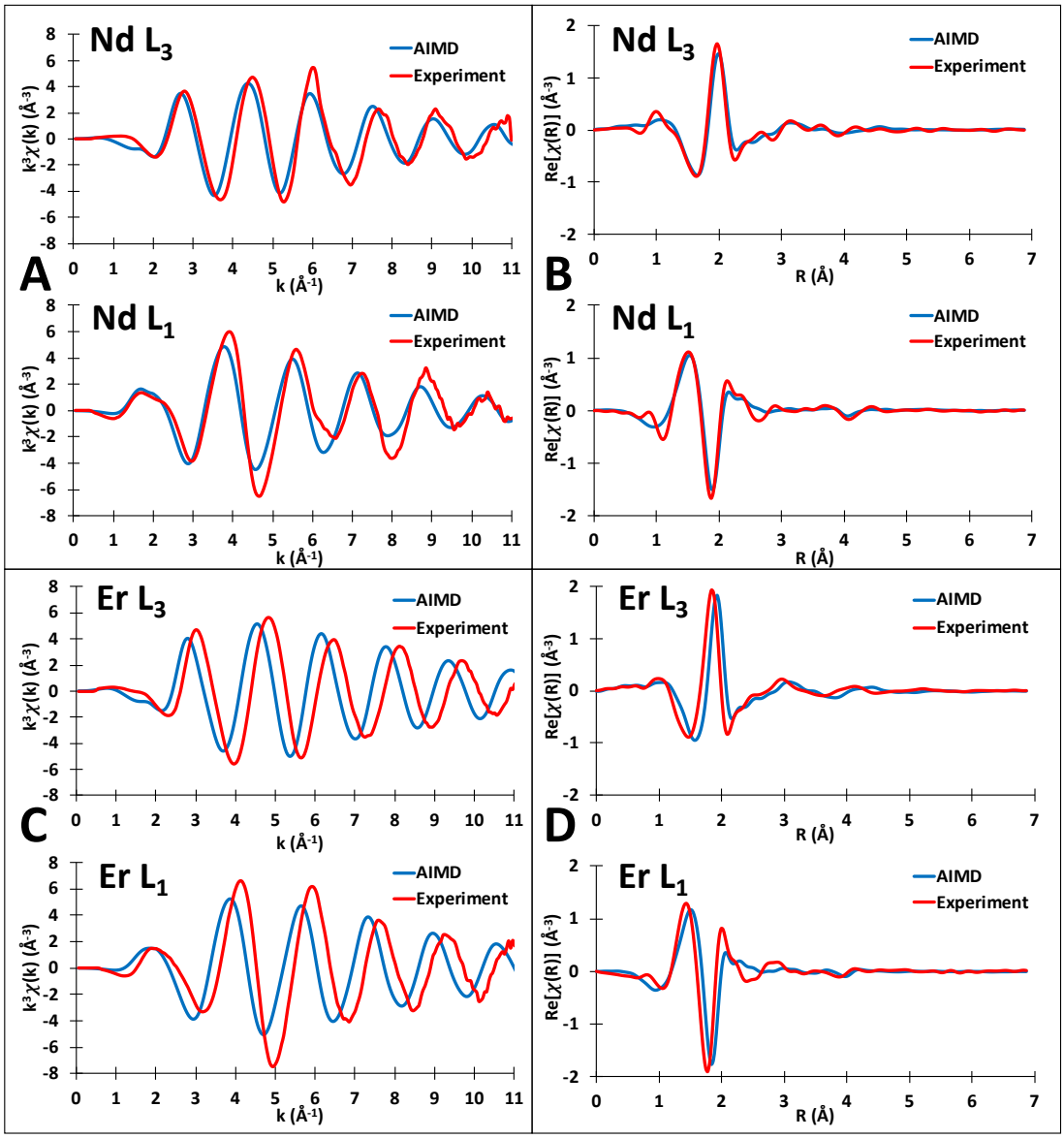

Figure 3-3. Comparison of calculated AIMD and experimental EXAFS spectra for the Nd^{3+} and Er^{3+} L_1- and L_3-edges. Figures A, C are derived from k^3-weighting of $\chi(k)$ (emphasizing first-shell structure) while Figures B, D representing $Re[\chi(R)]$, are derived from k^2-weighting (emphasizing multiple scattering structure for R > 2 Å). The Nd L_1 and L_3 data were windowed between $1.6 < k < 12.5$ Å^{-1} and $1.5 < k < 10$ Å^{-1}, respectively. The Er L_1 and L_3 data were windowed between $1.6 < k < 14$ Å^{-1} and $1.6 < k < 13$ Å^{-1}. The figures represent a simple overlay of independently generated $\chi(k)$ spectra from simulation with those from experiment. No fitting was done for this comparison, the AIMD-EXAFS and measured EXAFS spectra are completely independent of each other.

We observe that for the AIMD simulations, the nine-coordinate structure is preferred from La – Sm while the eight-coordinate structure from Eu – Lu is in agreement with experiment.[28–30,37,42,47,53] It should be noted that the AIMD simulations do not sample large enough time scales to observe water exchange events, although we did spontaneously observe that the AIMD trajectory for a nine-coordinate Sm^{3+} ion became eight-coordinate (see Methods). In qualitative agreement, a transition in the apparent molal volume with respect to ionic radius occurs at Sm.[98] We are not advocating that a clear divide occurs between Sm and Eu, due to the limitations of AIMD sampling. Unlike in experimental measurements or classical MD simulations, AIMD cannot average the equilibria between the eight- and nine-coordinate states, nor sample the 9-to-8 transition in coordination number.[99] Along these lines, we note that the notion of the clear "gadolinium break" has been challenged in recent experimental findings.[42] The shift in coordination number has been historically explained by the lanthanide contraction, but more recently electronic structure calculations at the CCSD(T) level of theory[67] point to decreasing bond strength when progressing through the lanthanide series.

3.3.2. Dynamic first coordination sphere geometry

For the first coordination sphere in the AIMD simulations of all Ln^{3+} ions, we calculated the root mean square distance (RMSD) between the first coordination sphere of each AIMD frame and the reference molecular geometries (**Figure 3-4**), see details in the Methods Section 2.1. The abbreviations that we use to identify the reference molecular geometries are also provided in **Figure 3-4**. The RMSD values were averaged over the entire AIMD trajectory to quantify the distance (Å) between corresponding oxygen atoms

in the Ln^{3+} aqua ions' first coordination sphere and their reference molecular geometries. The RMSDs were used to identify the more probable geometries for either the eight- or nine-coordinate Ln^{3+} ions. For example, a low RMSD value for the square antiprism geometry with respect to three other eight-coordinate reference molecular geometries, would mean that the dynamic solution structure of that simulated ion is most similar to a square antiprism geometry.

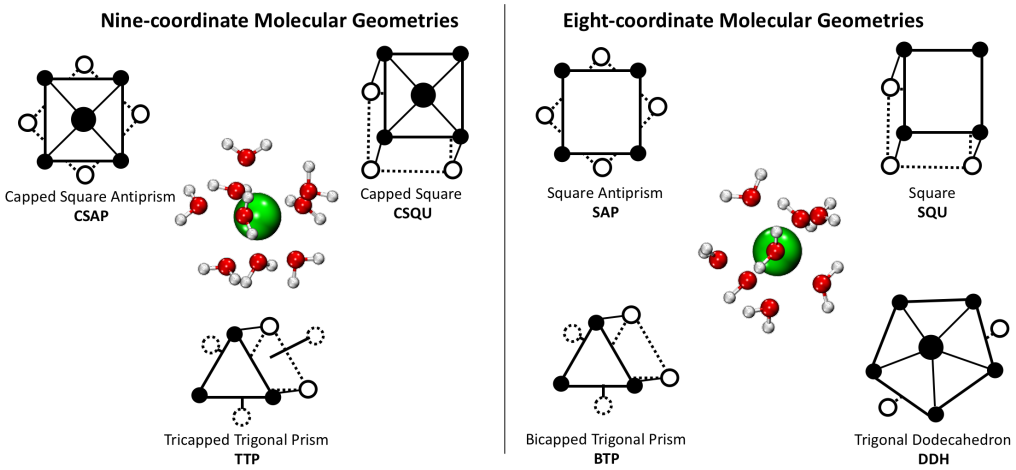

Figure 3-4. The first sphere molecular geometries for nine- and eight-coordinate Ln^{3+} ions. The color image is from an AIMD snapshot showing the first coordination spheres with Ln^{3+} (green) water oxygen (red) and hydrogen (white). Figures in black and white show the reference molecular geometries that are used to quantify the geometry of the first coordination sphere for each Ln^{3+} ion along the AIMD trajectory, where the circles represent oxygen atoms positions of that geometry.

The simulation-averaged RMSD values with respect to the reference molecular geometries, for all Ln^{3+} ions, are reported in **Tables 3-2** and **3-3**. The RMSD values suggest that all Ln^{3+} first coordination spheres are dynamic in solution at room temperature (AIMD conditions). Most RMSD values, for all reference geometries, are not near-zero (between ~0.40 Å and ~0.50 Å), meaning that the first coordination spheres of lanthanides do not have set molecular geometries, but are symmetrically disordered.

Table 3-2. Average RMSDs between the nine-coordinate Ln^{3+} ions and reference molecular geometries, as seen in **Figure 3-4**.

Element	Average RMSD ± Standard Deviation (Å)		
	Capped Square Antiprism	Capped Square	Tricapped Trigonal Prism
La	0.42 ± 0.02	0.47 ± 0.02	0.38 ± 0.03
Ce	0.45 ± 0.03	0.47 ± 0.02	0.38 ± 0.03
Pr	0.36 ± 0.03	0.43 ± 0.02	0.43 ± 0.03
Nd	0.42 ± 0.02	0.41 ± 0.02	0.48 ± 0.03
Pm	0.41 ± 0.02	0.45 ± 0.02	0.36 ± 0.03
Sm	0.51 ± 0.02	0.43 ± 0.02	0.39 ± 0.02

Previous classical MD studies[27,43–45,51] suggest that the early lanthanides favor the TTP geometry. Similarly, our AIMD simulations' RMSD values (**Table 3-2**) are generally lower for TTP than other geometries, especially Ce, Pr, Pm, and Sm being most TTP-like. However, our AIMD simulations point to dynamic nine-coordinate geometries (RMSD values ~0.4 Å), with the RMSD average values of TTP within the standard deviation of those of C-SAP for La and Pr. Further, the first coordination sphere of Nd^{3+} is the least TTP-like, with lower RMSD average values for the C-SAP and C-SQU geometries.

Table 3-3. Average RMSDs between the eight-coordinate Ln^{3+} ions and reference molecular geometries, as seen in **Figure 3-4**.

Element	Average RMSD ± Standard Deviation (Å)			
	Square	Dodecahedral	Square Antiprism	Bicapped Trigonal Prism
Eu	0.49 ± 0.02	0.40 ± 0.03	0.48 ± 0.02	0.43 ± 0.03
Gd	0.50 ± 0.02	0.42 ± 0.02	0.52 ± 0.02	0.49 ± 0.02
Tb	0.48 ± 0.02	0.43 ± 0.03	0.43 ± 0.04	0.45 ± 0.03
Dy	0.49 ± 0.02	0.42 ± 0.03	0.43 ± 0.03	0.48 ± 0.03
Ho	0.47 ± 0.02	0.46 ± 0.02	0.43 ± 0.03	0.40 ± 0.02
Er	0.48 ± 0.02	0.46 ± 0.02	0.43 ± 0.02	0.45 ± 0.02
Tm	0.44 ± 0.04	0.41 ± 0.03	0.37 ± 0.04	0.49 ± 0.03
Yb	0.50 ± 0.02	0.42 ± 0.02	0.42 ± 0.02	0.46 ± 0.02
Lu	0.47 ± 0.02	0.44 ± 0.02	0.39 ± 0.02	0.42 ± 0.03

The octa-aqua Ln^{3+} ions, like the nona-aqua ones, show RMSD values that are not close to zero, which means that they do not tightly fit with any of the reference molecular

geometries; however, the RMSD values show us to which molecular geometry they are most similar to at room temperature. The middle ions (Eu^{3+} – Dy^{3+}) are mostly DDH-like, with only Ho^{3+} having the lowest average RMSD to the BTP molecular geometry, within the standard deviation range to the SAP average RMSD. Gd^{3+} is the most DDH-like in the series. The average RMSD values of Eu^{3+} to DDH and BTP are close to each other, likewise for Tb^{3+} and Dy^{3+} and DDH and SAP average RMSD values are within their standard deviations. Similarly, a classical MD study[43] showed fluctuation between geometries for the middle lanthanides. We found that the later ions (Er^{3+} – Lu^{3+}) favor the SAP molecular geometry, however, very close to the BTP (Er^{3+}, Lu^{3+}) or the DDH geometries (Er^{3+}, Tm^{3+}, Yb^{3+}). In agreement with our findings, recent classical MD studies, report that the SAP geometry is favored for the later lanthanides.[27,49,50,52]

We calculated O-Ln-O values for all Ln^{3+} AIMD simulations and compared the angle distribution functions (ADFs) with those of the reference molecular geometries. **Figure 3-5** shows the comparison for Nd^{3+} (top) and Er^{3+} (bottom).

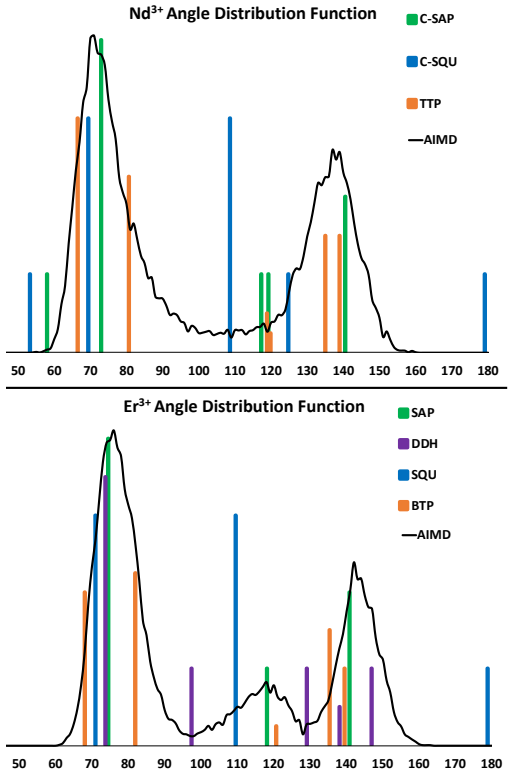

Figure 3-5: Ensemble of O-Ln-O distributions, top frame includes the Nd^{3+} angle distribution from the AIMD trajectory and those of the nine-coordinate reference geometries for comparison, while the bottom frame includes the Er^{3+} angle distribution from the AIMD trajectory and those of the eight-coordinate reference geometries for comparison.

From distribution of angles in **Figure 3-5**, one can clearly see that the capped square (9-coordinate) and square (8-coordinate) geometries are not favored by Nd or Er, in agreement with the RMSD values. Our Nd^{3+} O-Ln-O plot (**Figure 3-5, top**) shows that the ADF from AIMD matches the TTP geometries, unlike our RMSD values (**Table 3-2**), that, for the Nd^{3+} aqua ion, shows lower RMSD values to the C-SAP and C-SQU geometries. The lower RMSD values to the C-SAP and C-SQU geometries could be due to a single, longer capping Ln-O bond unlike the TTP geometry which has three longer Ln-O capping bonds. Similarly, a recent study,[50] which includes O-Ln-O analysis of classical MD simulations, supports that the C-SAP geometry is favored in the early

lanthanides. Previous classical MD studies[44,49,50,52] that analyzed O-Ln-O distributions show the best agreement to the SAP geometry for the later lanthanides, in agreement with our Er^{3+} O-Ln-O plot (**Figure 3-5, bottom**). However, the RMSD analysis shows that the later lanthanides' first coordination sphere, although most SAP-like, is also very close to the BTP or DDH geometries. The simulation-averaged RMSD values for most Ln^{3+} molecular geometries are within the standard deviation of the other molecular geometries, meaning that the Ln^{3+} ions' first sphere presents a dynamic behavior between different molecular geometries.

3.3.3. EXAFS multiple scattering analysis of Ln^{3+} aqua ion molecular geometries

Figure 3-6 compares the Er^{3+} L_3 and L_1 R^3-weighted $Re[\chi(R)]$ plots from AIMD with those for the reference molecular geometries. **Figure 3-7** compares these same types of plots from AIMD with those from the experimental data for the series of Dy^{3+}, Er^{3+}, and Lu^{3+}. We briefly explain the rationale behind the use of an R^3-weighted representation of these radial structure plots. The R^3-weighting is used to accentuate the spatial structure at high-R that is due mostly to photoelectron multiple scattering from within the first shell. There is sufficient sampling in both theoretical and experimental data to faithfully capture these long-range distances with a high signal-to-noise ratio. The longer-R features ($R >$ 2.5 Å) in these $Re[\chi(R)]$ plots originate primarily from multiple scattering oscillations in the $\chi(k)$ spectrum in the region below $k = 8$ Å^{-1}. The signal-to-noise ratio (~ 10^3) in a typical EXAFS scan over the region from $1.5 < k < 8$ Å^{-1} is sufficiently high to justify the R^3-weighting used in these plots. For the AIMD EXAFS spectra, convergence tests were employed to ensure sufficient sampling (inclusion of 200 frames were deemed

sufficient) for low-noise spectra. This fact was also effectively demonstrated by comparing two $Re[\chi(R)]$ plots generated from a single trajectory using different scattering cutoff distances of 6.5 to 8.5 Å (FEFF parameter "RPATH") in which new *R* structure due to multiple scattering is observed between 5.5 to 7 Å when applying the longer cutoff distance.

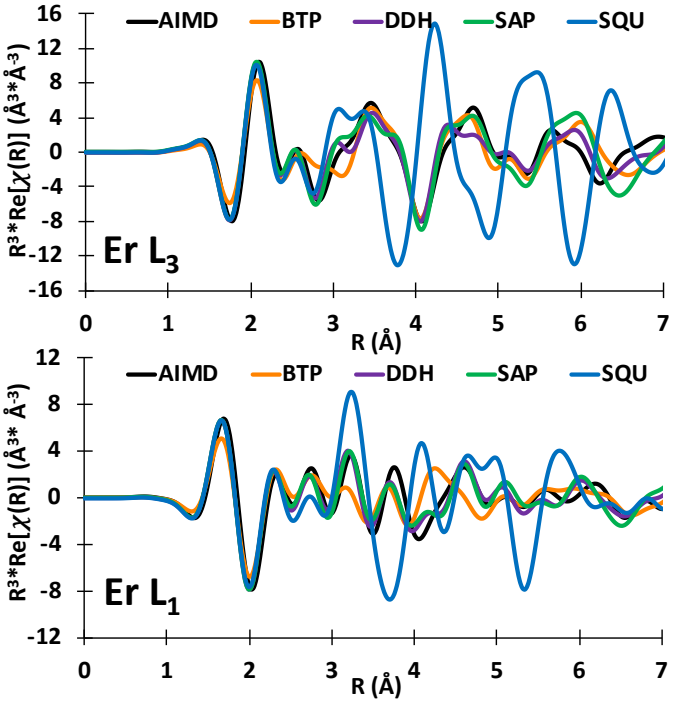

Figure 3-6: R^3-weighted $Re[\chi(R)]$ spectra generated from the Er^{3+} AIMD simulation and from the four different eight-coordinate reference molecular geometries (see Figure 3-4). For the reference molecular geometries, a universal setting of $\sigma^2 = 0.015$ Å^2 has been applied, as an approximation, to all multiple scattering paths, here as the first-shell single scattering paths were set to 0.007 Å. For AIMD, the σ^2 values were calculated exactly for the entire set of Ln-O configurations in the trajectory.

Figure 3-6 compares Er^{3+} L_3 and L_1 spectra that were calculated for the four eight-coordinate reference molecular geometries (**Figure 3-4**). Prior EXAFS studies for lanthanides have evaluated only the single scattering processes for the first shell that includes the region up to approximately 2.5 Å in this plot. It is clear to see from **Figure**

3-6, that in this region, the spectra for the reference molecular geometries are the nearly the same and hence they contain no information about the first-shell symmetry. In marked contrast, the multiple scattering region above 2.5 Å provides a unique and powerful method to differentiate molecular geometries. In **Figure 3-6**, the SQU geometry is completely different from that of the other geometries demonstrating the unique effect of collinear multiple scattering paths that are only present for SQU. In comparing both the L_3 and L_1 spectra, BTP has distinct features that clearly differentiate it from SAP and DDH. Finally, the differences between SAP and DDH are more nuanced but collectively the features allow some discrimination. From a comparison of the L_3 and L_1 spectra in **Figure 3-6**, it is also clear to see that the selection rules impose a different set of allowed transitions for these two edges. Hence, the structure of their multiple scattering spectra are completely different, illustrating the power of acquiring different edge spectra to provide independent measures of the local symmetry. Another important result illustrated in **Figure 3-6** is that better differentiation of the various symmetries occurs at higher R.

The EXAFS spectrum generated from AIMD (**Figure 3-6**) is exactly derived from the molecular geometries of the simulation and includes an ensemble average of equilibrium structures through a sampling of the trajectory structures. **Figure 3-6** compares the R^3-weighted $Re[\chi(R)]$ spectra from AIMD to those of the four reference molecular geometries. For the Er^{3+} aqua ion, the ADF suggests that the O-Ln-O values are most consistent with the SAP geometry, despite similar RMSD values to SAP, DDH, and BTP. However, multiple scattering EXAFS shows from the L_3 and L_1 AIMD spectra show the best agreement with either DDH or SAP or perhaps a mixture of the two. The R^3-weighted $Re[\chi(R)]$ spectra easily exclude the presence of SQU. Finally, AIMD could

also be represented by a smaller percentage of BTP in equilibrium with DDH and SAP. These conclusions are in general agreement with the relative prevalence of SAP, DDH and BTP from the RMSD values in **Table 3-3.** Overall, the EXAFS results agree with a room temperature speciation in which Ln^{3+} aqua ions, in solution, are dynamic and symmetrically disordered.

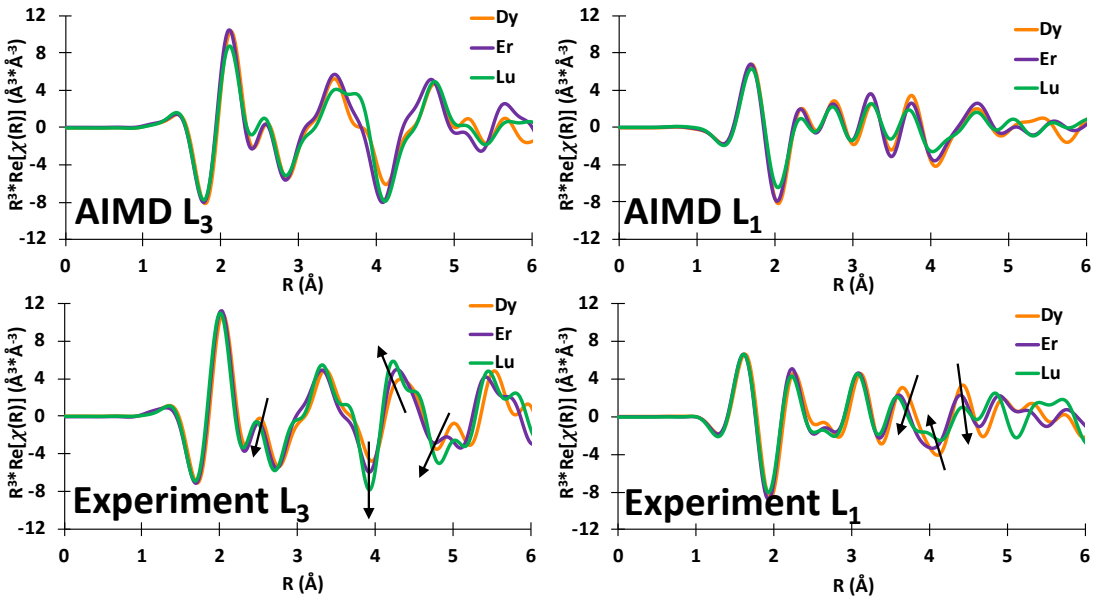

Figure 3-7. The Dy^{3+}, Er^{3+}, and Lu^{3+} L_3 and L_1 R^3-weighted $Re[\chi(R)]$ plots for AIMD and the experimental data. The vertical dashed lines identify common spectral features between the AIMD and the experimental spectra. The horizontal axis of the AIMD spectra has been scaled by 3% to account for the measured difference in the first shell Er-O distance (0.07 Å).

Figure 3-7 compares the L_3 and L_1 R^3–weighted $Re[\chi(R)]$ plots from AIMD with those from experiment. First, for the set of experimental spectra (lower panels), the spectral features are quite similar for the series of Dy^{3+}, Er^{3+}, and Lu^{3+} implying that, on an average, their local structures and associated symmetries are similar. Above ~3.5 Å, the experimental series show a modest progression of spectral features (see arrows in

Figure 3-7) in regions of the L_3 and L_1 spectra. Such changes could be ascribed to slight changes in the packing geometry with increasingly smaller ion radius (**Table 3-1**).

The EXAFS multiple-scattering spectra calculated from the AIMD simulations agree with the experimental spectra since there is a one-to-one correspondence for most of the spectral features. Thus, based upon the geometry analysis in **Figure 3-6**, this suggests that the dominant geometries for the experimental system are SAP and/or DDH. The results are also consistent with the RMSD analysis that shows that Dy^{3+} favors the DDH and SAP geometries, Er^{3+} favoring DDH, SAP, and BTH geometries, while Lu^{3+} being the most SAP-like of the three (**Table 3-3**). These results confirm the general symmetry structure predicted by the simulation.

3.4. Conclusions

In this work we examined the long-debated structure of Ln^{3+} aqua complexes by a combination of the first AIMD simulations of all fifteen Ln^{3+} complexes and EXAFS measurements, including multiple scattering at high *k*-values to assign local coordination geometry. Measured EXAFS spectra of four Ln^{3+} ions were compared with AIMD-generated EXAFS spectra, and we observe excellent agreement for the early lanthanides (Nd^{3+}), and acceptable (Ln-O bond lengths within < 0.07 Å) for the later ones (Dy^{3+}, Er^{3+}, Lu^{3+}). Analysis of the AIMD trajectories reveals that all Ln^{3+} aqua ions in solution have dynamic first coordination shells, which at room temperature, are symmetrically disordered. In short, solvated Ln^{3+} species do not possess a rigid molecular geometry, but rather are fluxional. Previously, the solution symmetry of Ln^{3+} ions has been inferred from experimentally measured Ln-O bond distances. In this work, multiple scattering

EXAFS spectra, from experimental measurements and AIMD simulations, are able to discriminate between different molecular geometries of the first coordination shells by measuring Ln-O distances and angular correlations, confirming that the Ln^{3+} aqua ions are subject to a dynamic solvation structure. This is the first time that the symmetry (i.e. Ln-O distances and angular correlations) of hydrating waters about Ln^{3+} has been experimentally measured by any technique thereby increasing our understanding about lanthanide coordination chemistry.

Chapter 3 References

(1) Kronholm, B.; Anderson, C. G.; Taylor, P. R. A Primer on Hydrometallurgical Rare Earth Separations. *Jom* **2013**, *65*, 1321–1326.

(2) Ferru, G.; Reinhart, B.; Bera, M. K.; Olvera De La Cruz, M.; Qiao, B.; Ellis, R. J. The Lanthanide Contraction beyond Coordination Chemistry. *Chem. - A Eur. J.* **2016**, *22*, 6899–6904.

(3) Qiao, B.; Muntean, J. V.; Olvera De La Cruz, M.; Ellis, R. J. Ion Transport Mechanisms in Liquid-Liquid Interface. *Langmuir* **2017**, *33*, 6135–6142.

(4) Baldwin, A. G.; Ivanov, A. S.; Williams, N. J.; Ellis, R. J.; Moyer, B. A.; Bryantsev, V. S.; Shafer, J. C. Outer-Sphere Water Clusters Tune the Lanthanide Selectivity of Diglycolamides. *ACS Cent. Sci.* **2018**, *4*, 739–747.

(5) Nakase, M.; Kobayashi, T.; Shiwaku, H.; Suzuki, S.; Grimes, T. S.; Mincher, B. J.; Yaita, T. Relationship Between Structure and Coordination Strength of N and N,O-Hybrid Donor Ligands with Trivalent Lanthanides. *Solvent Extr. Ion Exch.* **2018**, *36*, 633–646.

(6) Werner, E. J.; Biros, S. M. Supramolecular Ligands for the Extraction of Lanthanide and Actinide Ions. *Inorg. Chem. Front.* **2019**, *6*, 2067–2094.

(7) Healy, M. R.; Ivanov, A. S.; Karslyan, Y.; Bryantsev, V. S.; Moyer, B. A.; Jansone-Popova, S. Efficient Separation of Light Lanthanides(III) by Using Bis-Lactam Phenanthroline Ligands. *Chem. - A Eur. J.* **2019**, *25*, 6326–6331.

(8) Cheisson, T.; Schelter, E. J. Rare Earth Elements: Mendeleev's Bane, Modern Marvels. *Science (80-.).* **2019**, *363*, 489–493.

(9) Cotruvo, J. A. The Chemistry of Lanthanides in Biology: Recent Discoveries, Emerging Principles, and Technological Applications. *ACS Cent. Sci.* **2019**, *5*, 1496–1506.

(10) Liang, Z.; Bu, W.; Schweighofer, K. J.; Walwark, D. J.; Harvey, J. S.; Hanlon, G. R.; Amoanu, D.; Erol, C.; Benjamin, I.; Schlossman, M. L. Nanoscale View of Assisted Ion Transport across the Liquid–Liquid Interface. *Proc. Natl. Acad. Sci. U. S. A.* **2019**, *116*, 18227–18232.

(11) Hall, G. B.; Holfeltz, V. E.; Campbell, E. L.; Boglaienko, D.; Lumetta, G. J.; Levitskaia, T. G. Evolution of Acid-Dependent Am3+ and Eu3+ Organic Coordination Environment: Effects on the Extraction Efficiency. *Inorg. Chem.* **2020**, *59*, 4453–4467.

(12) Raymond, K. N.; Pierre, V. C. Next Generation, High Relaxivity Gadolinium MRI Agents. *Bioconjug. Chem.* **2005**, *16*, 3–8.

(13) Thiele, N. A.; Woods, J. J.; Wilson, J. J. Implementing F-Block Metal Ions in Medicine: Tuning the Size Selectivity of Expanded Macrocycles. *Inorg. Chem.* **2019**, *58*, 10483–10500.

(14) Molloy, J. K.; Nonat, A. M.; O'Brien, J. E.; Brougham, D. F.; Gunnlaugsson, T. Self-Assembled Ln(III) Cyclen-Based Micelles and AuNPs Conjugates as Candidates for Luminescent and Magnetic Resonance Imaging (MRI) Agents. *Supramol. Chem.* **2020**, *0*, 1–10.

(15) Woodruff, D. N.; Winpenny, R. E. P.; Layfield, R. A. Lanthanide Single-Molecule Magnets. *Chem. Rev.* **2013**, *113*, 5110–5148.

(16) Liddle, S. T.; Van Slageren, J. Improving F-Element Single Molecule Magnets. *Chem. Soc. Rev.* **2015**, *44*, 6655–6669.
(17) Kitchen, J. A. Lanthanide-Based Self-Assemblies of 2,6-Pyridyldicarboxamide Ligands: Recent Advances and Applications as next-Generation Luminescent and Magnetic Materials. *Coord. Chem. Rev.* **2017**, *340*, 232–246.
(18) Guo, F. S.; Day, B. M.; Chen, Y. C.; Tong, M. L.; Mansikkamäki, A.; Layfield, R. A. Magnetic Hysteresis up to 80 Kelvin in a Dysprosium Metallocene Single-Molecule Magnet. *Science (80-.).* **2018**, *362*, 1400–1403.
(19) Ullah, A.; Cerdá, J.; Baldoví, J. J.; Varganov, S. A.; Aragó, J.; Gaita-Ariño, A. In Silico Molecular Engineering of Dysprosocenium-Based Complexes to Decouple Spin Energy Levels from Molecular Vibrations. *J. Phys. Chem. Lett.* **2019**, *10*, 7678–7683.
(20) De Bettencourt-Dias, A. Lanthanide-Based Emitting Materials in Light-Emitting Diodes. *J. Chem. Soc. Dalt. Trans.* **2007**, No. 22, 2229–2241.
(21) Eliseeva, S. V; Bünzli, J.-C. G. Lanthanide Luminescence for Functional Materials and Bio-Sciences. *Chem. Soc. Rev.* **2010**, *39*, 189–227.
(22) Binnemans, K. Lanthanide-Based Luminescent Hybrid Materials. *Chem. Rev.* **2009**, *109*, 4283–4374.
(23) Monteiro, J. H. S. K.; De Bettencourt-Dias, A.; Sigoli, F. A. Estimating the Donor-Acceptor Distance to Tune the Emission Efficiency of Luminescent Lanthanide Compounds. *Inorg. Chem.* **2017**, *56*, 709–712.
(24) Zanoni, K. P. S.; Ravaro, L. P.; De Camargo, A. S. S. Host-Guest Luminescent Materials Based on Highly Emissive Species Loaded into Versatile Sol-Gel Hosts. *Dalt. Trans.* **2018**, *47*, 12813–12826.
(25) Wang, J.; Suffren, Y.; Daiguebonne, C.; Freslon, S.; Bernot, K.; Calvez, G.; Le Pollès, L.; Roiland, C.; Guillou, O. Multi-Emissive Lanthanide-Based Coordination Polymers for Potential Application as Luminescent Bar-Codes. *Inorg. Chem.* **2019**, *58*, 2659–2668.
(26) Cotton, S. A. Lanthanides: Comparison to 3d Metals. In *Encyclopedia of Inorganic and Bioinorganic Chemistry*; American Cancer Society, 2012.
(27) Sessa, F.; D'Angelo, P.; Migliorati, V. Combined Distribution Functions: A Powerful Tool to Identify Cation Coordination Geometries in Liquid Systems. *Chem. Phys. Lett.* **2018**, *691*, 437–443.
(28) Habenschuss, A.; Spedding, F. H. The Coordination (Hydration) of Rare Earth Ions in Aqueous Chloride Solutions from x-Ray Diffraction. II. LaCI3, PrCI3, and NdCI3. *J. Chem. Phys.* **1979**, *70*, 3758–3763.
(29) Habenschuss, A.; Spedding, F. H. The Coordination (Hydration) of Rare Earth Ions in Aqueous Chloride Solutions from x-Ray Diffraction. I. TbCI3, DyCI3, ErCI3, TmCI3, and LuCI3. *J. Chem. Phys.* **1979**, *70*, 2797–2806.
(30) Habenschuss, A.; Spedding, F. H. The Coordination (Hydration) of Rare Earth Ions in Aqueous Chloride Solutions from x-Ray Diffraction. III. SmCl3, EuCl3, and Series Behavior. *J. Chem. Phys.* **1980**, *73*, 442–450.
(31) Rizkalla, E. N.; Choppin, G. R. Chapter 127 Lanthanides and Actinides Hydration and Hydrolysis. In *Handbook on the Physics and Chemistry of Rare Earths*; Elsevier, 1994; Vol. 18, pp 529–558.

(32) Kowall, T. H.; Foglia, F.; Helm, L.; Merbach, A. E. Molecular Dynamics Simulation Study of Lanthanide Ions Ln3+in Aqueous Solution Including Water Polarization. Change in Coordination Number from 9 to 8 along the Series. *J. Am. Chem. Soc.* **1995**, *117*, 3790–3799.
(33) Kowall, T.; Foglia, F.; Helm, L.; Merbach, A. E. Mechanisms of Water Exchange between Lanthanide(II) Aqua Ions [Ln(H 2O)n]3+ and Bulk Water: A Molecular Dynamics Simulation Approach Including High-Pressure Effects. *Chem. - A Eur. J.* **1996**, *2*, 285–294.
(34) Aime, S.; Barge, A.; Botta, M.; De Sousa, A. S.; Parker, D. Direct NMR Spectroscopic Observation of a Lanthanide-Coordinated Water Molecule Whose Exchange Rate Is Dependent on the Conformation of the Complexes. *Angew. Chemie - Int. Ed.* **1998**, *37*, 2673–2675.
(35) Yaita, T.; Narita, H.; Suzuki, S.; Tachimori, S.; Motohashi, H.; Shiwaku, H. Structural Study of Lanthanides(III) in Aqueous Nitrate and Chloride Solutions by EXAFS. *J. Radioanal. Nucl. Chem.* **1999**, *239*.
(36) Helm, L.; Merbach, A. E. Water Exchange on Metal Ions: Experiments and Simulations. *Coord. Chem. Rev.* **1999**, *187*, 151–181.
(37) Allen, P. G.; Bucher, J. J.; Shuh, D. K.; Edelstein, N. M.; Craig, I. Coordination Chemistry of Trivalent Lanthanide and Actinide Ions in Dilute and Concentrated Chloride Solutions. *Inorg. Chem.* **2000**, *39*, 595–601.
(38) Floris, F. M.; Tani, A. A Study of Aqueous Solutions of Lanthanide Ions by Molecular Dynamics Simulation with Ab Initio Effective Pair Potentials. *J. Chem. Phys.* **2001**, *115*, 4750–4765.
(39) Parker, D.; Dickins, R. S.; Puschmann, H.; Crossland, C.; Howard, J. A. K. Being Excited by Lanthanide Coordination Complexes: Aqua Species, Chirality, Excited-State Chemistry, and Exchange Dynamics. *Chem. Rev.* **2002**, *102*, 1977–2010.
(40) Helm, L.; Merbach, A. E. Inorganic and Bioinorganic Solvent Exchange Mechanisms. *Chem. Rev.* **2005**, *105*, 1923–1959.
(41) Hughes, S. R.; Nguyen, T. N.; Capobianco, J. A.; Peslherbe, G. H. A Theoretical Study of Trivalent Lanthanide Ion Microsolvation in Water Clusters from First Principles. *Int. J. Mass Spectrom.* **2005**, *241*, 283–294.
(42) Persson, I.; D'Angelo, P.; De Panfilis, S.; Sandström, M.; Eriksson, L. Hydration of Lanthanoid(III) Ions in Aqueous Solution and Crystalline Hydrates Studied by EXAFS Spectroscopy and Crystallography: The Myth of the "Gadolinium Break." *Chem. - A Eur. J.* **2008**, *14*, 3056–3066.
(43) Duvail, M.; Spezia, R.; Vitorge, P. A Dynamic Model to Explain Hydration Behaviour along the Lanthanide Series. *ChemPhysChem* **2008**, *9*, 693–696.
(44) Duvail, M.; Vitorge, P.; Spezia, R. Building a Polarizable Pair Interaction Potential for Lanthanoids(III) in Liquid Water: A Molecular Dynamics Study of Structure and Dynamics of the Whole Series. *J. Chem. Phys.* **2009**, *130*.
(45) Duvail, M.; D'Angelo, P.; Gaigeot, M. P.; Vitorge, P.; Spezia, R. What First Principles Molecular Dynamics Can Tell Us about EXAFS Spectroscopy of Radioactive Heavy Metal Cations in Water. *Radiochim. Acta* **2009**, *97*, 339–346.
(46) Duvail, M.; Ruas, A.; Venault, L.; Moisy, P.; Guilbaud, P. Molecular Dynamics Studies of Concentrated Binary Aqueous Solutions of Lanthanide Salts: Structures

and Exchange Dynamics. *Inorg. Chem* **2010**, *49*, 519–530.
(47) Dangelo, P.; Zitolo, A.; Migliorati, V.; Chillemi, G.; Duvail, M.; Vitorge, P.; Abadie, S.; Spezia, R. Revised Ionic Radii of Lanthanoid(III) Ions in Aqueous Solution. *Inorg. Chem.* **2011**, *50*, 4572–4579.
(48) Marjolin, A.; Gourlaouen, C.; Clavaguera, C.; Ren, P. Y. Y.; Piquemal, J. P.; Dognon, J. P. Hydration Gibbs Free Energies of Open and Closed Shell Trivalent Lanthanide and Actinide Cations from Polarizable Molecular Dynamics. *J. Mol. Model* **2014**, *20*, 7.
(49) Sessa, F.; Spezia, R.; D'Angelo, P. Lutetium(Iii) Aqua Ion: On the Dynamical Structure of the Heaviest Lanthanoid Hydration Complex. *J. Chem. Phys.* **2016**, *144*, 204505.
(50) Morales, N.; Galbis, E.; Martínez, J. M.; Pappalardo, R. R.; Sánchez Marcos, E. Identifying Coordination Geometries of Metal Aquaions in Water: Application to the Case of Lanthanoid and Actinoid Hydrates. *J. Phys. Chem. Lett.* **2016**, *7*, 4275–4280.
(51) Migliorati, V.; Serva, A.; Terenzio, F. M.; D'Angelo, P. Development of Lennard-Jones and Buckingham Potentials for Lanthanoid Ions in Water. *Inorg. Chem.* **2017**, *56*, 6214–6224.
(52) Qiao, B.; Skanthakumar, S.; Soderholm, L. Comparative CHARMM and AMOEBA Simulations of Lanthanide Hydration Energetics and Experimental Aqueous-Solution Structures. *J. Chem. Theory Comput.* **2018**, *14*, 1781–1790.
(53) Yamaguchi, T.; Nomura, M.; Wakita, H.; Ohtaki, H. An Extended X-Ray Absorption Fine Structure Study of Aqueous Rare Earth Perchlorate Solutions in Liquid and Glassy States. *J. Chem. Phys.* **1988**, *89*, 5153–5159.
(54) Clark, A. E. Density Functional and Basis Set Dependence of Hydrated Ln(III) Properties. *J. Chem. Theory Comput.* **2008**, *4*, 708–718.
(55) Lee, P. A.; Pendry, J. B. Theory of the Extended X-Ray Absorption Fine Structure. *Phys. Rev. B* **1975**, *11*, 2795–2811.
(56) Bunker, G.; Stern, E. A. Experimental Study of Multiple Scattering in X-Ray Absorption near Edge Structure. *Phys. Rev. Lett.* **2000**, *84*, 5237.
(57) Di Cicco, A. EXAFS Multiple-Scattering Data-Analysis: GNXAS Methodology and Applications. *Phys. B Phys. Condens. Matter* **1995**, *208–209*, 125–128.
(58) Fulton, J. L.; Bylaska, E. J.; Bogatko, S.; Balasubramanian, M.; Cauët, E.; Schenter, G. K.; Weare, J. H. Near-Quantitative Agreement of Model-Free DFT-MD Predictions with XAFS Observations of the Hydration Structure of Highly Charged Transition-Metal Ions. *J. Phys. Chem. Lett.* **2012**, *3*, 2588–2593.
(59) Fulton, J. L.; Kathmann, S. M.; Schenter, G. K.; Balasubramanian, M. Hydrated Structure of Ag(I) Ion from Symmetry-Dependent, K- and L-Edge XAFS Multiple Scattering and Molecular Dynamics Simulations. *J. Phys. Chem. A* **2009**, *113*, 13976–13984.
(60) Kuzmin, A.; Purans, J.; Benfatto, M.; Natoli, C. R. X-Ray-Absorption Study of Rhenium L3 and L1 Edges in ReO3: Multiple-Scattering Approach. *Phys. Rev. B* **1993**, *47*, 2480–2486.
(61) Rehr, J. J.; Albers, R. C. Theoretical Approaches to X-Ray Absorption Fine Structure. *Rev. Mod. Phys.* **2000**, *72*, 621–654.

(62) Rehr, J. J.; Kas, J. J.; Prange, M. P.; Sorini, A. P.; Takimoto, Y.; Vila, F. Ab Initio Theory and Calculations of X-Ray Spectra. *C. R. Phys* **2009**, *10*, 548–559.
(63) Rehr, J. J.; Kas, J. J.; Vila, F. D.; Prange, M. P.; Jorissen, K. Parameter-Free Calculations of X-Ray Spectra with FEFF9. *Phys. Chem. Chem. Phys.* **2010**, *12*, 5503–5513.
(64) Durand, S.; Dognon, J. P.; Guilbaud, P.; Rabbe, C.; Wipff, G. Lanthanide and Alkaline-Earth Complexes of EDTA in Water: A Molecular Dynamics Study of Structures and Binding Selectivities. *J. Chem. Soc. Trans.* **2000**, *2*, 705–714.
(65) Finney, A. R.; Lectez, S.; Freeman, C. L.; Harding, J. H.; Stackhouse, S. Ion Association in Lanthanide Chloride Solutions. *Chem. -Eur. J* **2019**, *25*, 8725–8740.
(66) Zhang, J.; Dolg, M. Labile Capping Bonds in Lanthanide(III) Complexes: Shorter and Weaker. *J. Phys. Chem. A* **2015**, *119*, 774–780.
(67) Zhang, J.; Heinz, N.; Dolg, M. Understanding Lanthanoid(III) Hydration Structure and Kinetics by Insights from Energies and Wave Functions. *Inorg. Chem.* **2014**, *53*, 7700–7708.
(68) Goedecker, S.; Teter, M.; Hutter, J. Separable Dual-Space Gaussian Pseudopotentials. *Phys. Rev. B - Condens. Matter Mater. Phys* **1996**, No. 54, 1703–1710.
(69) Lippert, G.; Hutter, J.; Parrinello, M. A Hybrid Gaussian and Plane Wave Density Functional Scheme. *Mol. Phys* **1997**, *92*, 477–488.
(70) Lu, J. B.; Cantu, D. C.; Nguyen, M. T.; Li, J.; Glezakou, V. A.; Rousseau, R. Norm-Conserving Pseudopotentials and Basis Sets to Explore Lanthanide Chemistry in Complex Environments. *J. Chem. Theory Comput.* **2019**, *15*, 5987–5997.
(71) Cao, X.; Dolg, M. Valence Basis Sets for Relativistic Energy-Consistent Small-Core Lanthanide Pseudopotentials. *J. Chem. Phys.* **2001**, *115*, 7348–7355.
(72) Weigand, A.; Cao, X.; Yang, J.; Dolg, M. Quasirelativistic F-in-Core Pseudopotentials and Core-Polarization Potentials for Trivalent Actinides and Lanthanides: Molecular Test for Trifluorides. *Theor. Chem* **2010**, *126*, 117–127.
(73) Ross, R. B.; Gayen, S.; Ermler, W. C. Ab Initio Relativistic Effective Potentials with Spin-Orbit Operators. *J. Chem. Phys.* **1994**, *100*, 8145–8155.
(74) Cundari, T. R.; Stevens, W. J. Effective Core Potential Methods for the Lanthanides. *J. Chem. Phys.* **1993**, *98*, 5555–5565.
(75) Hay, P. J.; Wadt, W. R. Ab Initio Effective Core Potentials for Molecular Calculations. Potentials for the Transition Metal Atoms Sc to Hg. *J. Chem. Phys.* **1985**, *82*, 270–283.
(76) Dolg, M.; Stoll, H. Pseudopotential Study of the Rare Earth Monohydrides, Monoxides and Monofluorides. *Theor. Chim. Acta* **1989**, *75*, 369–387.
(77) Dolg, M.; Stoll, H.; Preuss, H. Energy-Adjusted Ab Initio Pseudopotentials for the Rare Earth Elements. *J. Chem. Phys.* **1989**, *90*, 1730–1734.
(78) Cao, X.; Zhang, J.; Weissmann, D.; Dolg, M.; Chen, X. Accurate Quantum Chemical Modelling of the Separation of Eu3+ from Am3+/Cm3+ by Liquid-Liquid Extraction with Cyanex272. *Phys. Chem* **2015**, *17*, 20605–20616.
(79) Huang, P. W.; Wang, C. Z.; Wu, Q. Y.; Lan, J. H.; Song, G.; Chai, Z. F.; Shi, W.

Q. Theoretical Studies on the Synergistic Extraction of Am3+ and Eu3+ with CMPO-HDEHP and CMPO-HEH[EHP] Systems. *Dalt* **2018**, *47*, 5474–5482.

(80) Fuggle, J. C.; Inglesfield, J. E. *Unoccupied Electronic States*; Springer-Verlag: New York.

(81) Perdew, J. P.; Burke, K.; Ernzerhof, M. Generalized Gradient Approximation Made Simple. *Phys. Rev. Lett.* **1996**, *77*, 3865–3868.

(82) Lin, I. C.; Seitsonen, A. P.; Tavernelli, I.; Rothlisberger, U. Structure and Dynamics of Liquid Water from Ab Initio Molecular Dynamics-Comparison of BLYP, PBE, and RevPBE Density Functionals with and without van Der Waals Corrections. *J. Chem. Theory Comput.* **2012**, *8*, 3902–3910.

(83) Chen, M.; Ko, H. Y.; Remsing, R. C.; Calegari Andrade, M. F.; Santra, B.; Sun, Z.; Selloni, A.; Car, R.; Klein, M. L.; Perdew, J. P.; Wu, X. Ab Initio Theory and Modeling of Water. *Proc. Natl. Acad. Sci. U. S. A.* **2017**, *114*, 10846–10851.

(84) Grimmel, S.; Schoendorff, G.; Wilson, A. K. Gauging the Performance of Density Functionals for Lanthanide-Containing Molecules. *J. Chem. Theory Comput.* **2016**, *12*, 1259–1266.

(85) Jaoul, A.; Nocton, G.; Clavaguéra, C. Assessment of Density Functionals for Computing Thermodynamic Properties of Lanthanide Complexes. *ChemPhysChem* **2017**, *18*, 2688–2696.

(86) Hutter, J.; Iannuzzi, M.; Schiffmann, F.; Vandevondele, J. Cp2k: Atomistic Simulations of Condensed Matter Systems. *Wiley Interdiscip. Rev. Comput. Mol. Sci.* **2014**, *4*, 15–25.

(87) VandeVondele, J.; Krack, M.; Mohamed, F.; Parrinello, M.; Chassaing, T.; Hutter, J.; Fast, Q. Fast and Accurate Density Functional Calculations Using a Mixed Gaussian and Plane Waves Approach. *Comput. Phys. Commun.* **2005**, *167*, 103–128.

(88) VandeVondele, J.; Hutter, J. Gaussian Basis Sets for Accurate Calculations on Molecular Systems in Gas and Condensed Phases. *J. Chem. Phys.* **2007**, *127*.

(89) Grimme, S.; Antony, J.; Ehrlich, S.; Krieg, H. A Consistent and Accurate Ab Initio Parametrization of Density Functional Dispersion Correction (DFT-D) for the 94 Elements H-Pu. *J. Chem. Phys.* **2010**, *132*.

(90) Kepert, D. The Stereochemistry of Eight Coordination. *J. Chem. Soc.* **1965**, 4736–4744.

(91) Burdett, J. K.; Hoffmann, R.; Fay, R. C. Eight-Coordination. *Inorg. Chem.* **1978**, *17*.

(92) Schenter, G. .; Fulton, J. L. XAFS Techniques for Catalysts, Nanomaterials and Surfaces; Iwasawa, I., Asakura, K., Tada, M., Eds.; Springer, 2017; pp 251–270.

(93) Ferrier, M. G.; Stein, B. W.; Batista, E. R.; Berg, J. M.; Birnbaum, E. R.; Engle, J. W.; John, K. D.; Kozimor, S. A.; Lezama Pacheco, J. S.; Redman, L. N. Synthesis and Characterization of the Actinium Aquo Ion. *ACS Cent. Sci.* **2017**, *3*, 176–185.

(94) Palmer, B. J.; Pfund, D. M.; Fulton, J. L. Direct Modeling of EXAFS Spectra from Molecular Dynamics Simulations. *J. Phys* **1996**, *100*, 13393–13398.

(95) Rousseau, R.; Schenter, G. K.; Fulton, J. L.; Linehan, J. C.; Engelhard, M. H.; Autrey, T. Defining Active Catalyst Structure and Reaction Pathways from Ab Initio Molecular Dynamics and Operando XAFS: Dehydrogenation of

Dimethylaminoborane by Rhodium Clusters. *J. Am. Chem. Soc.* **2009**, *131*, 10516–10524.

(96) Solera, J. A.; García, J.; Proietti, M. G. Multielectron Excitations at the L Edges in Rare-Earth Ionic Aqueous Solutions. *Phys. Rev. B* **1995**, *51*, 2678–2686.

(97) Zhang, K.; Stern, E. A.; Rehr, J. J.; Ellis, F. Double Electron Excitation in Atomic Xe. *Phys. Rev. B* **1991**, *44*, 2030–2039.

(98) Spedding, F. H.; Pikal, M. J.; Ayers, B. O. Apparent Molal Volumes of Some Aqueous Rare Earth Chloride and Nitrate Solutions at 25°. *J. Phys. Chem.* **1966**, *70*, 2440–2449.

(99) D'Angelo, P.; Zitolo, A.; Migliorati, V.; Persson, I. Analysis of the Detailed Configuration of Hydrated Lanthanoid(III) Ions in Aqueous Solution and Crystalline Salts by Using K- And L3-Edge XANES Spectroscopy. *Chem. - A Eur. J.* **2010**, *16*, 684–692.

Supporting Information for Chapter 3

Table. 3-S1 Ln^{3+} electronic configuration and multiplicities

Ln^{3+}	Electronic configuration	Multiplicity
La	$5s^25p^6$	1
Ce	$4f^1$	2
Pr	$4f^2$	3
Nd	$4f^3$	4
Pm	$4f^4$	5
Sm	$4f^5$	6
Eu	$4f^6$	7
Gd	$4f^7$	8
Tb	$4f^8$	7
Dy	$4f^9$	6
Ho	$4f^{10}$	5
Er	$4f^{11}$	4
Tm	$4f^{12}$	3
Yb	$4f^{13}$	2
Lu	$4f^{14}$	1

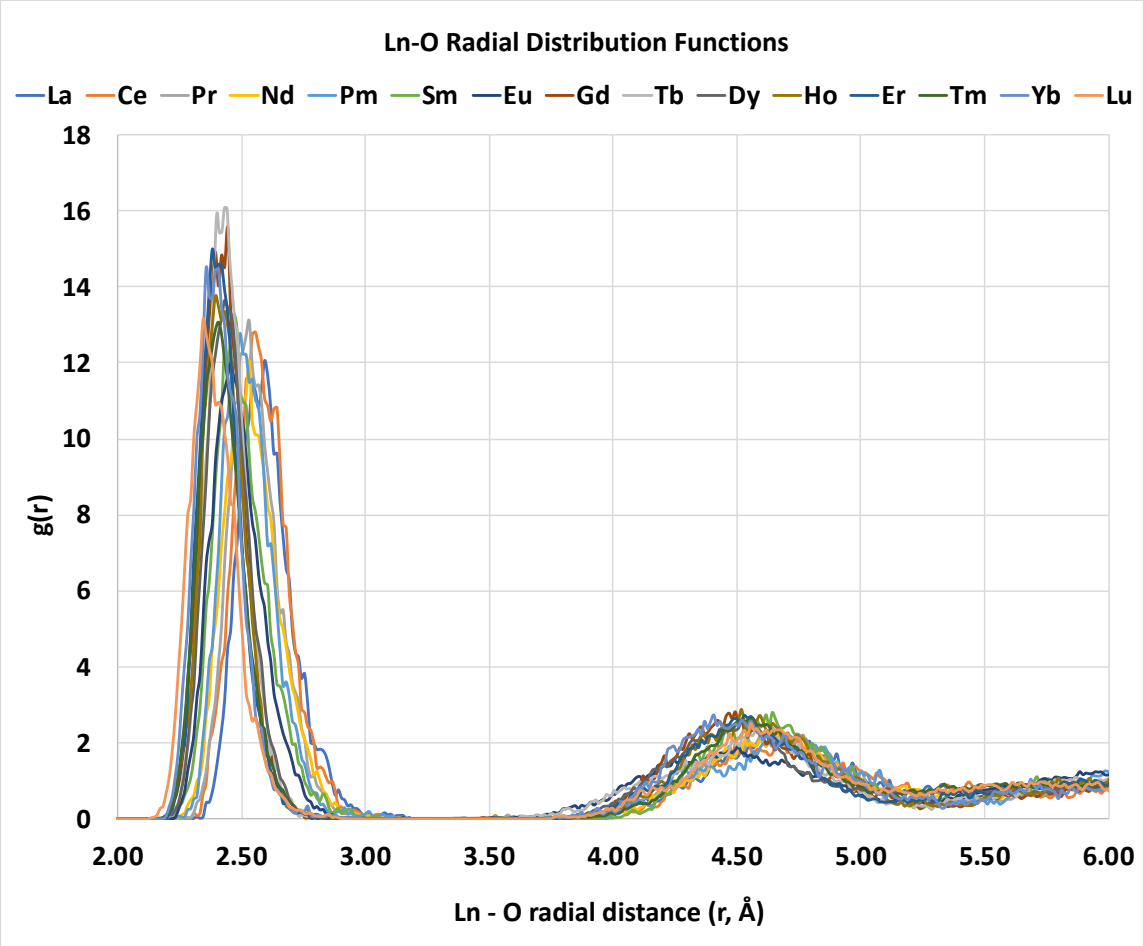

Figure 3-S1. The plot of all radial distribution functions of the Ln^{3+} aqua ion AIMD DFT simulations.

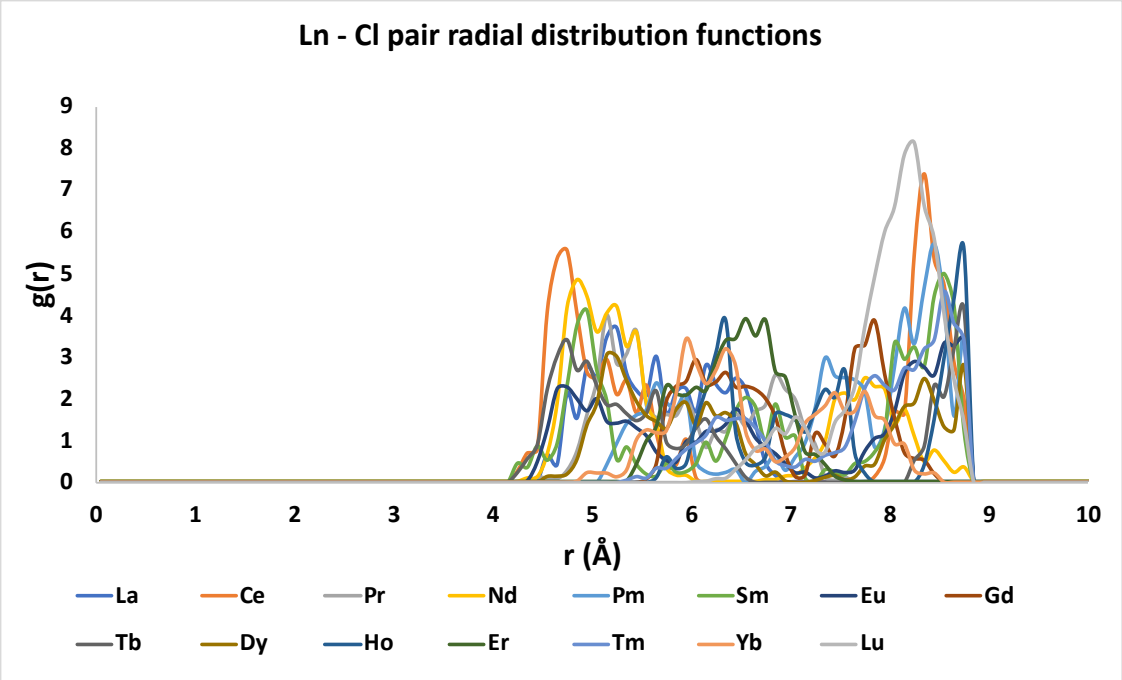

Figure 3-S2. A plot of all Ln – Cl radial distribution functions from AIMD simulations.

CHAPTER 4

Ionic contraction across the lanthanide series decreases the temperature-induced disorder of the water coordination sphere

Richard C. Shiery[1], John L. Fulton[2], David C. Cantu[1]

[1]*Department of Chemical and Materials Engineering, University of Nevada, Reno*

[2]*Physical Sciences Division, Pacific Northwest National Laboratory*

An excerpt of a paper published in *Inorganic Chemistry, 61, 287 – 294.*

Title of the full paper: Ionic contraction across the lanthanide series decreases the temperature-induced disorder of the water coordination sphere

Authors of the full paper: Darren M. Driscoll[2], Richard C. Shiery[1], Mahalingam Balasubramanian[2], John L. Fulton[3], David C. Cantu[1]

[1]*Department of Chemical and Materials Engineering, University of Nevada, Reno*

[2]*Advanced Photon Source, Argonne National Laboratory*

[3]*Physical Sciences Division, Pacific Northwest National Laboratory,*

4.1. Introduction

Probing the structure of aqueous lanthanide (Ln) ions with changes in temperature provides key insights into the factors controlling various first coordination sphere structures. Since the Ln properties of interest (e.g., ligand binding strength, luminescence, coordination, catalytic rates) depend on molecular structure, resolving if and how temperature changes Ln-containing structures is important to determine how these fundamental properties will be affected. For example it has been shown that i) the stability constants of Ln-ligand complexes change with temperature,[1] the intensity of emission spectra of Ln-ligand complexes show significant changes with temperature;[2] iii) the Ln coordination structure in peptides is flexible, sensitive and changes for different Ln^{3+} ions;[3] and iv) the structure of Ln-ligand catalysts affects redox reactions.[4] The associated applications will likely also be impacted or controlled by temperature-induced structural changes, including i) separations in which temperature affects Ln extraction;[5,6] ii) non-invasive nanothermometers, where it is desirable to have Ln-ligand complexes with highly temperature-sensitive dependence of their luminescent properties;[7,8] iii) synthetic peptides for Ln^{3+} binding, which could change binding affinity to a particular Ln^{3+} ion with temperature, and iv) Ln homogeneous catalysts reaction rates, which may vary according to changes in the catalyst structure due to temperature.

Temperature affects Ln-ligand structures in different ways that depends upon complex interactions between different ligands, anions, and solvent molecules. For this reason, the relative simplicity of aqua Ln^{3+} ions make them well suited to assess the structural changes of these cations with temperature. Here we describe how temperature

changes the first- and second-coordination spheres about Ce^{3+}, Sm^{3+}, and Lu^{3+} aqua ions that were selected from the center and the two endpoints of the Ln series.

Computationally, the coordination structures of the Ln aqua ions have been studied with electronic structure calculations,[9–11] *ab initio* molecular dynamics simulations,[12–15] and classical molecular dynamics simulations.[16,17,26–30,18–25] Experimentally, their structures have been resolved with X-ray diffraction,[31–33] X-ray absorption spectroscopy,[34–38] and excitation and emission spectroscopy.[39] Most computational and experimental studies on the structure of Ln aqua ions have been done at room temperature, although the temperature dependence of water exchange rates has been investigated with classical molecular dynamics.[26] There are studies that report the structure of Ln aqua ions in different phases: between liquid and frozen water,[39] crystal and solution phases,[38] hydrated in liquid water and solidified with ligands,[36] and water liquid and glassy states.[34] In this work, we focus on the effect of temperature on the coordination structure of Ln ions in liquid water.

Temperature dependent extended X-ray absorption fine structure (EXAFS) measurements of ions have been employed extensively to describe atomic structure within solutions.[40,41] Temperature induced structural transitions in both geometry and coordination have been shown to occur in a variety of metal ion-based solutions.[42–44] These solvation and structural transitions can be captured and quantified through element-specific EXAFS measurements. Specifically, EXAFS is highly sensitive to changes in bond lengths, solvation geometry and speciation through analysis of the photoelectron scattering paths.

This work reports a combination of *ab initio* molecular dynamics (AIMD) simulations and predicted EXAFS spectra from AIMD simulations, that were used to determine how temperature affects the structure of the first and second coordination spheres of the Ce^{3+}, Sm^{3+}, and Lu^{3+} ions in liquid water.

4.2. Methods

4.2.1. Ab initio molecular dynamics simulations

Previously we simulated all Ln^{3+} aqua ions in water, at 25 °C, using density functional theory (DFT) level AIMD simulations: predicted Ln-O distances are within ~0.05 Å from those measured with EXAFS.[12] In this work, we took room-temperature equilibrated frames from the Ce^{3+}, Sm^{3+}, and Lu^{3+} trajectories and ran AIMD simulations at 90 °C to determine how temperature affects the structure of their first coordination spheres.

DFT-level AIMD simulations were done in the PBE functional[45] using the CP2K package.[46,47] Core electrons were modeled with norm-conserving GTH pseudopotentials,[48] valence electrons were modelled with polarizable double-zeta basis sets,[49] and our LnPP1 pseudopotentials and basis sets[50] were used for Ce^{3+}, Sm^{3+}, and Lu^{3+}. Long range electrostatic terms were determined with a supplementary plane wave basis set,[51] using a 500 Ry cutoff for Ce and Sm, and 1000 Ry Lu. Grimme's D3 corrections[52] were used to account for van der Waals interactions within a 6.0 Å radius in all simulations. Ln Multiplicities were assigned with Hund's rule, see **Table 4-S1** of the Supporting Information.

AIMD simulations were done in periodic boundary conditions with cubic boxes having a length of 12.42 Å, with 64 explicit water molecules, which corresponds to a density of 0.998 g/mL. Three Cl^- anions were added to neutralize the charge of the Ln^{3+} cations. AIMD simulations were done in the canonical (NVT) ensemble at 90 °C with 1 fs time steps. The simulations were performed until at least 10 ps of simulation with a stable potential were observed, which were used to calculate Ln-O radial distribution functions (RDFs), O-Ln-O angle distribution functions (ADFs), calculate root mean square distances (RMSDs) to ideal geometries, and to predict EXAFS spectra.

4.2.2. Predicted extended X-ray absorption fine structure spectra

The EXAFS photoelectron single-scattering process provides a simple and accurate measure of the first-shell Ln-O distances. EXAFS spectra can be predicted from molecular dynamics simulations.[53] Comparing predicted and measured EXAFS spectra has been done to determine the coordination structure of heavy elements.[12,54] To directly compare with measured EXAFS spectra, we predicted $\chi(k)$ spectra from AIMD trajectories,[55] using FEFF8.5.[56] The Ln and O coordinates from 200 equispaced frames from equilibrated AIMD trajectories were used to generate ensemble average spectra. An AIMD-EXAFS spectrum[53,55,57] is generated for each frame and ensemble-average spectra resulted from the 200 frames of each case. FEFF8.5 was adjusted to include up to 35,000 paths. Only Ln and O atoms were included in FEFF calculations because the inclusion of H atoms results in a large number of scattering paths that fail to converge. The Hedin-Lundqvist exchange-correlation potential (default for FEFF8.5) was used with no SCF.

4.3. Results

Figure 4-1 includes the radial distribution functions (RDFs) from the AIMD simulations of the Ce^{3+}, Sm^{3+}, and Lu^{3+} aqua ions, at 25 °C and 90 °C. As expected, the increase in temperature resulted in shorter, broader peaks in the oxygen – oxygen RDFs in all cases (**Figure 4-1**, RHS). However, temperature had a much less pronounced effect on Ln-O RDFs (**Figure 4-1**, LHS). The first peak of Ce- and Sm-O distances shows slightly lower Ln-O distances at 90 °C than at 25 °C, which is counterintuitive. This can be explained by the fact that the Ce^{3+} and Sm^{3+} aqua ions changed their coordination number: they are 9-coordinate in the 25 °C AIMD simulations but 8-coordinate in the 90 °C AIMD simulations. The rearrangement of the second coordination sphere due to the change in coordination number in the first sphere also explains why temperature seemingly does not change the second peak in the Ce- and Sm-O RDFs: in simulation, the second sphere effects of temperature and change in coordination number average out.

On the other hand, the Lu^{3+} aqua ion remained 8-coordinate at 90 °C. This allows to isolate the effect of temperature on the structure of the first and second solvation sphere without a change in coordination number. The Lu-O RDF shows an almost identical first peak at 25 °C and 90 °C, but the second peak is broader at 90 °C than at 25 °C (**Figure 4-1**, LHS, bottom row). This implies that temperature has almost no effect on the first coordination sphere of the Lu^{3+} ion, which is somewhat unexpected, but it did make the second sphere more disordered, as expected.

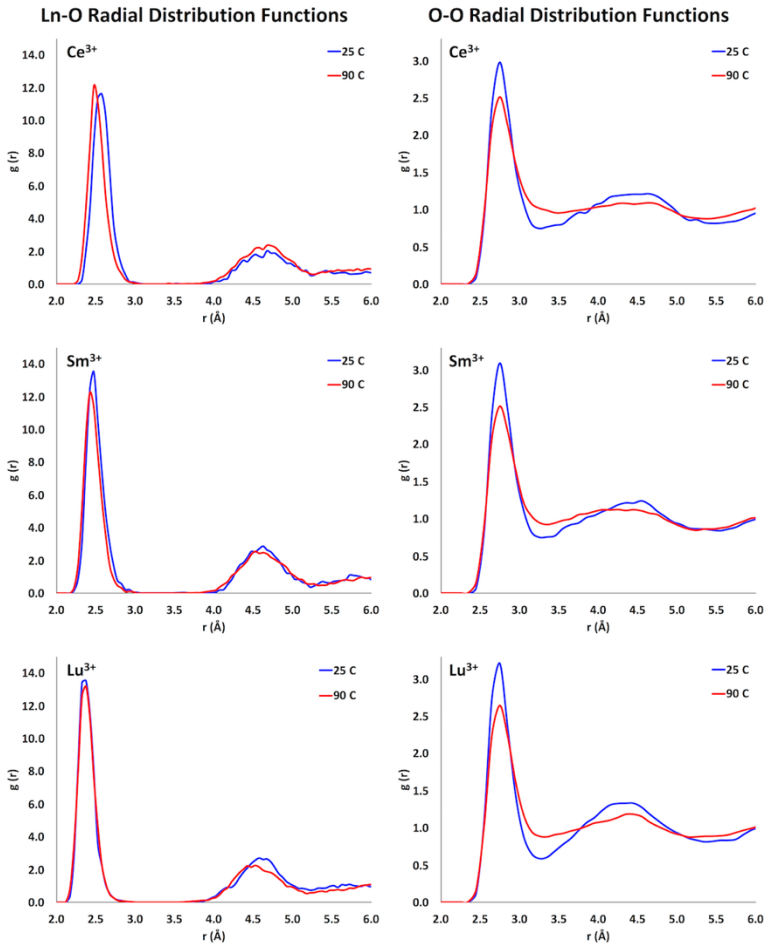

Figure 4-1: Plots of Ln-O (left hand column) and O-O radial distribution functions (right hand column) of the Ce^{3+} aqua ion (top row), Sm^{3+} aqua ion (middle row), and Lu^{3+} aqua ion (bottom row) AIMD simulations, each case at 25 °C (blue) and 90 °C (red).

Figures 4-2 and **4-3** display the EXAFS $\chi(k)$, and the Fourier-transformed $\chi(R)$ spectra generated from AIMD simulations. The $\chi(k)$ from the AIMD (**Figure 4-2**) show that increasing the temperature from 25 °C to 90 °C has a modest effect on the predicted spectra. The Ce $\chi(k)$ spectra in **Figure 4-2**, and to a lesser extent the Sm spectra, show appreciable phase shifts in the oscillations consistent with a contraction in the Ln-O bond distance at higher temperature. It is important to note that the simulated spectra for Lu^{3+} at 25 °C and 90 °C are both from eight-coordinate first-sphere structures, while those for

Ce^{3+} and Sm^{3+} represent an eight-coordinate structure at 90 °C and a nine-coordinate structure at 25°C. Thus, to a large extent the change coordination number in first sphere symmetry explains the observed differences in the AIMD EXAFS spectra of the Ce^{3+} and Sm^{3+} ions at the two different temperatures. The AIMD-predicted Lu^{3+} ion EXAFS spectra show a small but systematic shift to lower *k*-values at 90 °C, which corresponds to a slightly increased average distance of the first coordination shell, as shown in the first peak of the Lu-O RDF (**Figure 4-1**, LHS bottom row).

The $\chi(R)$ spectra in **Figure 4-3** provide further insights into trends within the lanthanide series with regards to increases in temperature. The AIMD spectra for Ce^{3+} and Sm^{3+} (LHS) show a contraction of the distance and a reduction in the amplitude of the $\chi(R)$ that is consistent with the difference in the nine- (25 °C) versus the eight-coordinate (90 °C) ions. The near-identical first peak of the Lu-O RDFs at 25 °C and 90 °C (**Figure 4-1**, bottom row) corresponds with the near-identical EXAFS spectra for Lu^{3+} at 25 °C and 90 °C, for the predicted spectra (**Figures 4-2** and **4-3**, bottom row).

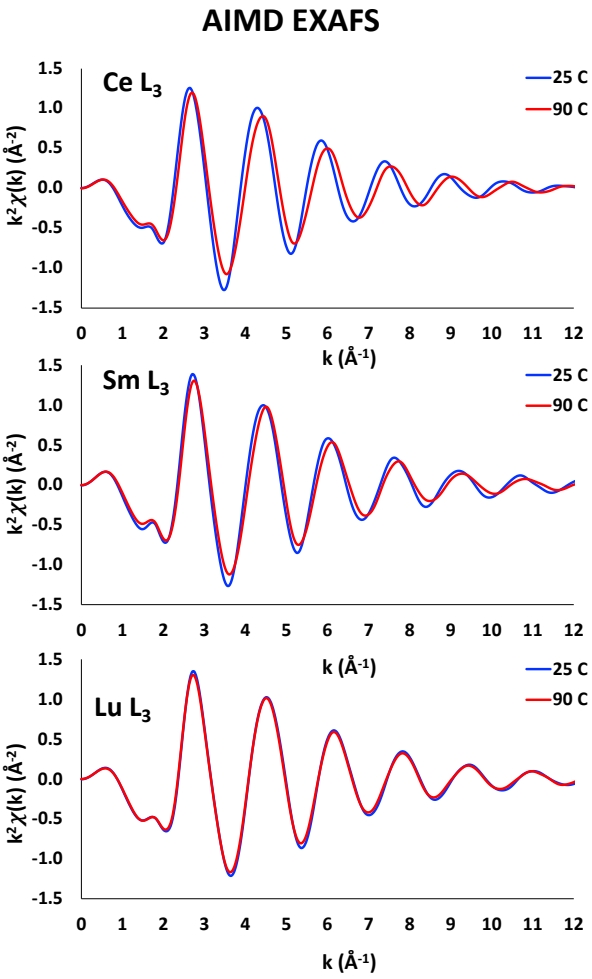

Figure 4-2: k^2-weighted $\chi(k)$ spectra of the Ce^{3+} (top row), Sm^{3+} (middle row), and Lu^{3+} (bottom row) L_3-edges predicted with simulation (left hand column), each case at 25 °C (blue) and 90 °C (red).

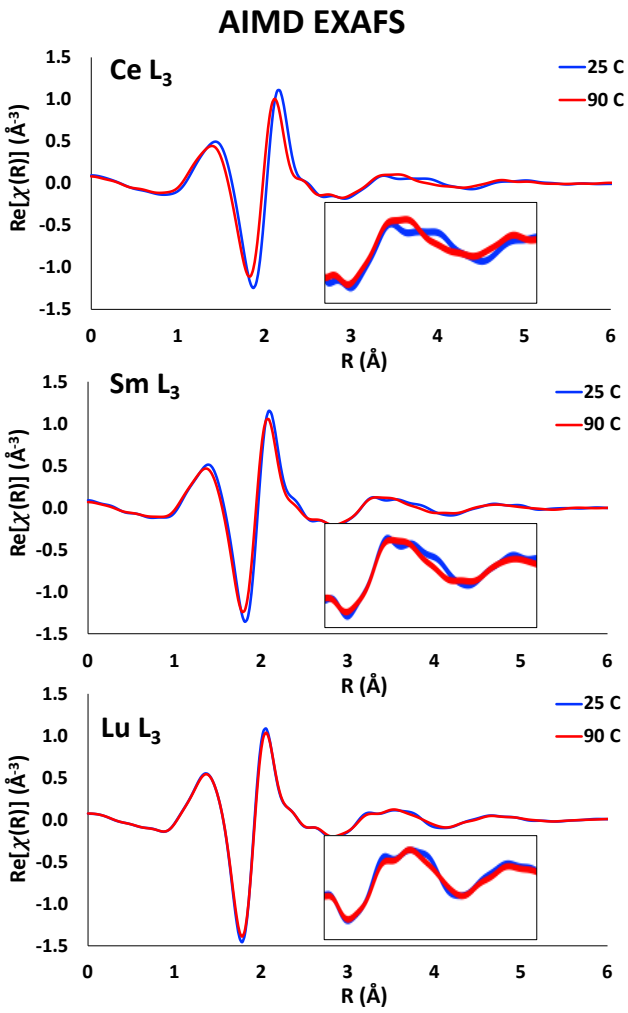

Figure 4-3: *Re*[$\chi(R)$] spectra derived from k^2-weighting of the Ce^{3+} (top row), Sm^{3+} (middle row), and Lu^{3+} (bottom row) L_3-edges predicted with simulation (left hand column), each case at 25 °C (blue) and 90 °C (red). The inserts of the figures show the expanded regions between 2.8 to 5 $Å^{-1}$ where the multiple scattering contributions, that are enhanced by certain symmetries, become more important.

4.4 Discussion

A change in the coordination number of the first sphere, or symmetry of the first sphere within a coordination number, would be detected in EXAFS as modest changes in average Ln-O distances or Debye-Waller factors. However, the multiple scattering region, from ~2.5 < R < ~6 Å, shown in the **Figure 4-3** inserts, provides a much more

sensitive fingerprint of the coordination symmetry.[12] For the AIMD (**Figure 4-3**), the structure of the multiple scattering regions at 25 °C and 90 °C are significantly different for Ce^{3+}, and Sm^{3+} ions, and to a less but still significant extent for the Lu^{3+} ion.

The Ln^{3+} ions were treated as having a single coordination number. A limitation of AIMD simulations is that nanosecond or greater timescales are not attainable, and therefore we cannot simulate water exchange events or back-and-forth changes in coordination number,[58] which results in that the AIMD simulations includes only equilibrium sampling of single coordination number conformations. Longer time scales would result in non-integer average coordination numbers that are a more complete sample of what is observed in experiment.[36] Since temperature is likely to reduce the difference in population between 9- and 8-coordinate species (these were estimated with electronic structure calculations for the Ce^{3+} aqua ion to change from ~31:1 CN=9:CN=8 species at 25 °C to ~13:1 CN=9:CN=8 species at 90 °C), longer simulation times that sample both coordination numbers could be used to accurately determine the free energy difference and relative populations of both coordination numbers at 25 and 90 °C. Longer AIMD simulations, with water exchange events, will likely result in EXAFS spectra whose differences between 25 °C and 90 °C more accurately model coordination.

Although AIMD simulations cannot sample water exchange events, they can identify the preferred coordination number of lanthanide aqua ions.[12] The Ce^{3+} and Sm^{3+} ions began as 9-coordinate in the AIMD simulations at 90 °C (starting point was the equilibrated 25 °C structures), however, they readily became 8-coordinate in the AIMD time scale at 90 °C, therefore the equilibrium simulation of the Ce^{3+} and Sm^{3+} aqua ions only samples 8-coordinate conformations.

The O-Ln-O angle distribution functions (**Figure 4-4**) from AIMD simulations, which correspond to the first peak of the Ln-O RDFs, show similar findings. For the Ce^{3+} and Sm^{3+} ions, the ADFs between 25 °C and 90 °C vary, due to the change in coordination number. For the Lu^{3+} ion, the ADFs at 25 °C and 90 °C are quite similar. A small difference is observed: the broadening of a minor peak around ~115° - 120° at the higher temperature. This is explained by the fact that, at room temperature, the Lu^{3+} aqua ion, although highly disordered and dynamical,[12] prefers the square antiprismatic geometry.[12,29] However, at 90 °C the dodecahedral geometry becomes preferred over the square antiprism. This is shown in the bottom frame of **Figure 4-4**, which superimposes the Lu^{3+} ion's ADFs with the angle distributions of ideal square antiprism and dodecahedral geometries. Also, the RMSD of the first coordination sphere of the Lu^{3+} aqua ion to the square antiprism slightly increased from 0.39+/-0.03 Å to 0.43+/-0.04 Å between 25 °C and 90 °C; it slightly decreased to the dodecahedral geometry from 0.44+/-0.02 Å to 0.41+/-0.05 Å.

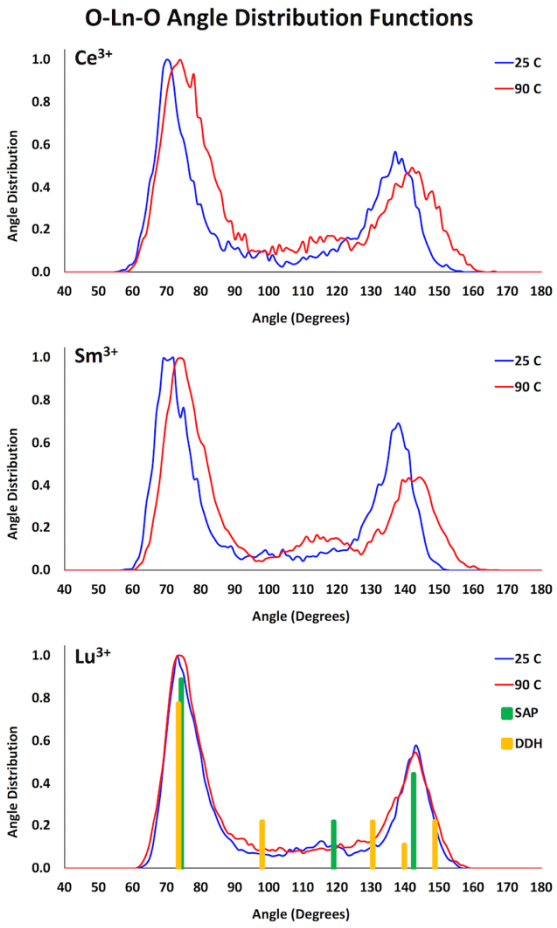

Figure 4-4: Plots of O-Ln-O angle distribution functions of the Ce^{3+} aqua ion (top row), Sm^{3+} aqua ion (middle row), and Lu^{3+} aqua ion (bottom row) AIMD simulations, each case at 25 °C (blue) and 90 °C (red), normalized for comparison. The angle distribution of the square antiprism (SAP, green) and dodecahedral (DDH, yellow) ideal geometries are superimposed for visual comparison.

There is distinction to be made regarding the definition of disorder for water molecules in the first coordination sphere of cations. The Debye-Waller factor (σ^2) for the Ln-O interaction in EXAFS measures only the radial component of the thermal ellipsoid of the oxygen atom with respect to the Ln position. The simulated Debye Waller factors for Ln^{3+} ions (~0.007 $Å^2$) are approximately the same as for first-row transition metals.[12,59] First-row transition elements, in the III oxidation state, are considered to have well-ordered first spheres water molecules with octahedral symmetry. In the case of the

Ln^{3+} ions, however there may be larger disorder in the symmetry within the water hydration sphere due to water packing efficiency: an excess of ion-surface area can accommodate multiple symmetries with a higher degree of disorder than suggested by a relatively small Debye-Waller factor. At 25 °C, the lanthanide contraction reaches a point around the middle of the series where the packing limitation favors a change in coordination number from 9 to 8. The AIMD simulations in this work suggest that at 90 °C this change occurs in the early lanthanides; therefore, the later lanthanides remain 8-coordinate 90 °C, with water molecules in the first sphere that show similar disorder at 25 °C and 90 °C.

4.5. Conclusions

AIMD results suggest that the first coordination sphere of the lanthanide aqua ions remain similarly disordered as temperature increases, more so for the Lu^{3+} ion that remains eight-coordinate, than for the Ce^{3+} and Sm^{3+} ions that change their preferred coordination number from nine to eight. AIMD simulations point to a structure of first coordination sphere of the Lu^{3+} ion that almost does not vary between 25 °C and 90 °C. Lanthanide – water coordination bonds have a highly ionic character that allow disorder in the geometry of the first coordination sphere at room temperature, yet are strong enough that temperature does not increase their disorder significantly, aside from changing the preferred coordination number from nine to eight for the lighter- to middle-lanthanides. As the lanthanide aqua ions are contracted along the series due to *f* electrons there is less temperature-induced disorder of the first coordination sphere.

Chapter 4 References

(1) Smith, R. M.; Martell, A. E. *Critical Stability Constants: Inorganic Complexes*; Springer, 1976; Vol. 4.

(2) Monteiro, J. H. S. K.; Sigoli, F. A.; de Bettencourt-Dias, A. A Water-Soluble TbIII Complex as a Temperature-Sensitive Luminescent Probe. *Can. J. Chem.* **2018**, *96*, 859–864.

(3) Liu, S.; Featherston, E. R.; Cotruvo, J. A.; Baiz, C. R. Lanthanide-Dependent Coordination Interactions in Lanmodulin: A 2D IR and Molecular Dynamics Simulations Study. *Phys. Chem. Chem. Phys.* **2021**, *23*, 21690–21700.

(4) Qiao, Y.; Schelter, E. J. Lanthanide Photocatalysis. *Acc. Chem. Res.* **2018**, *51*, 2926–2936.

(5) Nilsson, M.; Nash, K. L. Trans-Lanthanide Extraction Studies in the TALSPEAK System: Investigating the Effect of Acidity and Temperature. *Solvent Extr. Ion Exch.* **2009**, *27*, 354–377.

(6) Jordan, N.; Demnitz, M.; Lösch, H.; Starke, S.; Brendler, V.; Huittinen, N. Complexation of Trivalent Lanthanides (Eu) and Actinides (Cm) with Aqueous Phosphates at Elevated Temperatures. *Inorg. Chem.* **2018**, *57*, 7015–7024.

(7) Jaque, D.; Vetrone, F. Luminescence Nanothermometry. *Nanoscale* **2012**, *4*, 4301–4326.

(8) Wang, X.; Wolfbeis, O. S.; Meier, R. J. Luminescent Probes and Sensors for Temperature. *Chem. Soc. Rev.* **2013**, *42*, 7834–7869.

(9) Clark, A. E. Density Functional and Basis Set Dependence of Hydrated Ln(III) Properties. *J. Chem. Theory Comput.* **2008**, *4*, 708–718.

(10) Zhang, J.; Heinz, N.; Dolg, M. Understanding Lanthanoid(III) Hydration Structure and Kinetics by Insights from Energies and Wave Functions. *Inorg. Chem.* **2014**, *53*, 7700–7708.

(11) Zhang, J.; Dolg, M. Labile Capping Bonds in Lanthanide(III) Complexes: Shorter and Weaker. *J. Phys. Chem. A* **2015**, *119*, 774–780.

(12) Shiery, R. C.; Fulton, J. L.; Balasubramanian, M.; Nguyen, M.-T.; Lu, J.-B.; Li, J.; Rousseau, R.; Glezakou, V.-A.; Cantu, D. C. Coordination Sphere of Lanthanide Aqua Ions Resolved with Ab Initio Molecular Dynamics and X-Ray Absorption Spectroscopy. *Inorg. Chem.* **2021**, *60*, 3117–3130.

(13) Finney, A. R.; Lectez, S.; Freeman, C. L.; Harding, J. H.; Stackhouse, S. Ion Association in Lanthanide Chloride Solutions. *Chem. -Eur. J* **2019**, *25*, 8725–8740.

(14) Yazyev, O. V; Helm, L. Gadolinium (III) Ion in Liquid Water: Structure, Dynamics, and Magnetic Interactions from First Principles. *J. Chem. Phys.* **2007**, *127*, 84506.

(15) Ikeda, T.; Hirata, M.; Kimura, T. Hydration Structure of Y3+ and La3+ Compared: An Application of Metadynamics. *J. Chem. Phys.* **2005**, *122*, 244507.

(16) Kowall, T. H.; Foglia, F.; Helm, L.; Merbach, A. E. Molecular Dynamics Simulation Study of Lanthanide Ions Ln3+in Aqueous Solution Including Water Polarization. Change in Coordination Number from 9 to 8 along the Series. *J. Am. Chem. Soc.* **1995**, *117*, 3790–3799.

(17) Kowall, T.; Foglia, F.; Helm, L.; Merbach, A. E. Mechanisms of Water Exchange between Lanthanide(II) Aqua Ions [Ln(H 2O)n]3+ and Bulk Water: A Molecular Dynamics Simulation Approach Including High-Pressure Effects. *Chem. - A Eur. J.* **1996**, *2*, 285–294.
(18) Floris, F. M.; Tani, A. A Study of Aqueous Solutions of Lanthanide Ions by Molecular Dynamics Simulation with Ab Initio Effective Pair Potentials. *J. Chem. Phys.* **2001**, *115*, 4750–4765.
(19) Clavaguéra, C.; Pollet, R.; Soudan, J. M.; Brenner, V.; Dognon, J. P. Molecular Dynamics Study of the Hydration of Lanthanum(III) and Europium(III) Including Many-Body Effects. *J. Phys. Chem. B* **2005**, *109*, 7614–7616.
(20) Duvail, M.; Spezia, R.; Vitorge, P. A Dynamic Model to Explain Hydration Behaviour along the Lanthanide Series. *ChemPhysChem* **2008**, *9*, 693–696.
(21) Duvail, M.; Vitorge, P.; Spezia, R. Building a Polarizable Pair Interaction Potential for Lanthanoids(III) in Liquid Water: A Molecular Dynamics Study of Structure and Dynamics of the Whole Series. *J. Chem. Phys.* **2009**, *130*.
(22) Duvail, M.; D'Angelo, P.; Gaigeot, M. P.; Vitorge, P.; Spezia, R. What First Principles Molecular Dynamics Can Tell Us about EXAFS Spectroscopy of Radioactive Heavy Metal Cations in Water. *Radiochim. Acta* **2009**, *97*, 339–346.
(23) Duvail, M.; Ruas, A.; Venault, L.; Moisy, P.; Guilbaud, P. Molecular Dynamics Studies of Concentrated Binary Aqueous Solutions of Lanthanide Salts: Structures and Exchange Dynamics. *Inorg. Chem* **2010**, *49*, 519–530.
(24) Marjolin, A.; Gourlaouen, C.; Clavaguera, C.; Ren, P. Y. Y.; Piquemal, J. P.; Dognon, J. P. Hydration Gibbs Free Energies of Open and Closed Shell Trivalent Lanthanide and Actinide Cations from Polarizable Molecular Dynamics. *J. Mol. Model* **2014**, *20*, 7.
(25) Li, P.; Song, L. F.; Merz, K. M. Parameterization of Highly Charged Metal Ions Using the 12-6-4 LJ-Type Nonbonded Model in Explicit Water. *J. Phys. Chem. B* **2015**, *119*, 883–895.
(26) Sessa, F.; Spezia, R.; D'Angelo, P. Lutetium(Iii) Aqua Ion: On the Dynamical Structure of the Heaviest Lanthanoid Hydration Complex. *J. Chem. Phys.* **2016**, *144*, 204505.
(27) Morales, N.; Galbis, E.; Martínez, J. M.; Pappalardo, R. R.; Sánchez Marcos, E. Identifying Coordination Geometries of Metal Aquaions in Water: Application to the Case of Lanthanoid and Actinoid Hydrates. *J. Phys. Chem. Lett.* **2016**, *7*, 4275–4280.
(28) Migliorati, V.; Serva, A.; Terenzio, F. M.; D'Angelo, P. Development of Lennard-Jones and Buckingham Potentials for Lanthanoid Ions in Water. *Inorg. Chem.* **2017**, *56*, 6214–6224.
(29) Qiao, B.; Skanthakumar, S.; Soderholm, L. Comparative CHARMM and AMOEBA Simulations of Lanthanide Hydration Energetics and Experimental Aqueous-Solution Structures. *J. Chem. Theory Comput.* **2018**, *14*, 1781–1790.
(30) Sessa, F.; D'Angelo, P.; Migliorati, V. Combined Distribution Functions: A Powerful Tool to Identify Cation Coordination Geometries in Liquid Systems. *Chem. Phys. Lett.* **2018**, *691*, 437–443.
(31) Habenschuss, A.; Spedding, F. H. The Coordination (Hydration) of Rare Earth

Ions in Aqueous Chloride Solutions from x-Ray Diffraction. II. LaCI3, PrCI3, and NdCI3. *J. Chem. Phys.* **1979**, *70*, 3758–3763.

(32) Habenschuss, A.; Spedding, F. H. The Coordination (Hydration) of Rare Earth Ions in Aqueous Chloride Solutions from x-Ray Diffraction. I. TbCI3, DyCI3, ErCI3, TmCI3, and LuCI3. *J. Chem. Phys.* **1979**, *70*, 2797–2806.

(33) Habenschuss, A.; Spedding, F. H. The Coordination (Hydration) of Rare Earth Ions in Aqueous Chloride Solutions from x-Ray Diffraction. III. SmCl3, EuCl3, and Series Behavior. *J. Chem. Phys.* **1980**, *73*, 442–450.

(34) Yamaguchi, T.; Nomura, M.; Wakita, H.; Ohtaki, H. An Extended X-Ray Absorption Fine Structure Study of Aqueous Rare Earth Perchlorate Solutions in Liquid and Glassy States. *J. Chem. Phys.* **1988**, *89*, 5153–5159.

(35) Allen, P. G.; Bucher, J. J.; Shuh, D. K.; Edelstein, N. M.; Craig, I. Coordination Chemistry of Trivalent Lanthanide and Actinide Ions in Dilute and Concentrated Chloride Solutions. *Inorg. Chem.* **2000**, *39*, 595–601.

(36) Persson, I.; D'Angelo, P.; De Panfilis, S.; Sandström, M.; Eriksson, L. Hydration of Lanthanoid(III) Ions in Aqueous Solution and Crystalline Hydrates Studied by EXAFS Spectroscopy and Crystallography: The Myth of the "Gadolinium Break." *Chem. - A Eur. J.* **2008**, *14*, 3056–3066.

(37) D'Angelo, P.; Zitolo, A.; Migliorati, V.; Chillemi, G.; Duvail, M.; Vitorge, P.; Abadie, S.; Spezia, R. Revised Ionic Radii of Lanthanoid(III) Ions in Aqueous Solution. *Inorg. Chem.* **2011**, *50*, 4572–4579.

(38) Näslund, J.; Lindqvist-Reis, P.; Persson, I.; Sandström, M. Steric Effects Control the Structure of the Solvated Lanthanum(III) Ion in Aqueous, Dimethyl Sulfoxide, and N,N'-Dimethylpropyleneurea Solution. An EXAFS and Large-Angle X-Ray Scattering Study. *Inorg. Chem.* **2000**, *39*, 4006–4011.

(39) Kofod, N.; Nawrocki, P.; Platas-Iglesias, C.; Sørensen, T. J. Electronic Structure of Ytterbium(III) Solvates—a Combined Spectroscopic and Theoretical Study. *Inorg. Chem.* **2021**, *60*, 7453–7464.

(40) Miyanaga, T.; Fujikawa, T. Quantum Statistical Approach to Debye-Waller Factor in EXAFS, EELS and ARXPS. II. Application to One-Dimensional Models. *J. Phys. Soc. Japan* **1994**, *63*, 1036–1052.

(41) Sawa, Y.; Miyanaga, T.; Tanida, H.; Watanabe, I. Temperature Dependence of EXAFS for Bromide Ions in Solution. *J. Chem. Soc. Faraday Trans.* **1995**, *91*, 4389–4393.

(42) Hoffmann, M. M.; Darab, J. G.; Palmer, B. J.; Fulton, J. L. A Transition in the Ni2+ Complex Structure from Six- to Four-Coordinate upon Formation of Ion Pair Species in Supercritical Water: An X-Ray Absorption Fine Structure, Near-Infrared, and Molecular Dynamics Study. *J. Phys. Chem. A* **1999**, *103*, 8471–8482.

(43) Fulton, J. L.; Hoffmann, M. M.; Darab, J. G. An X-Ray Absorption Fine Structure Study of Copper(I) Chloride Coordination Structure in Water up to 325°C. *Chem. Phys. Lett.* **2000**, *330*, 300–308.

(44) Simonet, V.; Calzavara, Y.; Hazemann, J. L.; Argoud, R.; Geaymond, O.; Raoux, D. Structure of Aqueous ZnBr2 Solution Probed by X-Ray Absorption Spectroscopy in Normal and Hydrothermal Conditions. *J. Chem. Phys.* **2002**, *116*, 2997–3006.

(45) Perdew, J. P.; Burke, K.; Ernzerhof, M. Generalized Gradient Approximation Made Simple. *Phys. Rev. Lett.* **1996**, *77*, 3865–3868.
(46) Hutter, J.; Iannuzzi, M.; Schiffmann, F.; Vandevondele, J. Cp2k: Atomistic Simulations of Condensed Matter Systems. *Wiley Interdiscip. Rev. Comput. Mol. Sci.* **2014**, *4*, 15–25.
(47) VandeVondele, J.; Krack, M.; Mohamed, F.; Parrinello, M.; Chassaing, T.; Hutter, J. Quickstep: Fast and Accurate Density Functional Calculations Using a Mixed Gaussian and Plane Waves Approach. *Comput. Phys. Commun.* **2005**, *167*, 103–128.
(48) Goedecker, S.; Teter, M.; Hutter, J. Separable Dual-Space Gaussian Pseudopotentials. *Phys. Rev. B - Condens. Matter Mater. Phys* **1996**, No. 54, 1703–1710.
(49) VandeVondele, J.; Hutter, J. Gaussian Basis Sets for Accurate Calculations on Molecular Systems in Gas and Condensed Phases. *J. Chem. Phys.* **2007**, *127*.
(50) Lu, J. B.; Cantu, D. C.; Nguyen, M. T.; Li, J.; Glezakou, V. A.; Rousseau, R. Norm-Conserving Pseudopotentials and Basis Sets to Explore Lanthanide Chemistry in Complex Environments. *J. Chem. Theory Comput.* **2019**, *15*, 5987–5997.
(51) Lippert, G.; Hutter, J.; Parrinello, M. A Hybrid Gaussian and Plane Wave Density Functional Scheme. *Mol. Phys.* **1997**, *92*, 477–488.
(52) Grimme, S.; Antony, J.; Ehrlich, S.; Krieg, H. A Consistent and Accurate Ab Initio Parametrization of Density Functional Dispersion Correction (DFT-D) for the 94 Elements H-Pu. *J. Chem. Phys.* **2010**, *132*.
(53) Schenter, G. .; Fulton, J. L. XAFS Techniques for Catalysts, Nanomaterials and Surfaces; Iwasawa, I., Asakura, K., Tada, M., Eds.; Springer, 2017; pp 251–270.
(54) Ferrier, M. G.; Stein, B. W.; Batista, E. R.; Berg, J. M.; Birnbaum, E. R.; Engle, J. W.; John, K. D.; Kozimor, S. A.; Lezama Pacheco, J. S.; Redman, L. N. Synthesis and Characterization of the Actinium Aquo Ion. *ACS Cent. Sci.* **2017**, *3*, 176–185.
(55) Palmer, B. J.; Pfund, D. M.; Fulton, J. L. Direct Modeling of EXAFS Spectra from Molecular Dynamics Simulations. *J. Phys* **1996**, *100*, 13393–13398.
(56) Rehr, J. J.; Kas, J. J.; Prange, M. P.; Sorini, A. P.; Takimoto, Y.; Vila, F. Ab Initio Theory and Calculations of X-Ray Spectra. *C. R. Phys* **2009**, *10*, 548–559.
(57) Rousseau, R.; Schenter, G. K.; Fulton, J. L.; Linehan, J. C.; Engelhard, M. H.; Autrey, T. Defining Active Catalyst Structure and Reaction Pathways from Ab Initio Molecular Dynamics and Operando XAFS: Dehydrogenation of Dimethylaminoborane by Rhodium Clusters. *J. Am. Chem. Soc.* **2009**, *131*, 10516–10524.
(58) Helm, L.; Merbach, A. E. Water Exchange on Metal Ions: Experiments and Simulations. *Coord. Chem. Rev.* **1999**, *187*, 151–181.
(59) Fulton, J. L.; Bylaska, E. J.; Bogatko, S.; Balasubramanian, M.; Cauët, E.; Schenter, G. K.; Weare, J. H. Near-Quantitative Agreement of Model-Free DFT-MD Predictions with XAFS Observations of the Hydration Structure of Highly Charged Transition-Metal Ions. *J. Phys. Chem. Lett.* **2012**, *3*, 2588–2593.

Supporting Information for Chapter 4

Table 4-S1. Ln^{III} electronic configuration and multiplicities

Ln^{III}	Electronic configuration	Multiplicity
La	$5s^25p^6$	1
Ce	$4f^1$	2
Pr	$4f^2$	3
Nd	$4f^3$	4
Pm	$4f^4$	5
Sm	$4f^5$	6
Eu	$4f^6$	7
Gd	$4f^7$	8
Tb	$4f^8$	7
Dy	$4f^9$	6
Ho	$4f^{10}$	5
Er	$4f^{11}$	4
Tm	$4f^{12}$	3
Yb	$4f^{13}$	2
Lu	$4f^{14}$	1

CHAPTER 5

Computational prediction of all lanthanide aqua ion acidity constants

Richard C. Shiery, Kyle A. Cooper, David C. Cantu

Department of Chemical and Materials Engineering, University of Nevada, Reno

Modified from a manuscript that was published in *Inorganic Chemistry, 60, 10257 – 10266*, with the same title and authors

5.1. Introduction

The protonation state of lanthanide-containing species affects their molecular structure and changes their reactivity. Any heteroatom-hydrogen group in lanthanide (Ln) compounds can gain/lose the proton, with consequences in their properties. Some examples illustrate the importance:

(i) Ln^{III} aqua ions undergo hydrolysis and form $Ln^{III}(OH)$ species, which react with each other forming complexes with multiple Ln atoms linked by OH groups or O atoms, and precipitate.[1] This affects Ln separations, as the solution pH, and each Ln^{III} aqua ion's pK_a values, will determine their speciation and whether they precipitate or remain in solution.

(ii) A single change in the protonation state of ethylenediaminetetraacetic acid in Ln-EDTA complexes, (e.g., $[La^{III}\text{-}EDTA^{4-}]^{-}$ and $[La^{III}\text{-}EDTA^{3-}]^{0}$) changes the stability of the complex by one order of magnitude.[2] This illustrates that the stability of Ln-ligand complexes with multi-acidic ligands is very sensitive to protonation state. Metal-chelating ligands are known to have pH-sensitive binding, for example siderophores,[3] and pH has been used to control Ln biosorption.[4]

(iii) Contrast agents for magnetic resonance imaging include gadolinium-ligand complexes, for example Gd-DTPA, which must have at least one coordinated water molecule.[5,6] If a coordinated water molecule undergoes hydrolysis and becomes a hydroxyl, the Gd-ligand complex could lose its functionality, and its complex stability will change, which has consequences as uncomplexed Gd^{III} ions are involved in causing nephrogenic systemic fibrosis.[7]

(iv) Lanthanum exchanged faujasite is the principal component in catalysts used for petroleum cracking.[8] Brønsted acidic sites, on faujasite itself, and from H_2O or OH species coordinated to La atoms,[9] play a catalytic role to degrade hydrocarbons,[10] and possibly also on the hydrothermal stability of La-exchanged faujasite during steam treatment in cracking.

(v) Changes in protonation state will affect hydrogen bonding in rare earth metal organic frameworks,[11] which determines the optical and electronic properties of the porous material.

(vi) The role of Ln^{III} ions in enzyme active sites will depend on the Ln coordination structure with amino acid residues,[12–16] which are susceptible to protonation state changes, therefore affecting the whole coordination structure in the enzymes' active site.

It is difficult to identify the protonation state of specific acid sites in compounds or materials with multiple Brønsted acidic sites. Experimentally, titrations yield observable, ensemble quantities that do not connect particular acid sites, i.e., it is challenging to assign which particular acidic site corresponds to each measured pK_a value. Additionally, competing protonation among acidic sites cannot be deconvoluted to determine the acidity of a specific acidic group. In the case of porous materials such as zeolites or metal organic frameworks, the number of protonation sites can vary due to defects or impurities in the material structure. Further, the chemical environment affects protonation state, as is well known in protein structure where neighboring amino acid residues change local pK_a values.[17–19] Therefore, the pK_a values of a Ln-containing compound could change in mixtures, for example in Ln/actinide mixtures seen in the

nuclear fuel cycle.[20] Computationally, determining the protonation state of a Brønsted acidic site requires considering the electronic structure (forming/breaking heteroatom-H bonds) to compute a thermodynamic quantity. In the case of Ln-containing compounds, electronic structure calculations are complicated by the fact that lanthanides have a large number of nearly degenerate electronic states with high electronic spin multiplicity.

We optimized transferable GTH-type[21] pseudopotentials and their corresponding basis sets for lanthanides (LnPP1), for generalized gradient approximation calculations in a mixed Gaussian and plane wave setting.[22] These allow performing density functional theory (DFT) calculations and DFT-level *ab initio* molecular dynamics (AIMD) simulations in periodic conditions with explicit solvent molecules, well suited for Ln-containing systems in the condensed phase, e.g., porous materials, Ln-ligand complexes in solution. Other effective core potentials and basis sets are available for the lanthanides,[23–29] which are suitable for electronic structure calculations, at higher levels of theory, with systems containing up to ~100 atoms.

We recently showed that our LnPP1 pseudopotentials and basis sets with AIMD simulations can replicate the coordination structure of Ln^{III} aqua ions and Ln-ligand complexes in solution.[30,31] In this work, we employ a rare event simulation technique paired with solution phase AIMD simulations with explicit solvent, to predict a thermodynamic quantity: the first hydrolysis constant of all Ln^{III} aqua ions. The second and third hydrolysis constants were also quantified, with respect to the first, using electronic structure calculations at a higher level of theory and including relativistic effects. The hydrolysis constants of the Ln^{III} aqua ions are the best characterized Ln complexes with multiple Brønsted acid sites. In this work, they were chosen as an ideal

experimental reference point, representative of the entire Ln series with many measurements for most Ln elements (except Pm due to radioactivity), to determine an approach to quantify absolute pK_a values of multi-acidic Ln-containing systems solely from computation.

5.2. Methods

5.2.1. Approach

Water molecules coordinated on Ln^{III} ions in aqueous solution undergo three hydrolysis reactions:

$$\mathrm{p}K_{a1}\colon X^{3-} + [\mathrm{Ln^{III}} \cdot (\mathrm{H_2O})_n + \mathrm{H_2O}]^{3+} \leftrightarrow X^{3-} + [\mathrm{Ln^{III}(OH)} \cdot (\mathrm{H_2O})_{n-1} + \mathrm{H_3O^+}]^{3+}$$

$$\mathrm{p}K_{a2}\colon X^{2-} + [\mathrm{Ln^{III}(OH)} \cdot (\mathrm{H_2O})_{n-1} + \mathrm{H_2O}]^{2+} \leftrightarrow X^{2-} + [\mathrm{Ln^{III}(OH)_2} \cdot (\mathrm{H_2O})_{n-2} + \mathrm{H_3O^+}]^{2+}$$

$$\mathrm{p}K_{a3}\colon X^{-} + [\mathrm{Ln^{III}(OH)_2} \cdot (\mathrm{H_2O})_{n-2} + \mathrm{H_2O}]^{+} \leftrightarrow X^{-} + [\mathrm{Ln^{III}(OH)_3} \cdot (\mathrm{H_2O})_{n-3} + \mathrm{H_3O^+}]^{+}$$

where n is the Ln^{III} coordination number, and X is the charge neutralizing anion. La – Sm were treated nine coordinate, and Eu – Lu eight coordinate, as in our previous work.[30] Reaction free energies ΔG can be converted to pK_a units:

$$\mathrm{p}K_\mathrm{a} = \frac{-\Delta G}{RT\ln(10)} \quad (5.1)$$

at a given temperature T. All simulations and calculations in this work were done at room temperature (298 K).

Absolute values of the first hydrolysis reaction constant ($\mathrm{p}K_{\mathrm{a1}}$) were calculated from constrained, Bluemoon *ab initio* molecular dynamics simulations,[32,33] which gave potentials of mean force of the first hydrolysis reaction, i.e., the proton transfer from a

Ln^{III}-coordinated water molecule to a solution water molecule. Then, free energies were extracted from the potentials of mean force, and pK_{a1} values calculated with **equation 5.1**.

Separately, electronic structure calculations were employed to calculate free energies of the hydrolysis reactions as:

$$\Delta G_1 = G_{\mathrm{Ln^{III}(OH)\cdot(H_2O)}_{n-1}} + G_{\mathrm{H_3O^+}} - G_{\mathrm{Ln^{III}\cdot(H_2O)}_n} - G_{\mathrm{H_2O}} \quad (5.2)$$

$$\Delta G_2 = G_{\mathrm{Ln^{III}(OH)_2\cdot(H_2O)}_{n-2}} + G_{\mathrm{H_3O^+}} - G_{\mathrm{Ln^{III}(OH)\cdot(H_2O)}_{n-1}} - G_{\mathrm{H_2O}} \quad (5.3)$$

$$\Delta G_3 = G_{\mathrm{Ln^{III}(OH)_3\cdot(H_2O)}_{n-3}} + G_{\mathrm{H_3O^+}} - G_{\mathrm{Ln^{III}(OH)_2\cdot(H_2O)}_{n-2}} - G_{\mathrm{H_2O}} \quad (5.4)$$

Then, the relative values of the second and third hydrolysis reaction constants, $\Delta pK_{a,2-1}$ and $\Delta pK_{a,3-2}$, were calculated with relative reaction free energies:

$$\Delta\Delta G_{2-1} = |\Delta G_2 - \Delta G_1| \quad (5.5)$$

$$\Delta\Delta G_{3-2} = |\Delta G_3 - \Delta G_2| \quad (5.6)$$

$$\Delta pK_{a,2-1} = \frac{\Delta\Delta G_{2-1}}{RT\ln(10)} \quad (5.7)$$

$$\Delta pK_{a,3-2} = \frac{\Delta\Delta G_{3-2}}{RT\ln(10)} \quad (5.8)$$

Finally, the values of pK_{a2} and pK_{a3} were calculated with $\Delta pK_{a,2-1}$ and $\Delta pK_{a,3-2}$, using pK_{a1} values, obtained from constrained AIMD simulations, as the reference point:

$$pK_{a2} = pK_{a1} + \Delta pK_{a,2-1} \quad (5.9)$$

$$pK_{a3} = pK_{a2} + \Delta pK_{a,3-2} \quad (5.10)$$

5.2.2. Constrained ab initio molecular dynamics simulations for pK_{a1}

We previously simulated all Ln^{III} aqua ions with DFT-level AIMD to identify their first sphere coordination structures, which were verified with extended X-ray absorption fine structure (EXAFS) measurements.[30] We took equilibrated simulation frames from our

previous work as the starting point to build potentials of mean force of proton transfer of the first hydrolysis reaction, see **Figure 5-1**.

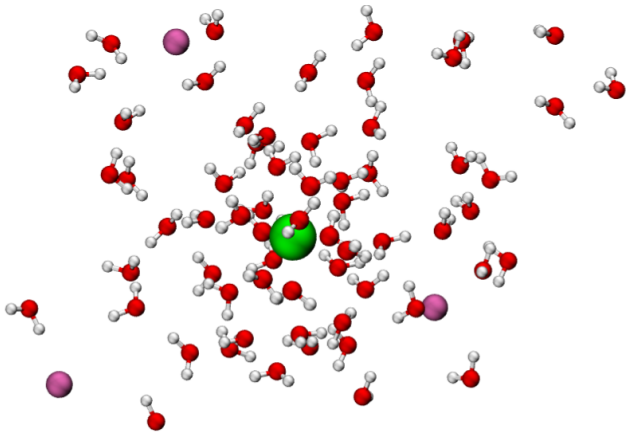

Figure 5-1: All simulations to quantify the first hydrolysis constant included a Ln^{III} ion (green), three Cl- ions (purple) to neutralize the charge, and 64 water molecules (oxygen red, hydrogen white) in periodic conditions to simulate aqueous solution.

For each Ln^{III} aqua ion in their starting frame, we pulled a proton from a coordinated water molecule to a neighboring water molecule in 0.05 Å increments, with O-H bond distances ranging from ~1.00 Å to ~1.40 Å. For each Ln^{III} ion, nine independent simulation boxes, with varying O-H distances, were generated. Each simulation box included 64 explicit water molecules in a cubic periodic box of 12.42 Å length, which corresponds to a water density of 0.998 g/mL. Three Cl^- ions were added to simulation boxes to neutralize the charge. Ln^{III} multiplicities were assigned following Hund's rule, and appear in the Supporting Information (SI). For each simulation box, the O-H distance was constrained (**Figure 5-2**), and 15 ps of NVT simulation were performed with 1 fs time steps. The forces on the constraint (SHAKE Lagragian multipliers) were averaged over the last 10 ps (5 to 15 ps) of NVT simulation, to generate an average force on the constraint for each O-H distance ($\boldsymbol{r_{O\text{-}H}}$). An integration of the forces on the constraint over $\boldsymbol{r_{O\text{-}H}}$ was done to obtain potentials of mean force (i.e., free

energy profile) of proton transfer in the first hydrolysis reaction, from which pK_{a1} values calculated using **equation 5.1**. Helmholtz free energies are obtained from the potentials of mean force, but they approximate Gibbs free energies due to a very small *PV* term from the simulation box. The potential of mean force of the first hydrolysis constant of Gd^{III} appears in **Figure 5-2**. To estimate the error in pK_{a1} values, we took the absolute difference between pK_{a1} values calculated with the first half of equilibrated trajectory (5 to 10 ps) with those calculated with second half (10 to 15 ps) of the equilibrated trajectory.

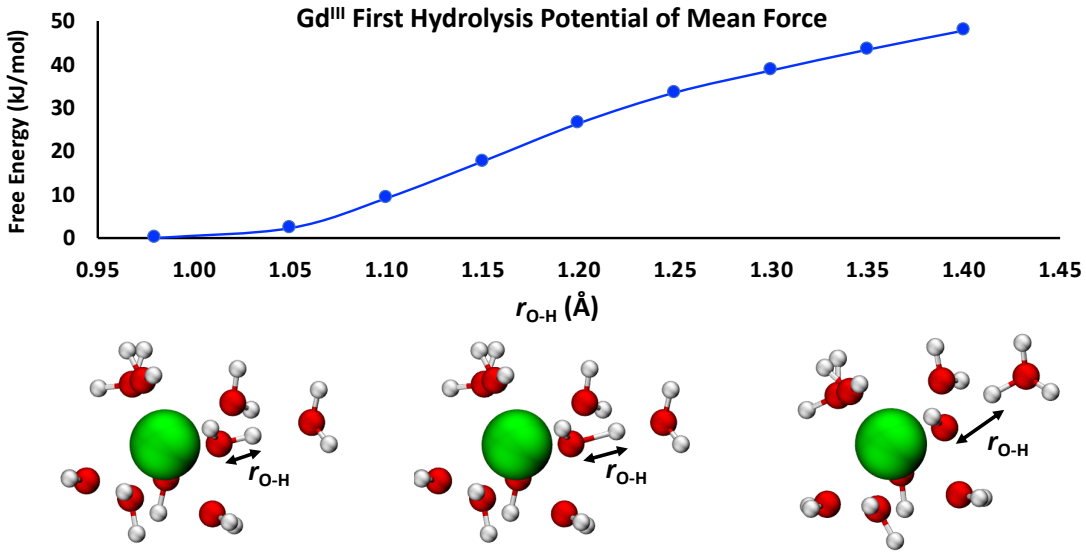

Figure 5-2: Potentials of mean force (top) of a proton transfer from $[Gd^{III}(H_2O)_8]^{3+}$ to H_2O, the first hydrolysis reaction. Similar potentials of mean force were generated for all Ln^{III} aqua ions. For each point on the graph, an AIMD simulation with a constraint on $r_{O\text{-}H}$ was performed. Each AIMD simulation was done as shown in Figure 5-1, in this figure only the Ln^{III}-coordinated water molecules, and the water molecules which accepts a proton, are shown for clarity (bottom) with same coloring scheme as in Figure 5-1.

Potentials of mean force of proton transfer from constrained DFT-based AIMD simulations have been shown to be an accurate way to calculate pK_a values.[34–36] This

approach has been employed to obtain the acidity constants of oxide surfaces,[37] organic compounds,[38–42] and transition metal complexes.[43] The recent work by Schilling and Luber is informative and discusses different constraints and methods to quantify pK_a values from AIMD simulations; they find that simple distances between heteroatoms and H atoms are an adequate constraint to calculate absolute pK_a constants in inorganic compounds.[43] Using O-H distances as the constraint in AIMD simulation for potentials of mean force of proton transfer reactions are best suited for first hydrolysis reactions: the second and third reactions have additional Ln-coordinated -OH groups that may accept a proton from the solvent, via a Grothus-type mechanism, as the proton is transferred from the Ln-coordinated H_2O molecule to a solvent H_2O molecule for the second or third hydrolysis.

All atoms in the AIMD simulation boxes were modeled with density functional theory (DFT), conducted in the PBE functional[44] using the CP2K package.[45,46] The PBE functional has been tested for water[47,48] and lanthanides.[49,50] Core electrons were modeled with norm-conserving GTH pseudopotentials,[21] valence electrons were modelled with polarizable double-zeta basis sets,[51] and our LnPP1 pseudopotentials and basis sets[22] were used for Ln^{III} ions. Long range electrostatic terms were determined with a supplementary plane wave basis set, using a 500 Ry cutoff for La – Gd, 800 Ry for Tb – Tm, and 1000 Ry for Yb – Lu. Grimme's D3 corrections[52] were used to account for van der Waals interactions within a 6.0 Å radius in all simulations. AIMD simulations, as here described, replicated Ln^{III} aqua ion molecular geometries, including Ln^{III}-O distances within ~0.05 Å of experiment, in our recent work.[30]

5.2.3 Electronic structure calculations for pK_{a2} and pK_{a3}

The free energies of the three hydrolysis reactions were calculated in a thermodynamic integration (**equations 5.2 – 5.4**). To determine the free energies of each species in **equations 5.2 – 5.4**, we used an implicit water solvent model (conductor-like polarizable continuum model).[53] Water and hydroxide molecules directly coordinated to Ln^{III} ions were explicitly included (**Figure 5-3**).

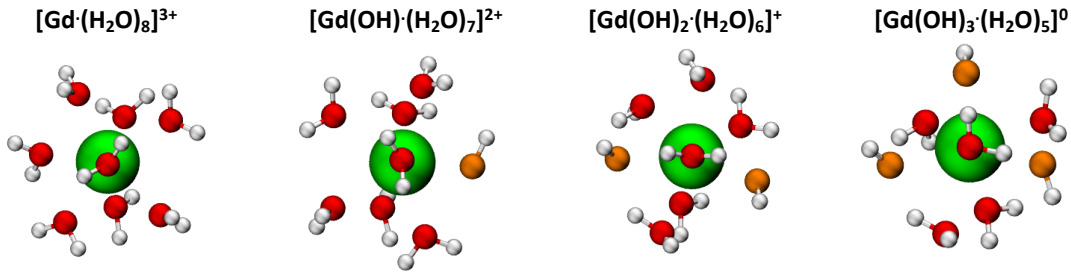

Figure 5-3: Optimized geometries of Gd^{III} (green) aqua ion hydroxides. All coordinated water molecules (oxygen red, hydrogen white) and hydroxyl groups (orange oxygen) were included in geometry optimization and energy calculations for the thermodynamic integration.

For each Ln^{III} ion, the molecular coordinates of all the species to complete the thermodynamic integration were optimized with the M06 functional[54] using effective core potentials and corresponding basis sets (Stuttgart RSC Segmented + ECP) for Ln^{III} ions,[23,55] and the cc-PVTZ basis set[56] for atoms in H_2O, OH^- and H_3O^+ species. Vibrational frequencies of the optimized structures were obtained as well to compute free energies. Multiple geometry optimizations were performed because Ln^{III} aqua ions and hydroxides have multiple minima that are close in energy. Although the identified optimized structures are not guaranteed to be global minima, they represent the minima in a large conformational space, because our starting structures came from AIMD

simulations. The SI provides additional discussion on the vibrational frequencies. With the optimized geometries, all-electron single-point energy calculations were performed using the M06 functional, a relativistic second order Douglas–Kroll–Hess (DKH2) Hamiltonian,[57,58] segmented all-electron relativistically contracted (SARC) basis set[59] for the Ln elements, and the minimally augmented[60] ma-def2-TZVPP basis set[61,62] was used for atoms in H_2O, OH^- and H_3O^+ species. Diffuse functions in the basis sets of single point energy calculations improved our predicted pK_{a2} and pK_{a3} for values. Also, a study of lanthanide-ligand binding energies reports that basis sets with diffuse functions (ma-def2-TVZP) resulted in Ln-ligand binding energies that are energetically more favorable.[63] Additional discussion is provided in the SI regarding the use of basis sets with diffuse functions in geometry optimizations. The M06 functional is reliable for calculating thermodynamic properties,[64] including those with the lanthanides.[49,50] The efficiency of DKH2 and SARC basis set in electronic structure calculations with lanthanides has been shown[65–67]. Relativistic effects need to be considered for accurate calculations with Ln elements[68]. For geometry optimizations and frequency calculations, we used small core effective core potentials in which core electrons interact with the valence electrons,[69] and for all-electron single-point energy calculations we used scalar relativistic approximations (Douglas−Kroll−Hess approach).[57,58,70] The more accurate all-electron calculations are computationally too expensive for geometry optimizations (four species per Ln^{III} ion, 15 Ln^{III} ions, **Figure 5-3**). All electronic structure calculations were done with ORCA[71] using the resolution of identity chain of sphere (RIJCOSX)[72] to improve the calculations efficiency using “Grid7” and “GridX7” grids.

With reaction free energies (**equations 5.2 – 5.4**) quantified from electronic structure calculations, the values of pK_{a2} and pK_{a3} for each Ln^{III} ion were calculated using relative reaction free energies **(equations 5.5 – 5.10**), based on the absolute pK_{a1} values for each Ln^{III} ion predicted with constrained AIMD simulations in the solution phase. All simulations and calculations correspond to aqueous solution (explicit solvent for pK_{a1}, implicit solvent for pK_{a2} and pK_{a3}); no gas phase energies were used.

5.3. Results and Discussion

For each predicted pK_a value, of each Ln^{III} ion, we calculated mean absolute deviations (MAD) of our calculations with experimentally measured hydrolysis constants in the literature. Our calculated Ln^{III} ion pK_a values at room temperature in aqueous solution are reported in **Table 5-1**. The +/- margin of error in pK_{a1} predictions were quantified as described in section 5.2.2, and carries over to pK_{a2} and pK_{a3} predictions. The small margins of error (<1 pK_a) indicate that the trajectories are equilibrated, and sufficient sampling was obtained in 15 ps of NVT simulation. The margins of error were not used to lower the MAD values, the MAD values reported represent the absolute deviation of our calculations with experimentally reported hydrolysis constants. Our predicted first hydrolysis (pK_{a1}) constants have MAD values that range between 0.5 and 2.4 pK_a units from experiment; the second hydrolysis (pK_{a2}) constants range between 0.2 and 4.5 pK_a units, and the third hydrolysis (pK_{a3}) constants range between 0.4 and 7.1 pK_a units.

Table 5-1: Ln^{III} ion hydrolysis constants calculated in this work, and their MAD to experimentally measured hydrolysis constants.

	First Hydrolysis		Second Hydrolysis		Third Hydrolysis	
	pK_{a1}	**MAD**	**pK_{a2}**	**MAD**	**pK_{a3}**	**MAD**
La	8.4 ± 0.9	0.7	13.4	4.5	19.6	7.1
Ce	8.8 ± 0.3	0.5	17.1	0.8	20.0	5.3
Pr	9.0 ± 0.5	0.6	14.0	-	20.8	4.9
Nd	8.3 ± 0.5	0.5	12.9	3.8	17.8	6.6
Pm	8.7 ± 0.5	2.2	12.8	-	19.9	-
Sm	7.0 ± 0.1	1.1	10.9	4.5	16.7	6.9
Eu	10.1 ± 0.2	2.4	19.8	-	23.9	0.4
Gd	8.4 ± 0.4	0.6	15.8	0.3	17.2	5.5
Tb	9.1 ± 0.5	1.6	15.4	-	20.4	3.0
Dy	9.1 ± 0.1	1.6	16.1	-	21.2	1.7
Ho	8.4 ± 0.5	0.9	15.2	1.1	18.8	3.9
Er	7.2 ± 0.9	0.9	11.8	4.2	15.9	6.8
Tm	8.9 ± 0.1	1.7	12.1	3.9	15.8	6.1
Yb	8.2 ± 0.3	0.9	15.1	0.2	18.3	3.6
Lu	7.9 ± 0.9	0.9	14.0	1.2	17.1	4.3

Our pK_{a1} predictions have an average MAD value for all Ln elements of 1.1 pK_a units. A significant deviation from experiments comes from a single set of measurements[73] that underestimates the first hydrolysis constant by ~2 – 4 pK_a units compared to the other reported measurements. Higher MAD values were obtained for pK_{a2} and pK_{a3} with average MAD values for all Ln elements of 2.5 and 4.7 pK_a units respectively. This is, in part, because less experimental measurements have been done for the second and third hydrolysis constants, and, in part, because the magnitude of pK_a values also increase for the second and third hydrolysis constants.

Table 5-2 contains our results and all the experimentally measured Ln^{III} ion hydrolysis constants, along with their references, that were used to calculate the MAD values. **Table 5-2** provides an updated compilation of all experimentally measured Ln^{III} ion hydrolysis constants in a single, useful reference table. There is a large variation in

experimentally measured pK_{a1} values, generally more pronounced for the later lanthanides. For most elements, our predicted pK_{a1} values, are inside the range of experimentally measured first hydrolysis constants with a few exceptions: we slightly overestimate the pK_{a1} values for Eu, Tb, Dy, and Tm, as well as for Pm which only has a single experimental measurement. On the other hand, for pK_{a2} and pK_{a3} lower pK_a values are predicted in most instances. Basis sets with diffuse functions improved the calculated pK_{a2} and pK_{a3} values with respect to experiment: our underestimated values could be due to the fact that the interactions between Ln electrons with oxygen electrons, far from the nuclei, is not being accurately replicated with the level of theory used in this work.

Table 5-2: Ln^{III} ion hydrolysis constants calculated in this work, and experimentally measured hydrolysis constants reported in the literature.

	First Hydrolysis		Second Hydrolysis		Third Hydrolysis	
	pK_{a1}	**Source**	**pK_{a2}**	**Source**	**pK_{a3}**	**Source**
La	7.4	[73]				
	7.77	[74]				
	8.14	[75]				
	8.4 ± 0.9	This Work				
	8.4	[76]				
	8.5	[2]				
	8.5	[77]				
	8.52	[78]			19.6	This Work
	8.53	[79]	13.4	This Work	26.12	[80]
	8.6	[81]	17.9	[81]	26.56	[79]
	8.81	[82]			26.84	[78]
	8.87	[83]			27.3	[81]
	8.89	[84]				
	9.1	[85]				
	9.2	[86]				
	9.33	[87]				
	9.94	[88]				
	10	[89]				
	10.0	[90]				
	10.1	[91]				
	10.3	[92]				
Ce	8.02	[75]				
	8.1	[93]				
	8.31	[84]				
	8.34	[82]			20.0	This Work
	8.34	[77]	16.3	[93]	23.65	[94]
	8.43	[79]	17.1	This Work	26.0	[93]
	8.8 ± 0.3	This Work			26.25	[79]
	9.1	[95]				
	9.3	[96]				
Pr	7.1	[73]				
	7.86	[75]				
	8.1	[77]				
	8.3	[84]				
	8.32	[82]				
	8.32	[79]				
	8.5	[96]	14.0	This Work	20.8	This Work
	8.5	[97]			25.66	[79]
	8.54	[83]				

	8.82	[87]				
	8.94	[98]				
	9 ± 0.5	This Work				
	9.0	[90]				
	9.5	[92]				
Nd	7	[73]	9.2	[100]	17.8	This Work
	7.76	[75]	12.9	This Work	23.54	[80]
	8.0	[2]	16.2	[99]	23.8	[101]
	8.0	[77]	17.35	[103]	23.9	[102]
	8.1	[99]			24.0	[100]
	8.13	[84]			24.3	[99]
	8.18	[82]			25.16	[79]
	8.24	[79]			26.2	[103]
	8.3 ± 0.5	This Work				
	8.5	[96]				
	8.5	[97]				
	8.7	[87]				
	9.0	[90]				
	9.4	[104]				
	9.46	[88]				
Pm	6.5	[73]	12.8	This Work	19.9	This Work
	8.7 ± 0.5	This Work				
Sm	4.4	[73]	10.9	This Work	16.7	This Work
	7.0 ± 0.1	This Work	15.0	[105]	22.7	[105]
	7.11	[78]	15.84	[78]	23.44	[78]
	7.5	[105]			24.62	[79]
	7.6	[75]				
	7.84	[82]				
	7.84	[84]				
	7.9	[77]				
	8.02	[79]				
	8.61	[87]				
	8.9	[90]				
Eu	4.8	[73]	19.8	This Work	23.9	This Work
	6.7	[106]			24.34	[79]
	7.3	[107]				
	7.49	[75]				
	7.49	[108]				
	7.66	[84]				
	7.76	[82]				
	7.8	[77]				
	7.91	[79]				
	8	[85]				

	8.08	[109]				
	8.1	[110]				
	8.2	[111]				
	8.31	[112]				
	8.34	[83]				
	8.58	[87]				
	8.7	[113]				
	10.1 ± 0.2	This Work				
Gd	7.1	[73]	15.16 15.8 15.82	[115] This Work [116]	17.2 21.9 22.16 23.92	This Work [114] [80] [79]
	7.3	[114]				
	7.36	[75]				
	7.83	[82]				
	7.87	[84]				
	7.87	[79]				
	7.87	[115]				
	8	[77]				
	8.2	[89]				
	8.3	[85]				
	8.44	[116]				
	8.4 ± 0.4	This Work				
	8.62	[87]				
	9.2	[117]				
Tb	5.2	[73]	15.4	This Work	20.4 23.43	This Work [79]
	7.18	[75]				
	7.55	[115]				
	7.6	[84]				
	7.64	[82]				
	7.74	[79]				
	7.9	[77]				
	8.43	[87]				
	8.44	[116]				
	9.1 ± 0.5	This Work				
Dy	5.6	[73]	16.1	This Work	21.2 22.92	This Work [79]
	7.5	[118]				
	7.53	[84]				
	7.59	[82]				
	7.72	[79]				
	8.0	[77]				
	8.37	[87]				
	9.1 ± 0.1	This Work				
	5.7	[73]				
	6.8	[75]				
	7.43	[84]				

Ho	7.56 7.66 7.85 8 8.14 8.31 8.4 ± 0.5	[82] [79] [74] [77] [119] [87] This Work	15.2 16.25	This Work [79]	18.8 22.71	This Work [79]
Er	5.5 6.3 6.56 7.2 ± 0.9 7.46 7.52 7.63 7.9 8.16 8.26 8.4 9	[73] [120] [75] This Work [84] [82] [79] [77] [83] [87] [88] [121]	11.8 14.5 16.15 17.4	This Work [2] [79] [89]	15.9 22.23 23.1	This Work [79] [2]
Tm	4.4 6.36 7.34 7.39 7.51 7.7 8.22 8.58 8.9 ± 0.0	[73] [75] [84] [82] [79] [77] [87] [122] This Work	12.1 15.98	This Work [79]	15.8 21.91	This Work [79]
Yb	4.3 6.24 7.24 7.31 7.45 7.7 7.7 8.0 8.19 8.4 8.2 ± 0.3 8.6	[73] [75] [82] [84] [79] [123] [77] [85] [87] [124] This Work [92]	15.1 15.5 15.59	This Work [123] [79]	18.3 20.68 21.72 23.2	This Work [80] [79] [123]
	3.5 6.04 6.6	[73] [75] [96]				

Lu	7.27 7.33 7.41 7.6 7.7 7.9 ± 0.9 8.0 8.11 8.17	[82] [84] [79] [77] [85] This Work [125] [83] [87]	14.0 15.21	This Work [79]	17.1 21.43	This Work [79]

The calculated pK_a values in this work agree with the well observed trend that Ln^{III} ion acidity increases from the lighter to the heavier lanthanides. However, our predicted pK_{a1} values show higher constants (lower acidity than experiment) for the middle lanthanides (Eu – Dy). As observed in experiment, our calculations report increasing hydrolysis constants from the first to the third hydrolysis reactions within each Ln^{III} aqua ion.

Electronic structure calculations, which can generate relative pK_a values, are typically combined with an experimental quantity, most commonly the free energy of proton hydration, to predict absolute pK_a values via thermodynamic integration;[126–133] using implicit solvent models[134,135] to model aqueous conditions. In this work, we calculate absolute values of pK_{a1} from solution phase AIMD simulations, and use that as the reference point to calculate pK_{a2} and pK_{a3} with electronic structure calculations in an implicit solvation model. Despite that constrained AIMD simulations are computationally more expensive than electronic structure calculations, they have the advantage that absolute pK_a values in the condensed phase can be obtained due to periodic conditions. AIMD simulations also allow to include explicit solvation which is critical to accurately predict pK_a values in species with a large conformational space, as has been observed

with metal ions,[130,131] as well as organic compounds with multiple Brønsted acid sites.[132] Additionally, with recently available Ln pseudopotentials and basis sets,[22] larger periodic systems, such as Ln-ligands complexes in solution or porous materials are within reach of constrained AIMD simulations. This is relevant in the case of Ln^{III} ions due to a wide range of reported experimental values, for example the first hydrolysis constant Lu^{III} has reported values between 3.5 and 8.17 (**Table 5-2**). Constrained AIMD simulations will be useful to determine the Brønsted acidity of Ln-containing systems, such as those described in the Introduction, with multiple acidic sites.

5.4. Conclusions

Absolute pK_a values of lanthanide-containing species can be calculated with Bluemoon AIMD simulations. This is shown with the first hydrolysis constant of all Ln^{III} aqua ions, which are the best characterized Ln^{III} complexes with multiple Brønsted acidic sites along the entire Ln series. For each Ln^{III} aqua ion, the remaining pK_a sites were calculated using electronic structure calculations that include relativistic effects with respect to the pK_a of the acidic site quantified with constrained AIMD simulations. This approach is particularly advantageous to characterize the Brønsted acidity of Ln^{III}-ligand complexes, or Ln-containing systems, which have multiple acidic sites and measured pK_a values cannot be connected with a particular acidic group.

Chapter 5 References

(1) Housecroft, C. E.; Sharpe, A. G. *Inorganic Chemistry*, Second.; Pearson Education Limited, 2005.

(2) Smith, R. M.; Martell, A. E. *Critical Stability Constants: Inorganic Complexes*; Springer, 1976; Vol. 4.

(3) Abergel, R. J.; Warner, J. A.; Shuh, D. K.; Raymond, K. N. Enterobactin Protonation and Iron Release: Structural Characterization of the Salicylate Coordination Shift in Ferric Enterobactin. *J. Am. Chem. Soc.* **2006**, *128* (27), 8920–8931. https://doi.org/10.1021/ja062046j.

(4) Bonificio, W. D.; Clarke, D. R. Rare-Earth Separation Using Bacteria. *Environ. Sci. Technol. Lett.* **2016**, *3* (4), 180–184. https://doi.org/10.1021/acs.estlett.6b00064.

(5) Lauffer, R. B. Paramagnetic Metal Complexes as Water Proton Relaxation Agents for NMR Imaging: Theory and Design. *Chem. Rev.* **1987**, *87* (5), 901–927.

(6) Micskei, K.; Helm, L.; Brucher, E.; Merbach, A. E. Oxygen-17 NMR Study of Water Exchange on Gadolinium Polyaminopolyacetates [Gd(DTPA)(H2O)]2- and [Gd(DOTA)(H2O)]- Related to NMR Imaging. *Inorg. Chem.* **1993**, *32* (18), 3844–3850. https://doi.org/10.1021/ic00070a013.

(7) Grobner, T.; Prischl, F. C. Gadolinium and Nephrogenic Systemic Fibrosis. *Kidney Int.* **2007**, *72* (3), 260–264. https://doi.org/https://doi.org/10.1038/sj.ki.5002338.

(8) Vogt, E. T. C.; Weckhuysen, B. M. Fluid Catalytic Cracking: Recent Developments on the Grand Old Lady of Zeolite Catalysis. *Chem. Soc. Rev.* **2015**, *44* (20), 7342–7370. https://doi.org/10.1039/C5CS00376H.

(9) Schüßler, F.; Pidko, E. A.; Kolvenbach, R.; Sievers, C.; Hensen, E. J. M.; van Santen, R. A.; Lercher, J. A. Nature and Location of Cationic Lanthanum Species in High Alumina Containing Faujasite Type Zeolites. *J. Phys. Chem. C* **2011**, *115* (44), 21763–21776. https://doi.org/10.1021/jp205771e.

(10) Noda, T.; Suzuki, K.; Katada, N.; Niwa, M. Combined Study of IRMS-TPD Measurement and DFT Calculation on Brønsted Acidity and Catalytic Cracking Activity of Cation-Exchanged Y Zeolites. *J. Catal.* **2008**, *259* (2), 203–210. https://doi.org/https://doi.org/10.1016/j.jcat.2008.08.004.

(11) Vogel, D. J.; Nenoff, T. M.; Rimsza, J. M. Tuned Hydrogen Bonding in Rare-Earth Metal–Organic Frameworks for Design of Optical and Electronic Properties: An Exemplar Study of Y–2,5-Dihydroxyterephthalic Acid. *ACS Appl. Mater. Interfaces* **2020**, *12* (4), 4531–4539. https://doi.org/10.1021/acsami.9b20513.

(12) Fitriyanto, N. A.; Fushimi, M.; Matsunaga, M.; Pertiwiningrum, A.; Iwama, T.; Kawai, K. Molecular Structure and Gene Analysis of Ce3+-Induced Methanol Dehydrogenase of Bradyrhizobium Sp. MAFF211645. *J. Biosci. Bioeng.* **2011**, *111* (6), 613–617. https://doi.org/10.1016/j.jbiosc.2011.01.015.

(13) Hibi, Y.; Asai, K.; Arafuka, H.; Hamajima, M.; Iwama, T.; Kawai, K. Molecular Structure of La3+-Induced Methanol Dehydrogenase-like Protein in Methylobacterium Radiotolerans. *J. Biosci. Bioeng.* **2011**, *111* (5), 547–549. https://doi.org/10.1016/j.jbiosc.2010.12.017.

(14) Nakagawa, T.; Mitsui, R.; Tani, A.; Sasa, K.; Tashiro, S.; Iwama, T.; Hayakawa,

T.; Kawai, K. A Catalytic Role of XoxF1 as La3+-Dependent Methanol Dehydrogenase in Methylobacterium Extorquens Strain AM1. *PLoS One* **2012**, *7* (11), 1–7. https://doi.org/10.1371/journal.pone.0050480.

(15) Cook, E. C.; Featherston, E. R.; Showalter, S. A.; Cotruvo, J. A. Structural Basis for Rare Earth Element Recognition by Methylobacterium Extorquens Lanmodulin. *Biochemistry* **2019**, *58* (2), 120–125. https://doi.org/10.1021/acs.biochem.8b01019.

(16) Good, N. M.; Fellner, M.; Demirer, K.; Hu, J.; Hausinger, R. P.; Martinez-Gomez, N. C. Lanthanide-Dependent Alcohol Dehydrogenases Require an Essential Aspartate Residue for Metal Coordination and Enzymatic Function. *J. Biol. Chem.* **2020**, *295* (24), 8272–8284. https://doi.org/10.1074/jbc.RA120.013227.

(17) Krieger, E.; Nielsen, J. E.; Spronk, C. A. E. M.; Vriend, G. Fast Empirical PKa Prediction by Ewald Summation. *J. Mol. Graph. Model.* **2006**, *25* (4), 481–486. https://doi.org/https://doi.org/10.1016/j.jmgm.2006.02.009.

(18) Bas, D. C.; Rogers, D. M.; Jensen, J. H. Very Fast Prediction and Rationalization of PKa Values for Protein–Ligand Complexes. *Proteins Struct. Funct. Bioinforma.* **2008**, *73* (3), 765–783. https://doi.org/https://doi.org/10.1002/prot.22102.

(19) Anandakrishnan, R.; Aguilar, B.; Onufriev, A. V. H++ 3.0: Automating PK Prediction and the Preparation of Biomolecular Structures for Atomistic Molecular Modeling and Simulations. *Nucleic Acids Res.* **2012**, *40* (W1), W537–W541. https://doi.org/10.1093/nar/gks375.

(20) Nash, K. L. The Chemistry of TALSPEAK: A Review of the Science. *Solvent Extr. Ion Exch.* **2015**, *33* (1), 1–55. https://doi.org/10.1080/07366299.2014.985912.

(21) Goedecker, S.; Teter, M.; Hutter, J. Separable Dual-Space Gaussian Pseudopotentials. *Phys. Rev. B - Condens. Matter Mater. Phys* **1996**, No. 54, 1703–1710.

(22) Lu, J. B.; Cantu, D. C.; Nguyen, M. T.; Li, J.; Glezakou, V. A.; Rousseau, R. Norm-Conserving Pseudopotentials and Basis Sets to Explore Lanthanide Chemistry in Complex Environments. *J. Chem. Theory Comput.* **2019**, *15*, 5987–5997. https://doi.org/10.1021/acs.jctc.9b00553.

(23) Cao, X.; Dolg, M. Valence Basis Sets for Relativistic Energy-Consistent Small-Core Lanthanide Pseudopotentials. *J. Chem. Phys.* **2001**, *115* (16), 7348–7355. https://doi.org/10.1063/1.1406535.

(24) Weigand, A.; Cao, X.; Yang, J.; Dolg, M. Quasirelativistic F-in-Core Pseudopotentials and Core-Polarization Potentials for Trivalent Actinides and Lanthanides: Molecular Test for Trifluorides. *Theor. Chem. Acc.* **2010**, *126* (3), 117–127. https://doi.org/10.1007/s00214-009-0584-2.

(25) Ross, R. B.; Gayen, S.; Ermler, W. C. Ab Initio Relativistic Effective Potentials with Spin-Orbit Operators. V. Ce through Lu. *J. Chem. Phys.* **1994**, *100* (11), 8145–8155. https://doi.org/10.1063/1.466809.

(26) Cundari, T. R.; Stevens, W. J. Effective Core Potential Methods for the Lanthanides. *J. Chem. Phys.* **1993**, *98* (7), 5555–5565. https://doi.org/10.1063/1.464902.

(27) Hay, P. J.; Wadt, W. R. Ab Initio Effective Core Potentials for Molecular

Calculations. Potentials for the Transition Metal Atoms Sc to Hg. *J. Chem. Phys.* **1985**, *82* (1), 270–283. https://doi.org/10.1063/1.448799.

(28) Dolg, M.; Stoll, H. Pseudopotential Study of the Rare Earth Monohydrides, Monoxides and Monofluorides. *Theor. Chim. Acta* **1989**, *75*, 369–387.

(29) Dolg, M.; Stoll, H.; Preuss, H. Energy-Adjusted Ab Initio Pseudopotentials for the Rare Earth Elements. *J. Chem. Phys.* **1989**, *90*, 1730–1734.

(30) Shiery, R. C.; Fulton, J. L.; Balasubramanian, M.; Nguyen, M.-T.; Lu, J.-B.; Li, J.; Rousseau, R.; Glezakou, V.-A.; Cantu, D. C. Coordination Sphere of Lanthanide Aqua Ions Resolved with Ab Initio Molecular Dynamics and X-Ray Absorption Spectroscopy. *Inorg. Chem.* **2021**, *60* (5), 3117–3130. https://doi.org/10.1021/acs.inorgchem.0c03438.

(31) Kaliakin, D. S.; Sobrinho, J. A.; Monteiro, J. H. S. K.; de Bettencourt-Dias, A.; Cantu, D. C. Solution Structure of a Europium–Nicotianamine Complex Supports That Phytosiderophores Bind Lanthanides. *Phys. Chem. Chem. Phys.* **2021**, *23* (7), 4287–4299. https://doi.org/10.1039/D0CP06150F.

(32) Carter, E. A.; Ciccotti, G.; Hynes, J. T.; Kapral, R. Constrained Reaction Coordinate Dynamics for the Simulation of Rare Events. *Chem. Phys. Lett.* **1989**, *156* (5), 472–477. https://doi.org/https://doi.org/10.1016/S0009-2614(89)87314-2.

(33) Sprik, M.; Ciccotti, G. Free Energy from Constrained Molecular Dynamics. *J. Chem. Phys.* **1998**, *109* (18), 7737–7744. https://doi.org/10.1063/1.477419.

(34) Sprik, M. Computation of the PK of Liquid Water Using Coordination Constraints. *Chem. Phys.* **2000**, *258* (2), 139–150. https://doi.org/https://doi.org/10.1016/S0301-0104(00)00129-4.

(35) Sulpizi, M.; Sprik, M. Acidity Constants from {DFT}-Based Molecular Dynamics Simulations. *J. Phys. Condens. Matter* **2010**, *22* (28), 284116. https://doi.org/10.1088/0953-8984/22/28/284116.

(36) Cheng, J.; Liu, X.; VandeVondele, J.; Sulpizi, M.; Sprik, M. Redox Potentials and Acidity Constants from Density Functional Theory Based Molecular Dynamics. *Acc. Chem. Res.* **2014**, *47* (12), 3522–3529. https://doi.org/10.1021/ar500268y.

(37) Hass, K. C.; Schneider, W. F.; Curioni, A.; Andreoni, W. The Chemistry of Water on Alumina Surfaces: Reaction Dynamics from First Principles. *Science (80-.).* **1998**, *282* (5387), 265–268. https://doi.org/10.1126/science.282.5387.265.

(38) Ivanov, I.; Chen, B.; Raugei, S.; Klein, M. L. Relative PKa Values from First-Principles Molecular Dynamics: The Case of Histidine Deprotonation. *J. Phys. Chem. B* **2006**, *110* (12), 6365–6371. https://doi.org/10.1021/jp056750i.

(39) De Meyer, T.; Ensing, B.; Rogge, S. M. J.; De Clerck, K.; Meijer, E. J.; Van Speybroeck, V. Acidity Constant (PK(a)) Calculation of Large Solvated Dye Molecules: Evaluation of Two Advanced Molecular Dynamics Methods. *Chemphyschem* **2016**, *17* (21), 3447–3459. https://doi.org/10.1002/cphc.201600734.

(40) Kılıç, M.; Ensing, B. Acidity Constants of Lumiflavin from First Principles Molecular Dynamics Simulations. *Phys. Chem. Chem. Phys.* **2014**, *16* (35), 18993–19000. https://doi.org/10.1039/C4CP01450B.

(41) Chen, Y.-L.; Doltsinis, N. L.; Hider, R. C.; Barlow, D. J. Prediction of Absolute Hydroxyl PKa Values for 3-Hydroxypyridin-4-Ones. *J. Phys. Chem. Lett.* **2012**, *3*

(20), 2980–2985. https://doi.org/10.1021/jz301061m.
(42) Tummanapelli, A. K.; Vasudevan, S. Dissociation Constants of Weak Acids from Ab Initio Molecular Dynamics Using Metadynamics: Influence of the Inductive Effect and Hydrogen Bonding on PKa Values. *J. Phys. Chem. B* **2014**, *118* (47), 13651–13657. https://doi.org/10.1021/jp5088898.
(43) Schilling, M.; Luber, S. Determination of PKa Values via Ab Initio Molecular Dynamics and Its Application to Transition Metal-Based Water Oxidation Catalysts. *Inorganics* **2019**, *7* (6). https://doi.org/10.3390/inorganics7060073.
(44) Perdew, J. P.; Burke, K.; Ernzerhof, M. Generalized Gradient Approximation Made Simple. *Phys. Rev. Lett.* **1996**, *77* (18), 3865–3868.
(45) Hutter, J.; Iannuzzi, M.; Schiffmann, F.; Vandevondele, J. Cp2k: Atomistic Simulations of Condensed Matter Systems. *Wiley Interdiscip. Rev. Comput. Mol. Sci.* **2014**, *4* (1), 15–25. https://doi.org/10.1002/wcms.1159.
(46) VandeVondele, J.; Krack, M.; Mohamed, F.; Parrinello, M.; Chassaing, T.; Hutter, J.; Fast, Q. Fast and Accurate Density Functional Calculations Using a Mixed Gaussian and Plane Waves Approach. *Comput. Phys. Commun.* **2005**, *167* (2), 103–128.
(47) Lin, I. C.; Seitsonen, A. P.; Tavernelli, I.; Rothlisberger, U. Structure and Dynamics of Liquid Water from Ab Initio Molecular Dynamics-Comparison of BLYP, PBE, and RevPBE Density Functionals with and without van Der Waals Corrections. *J. Chem. Theory Comput.* **2012**, *8* (10), 3902–3910. https://doi.org/10.1021/ct3001848.
(48) Chen, M.; Ko, H. Y.; Remsing, R. C.; Calegari Andrade, M. F.; Santra, B.; Sun, Z.; Selloni, A.; Car, R.; Klein, M. L.; Perdew, J. P.; Wu, X. Ab Initio Theory and Modeling of Water. *Proc. Natl. Acad. Sci. U. S. A.* **2017**, *114* (41), 10846–10851. https://doi.org/10.1073/pnas.1712499114.
(49) Grimmel, S.; Schoendorff, G.; Wilson, A. K. Gauging the Performance of Density Functionals for Lanthanide-Containing Molecules. *J. Chem. Theory Comput.* **2016**, *12* (3), 1259–1266. https://doi.org/10.1021/acs.jctc.5b01193.
(50) Jaoul, A.; Nocton, G.; Clavaguéra, C. Assessment of Density Functionals for Computing Thermodynamic Properties of Lanthanide Complexes. *ChemPhysChem* **2017**, *18* (19), 2688–2696. https://doi.org/10.1002/cphc.201700629.
(51) VandeVondele, J.; Hutter, J. Gaussian Basis Sets for Accurate Calculations on Molecular Systems in Gas and Condensed Phases. *J. Chem. Phys.* **2007**, *127* (11). https://doi.org/10.1063/1.2770708.
(52) Grimme, S.; Antony, J.; Ehrlich, S.; Krieg, H. A Consistent and Accurate Ab Initio Parametrization of Density Functional Dispersion Correction (DFT-D) for the 94 Elements H-Pu. *J. Chem. Phys.* **2010**, *132* (15). https://doi.org/10.1063/1.3382344.
(53) Barone, V.; Cossi, M. Quantum Calculation of Molecular Energies and Energy Gradients in Solution by a Conductor Solvent Model. *J. Phys. Chem. A* **1998**, *102* (11), 1995–2001. https://doi.org/10.1021/jp9716997.
(54) Zhao, Y.; Truhlar, D. G. The M06 Suite of Density Functionals for Main Group Thermochemistry, Thermochemical Kinetics, Noncovalent Interactions, Excited States, and Transition Elements: Two New Functionals and Systematic Testing of

Four M06-Class Functionals and 12 Other Function. *Theor. Chem. Acc.* **2008**, *120* (1–3), 215–241. https://doi.org/10.1007/s00214-007-0310-x.

(55) Cao, X.; Dolg, M. Segmented Contraction Scheme for Small-Core Lanthanide Pseudopotential Basis Sets. *J. Mol. Struct. THEOCHEM* **2002**, *581* (1), 139–147. https://doi.org/https://doi.org/10.1016/S0166-1280(01)00751-5.

(56) Dunning, T. H. Gaussian Basis Sets for Use in Correlated Molecular Calculations. I. The Atoms Boron through Neon and Hydrogen. *J. Chem. Phys.* **1989**, *90* (2), 1007–1023. https://doi.org/10.1063/1.456153.

(57) Douglas, M.; Kroll, N. M. Quantum Electrodynamical Corrections to the Fine Structure of Helium. *Ann. Phys. (N. Y).* **1974**, *82* (1), 89–155. https://doi.org/10.1016/0003-4916(74)90333-9.

(58) Hess, B. A. Applicability of the No-Pair Equation with Free-Particle Projection Operators to Atomic and Molecular Structure Calculations. *Phys. Rev. A* **1985**, *32* (2), 756–763. https://doi.org/10.1103/PhysRevA.32.756.

(59) Pantazis, D. A.; Chen, X. Y.; Landis, C. R.; Neese, F. All-Electron Scalar Relativistic Basis Sets for Third-Row Transition Metal Atoms. *J. Chem. Theory Comput.* **2008**, *4* (6), 908–919. https://doi.org/10.1021/ct800047t.

(60) Zheng, J.; Xu, X.; Truhlar, D. G. Minimally Augmented Karlsruhe Basis Sets. *Theor. Chem. Acc.* **2011**, *128* (3), 295–305. https://doi.org/10.1007/s00214-010-0846-z.

(61) Woon, D. E.; Dunning, T. H. Gaussian Basis Sets for Use in Correlated Molecular Calculations. I. The Atoms Boron through Neon and Hydrogen. *J. Chem. Phys.* **1988**, *90*, 1007–1023. https://doi.org/10.1063/1.470645.

(62) Weigend, F.; Ahlrichs, R. Balanced Basis Sets of Split Valence, Triple Zeta Valence and Quadruple Zeta Valence Quality for H to Rn: Design and Assessment of Accuracy. *Phys. Chem. Chem. Phys.* **2005**, *7*, 3297–3305. https://doi.org/10.1039/b508541a.

(63) Vo, M. N.; Bryantsev, V. S.; Johnson, J. K.; Keith, J. A. Quantum Chemistry Benchmarking of Binding and Selectivity for Lanthanide Extractants. *Int. J. Quantum Chem.* **2018**, *118* (7), e25516. https://doi.org/https://doi.org/10.1002/qua.25516.

(64) Mardirossian, N.; Head-Gordon, M. How Accurate Are the Minnesota Density Functionals for Noncovalent Interactions, Isomerization Energies, Thermochemistry, and Barrier Heights Involving Molecules Composed of Main-Group Elements? *J. Chem. Theory Comput.* **2016**, *12* (9), 4303–4325. https://doi.org/10.1021/acs.jctc.6b00637.

(65) Jorge, F. E.; Martins, L. S. C.; Franco, M. L. All-Electron Double Zeta Basis Sets for the Lanthanides: Application in Atomic and Molecular Property Calculations. *Chem. Phys. Lett.* **2016**, *643*, 84–88. https://doi.org/10.1016/j.cplett.2015.11.013.

(66) de Oliveira, A. Z.; Ferreira, I. B.; Campos, C. T.; Jorge, F. E.; Fantin, P. A. Segmented All-Electron Basis Sets of Triple Zeta Quality for the Lanthanides: Application to Structure Calculations of Lanthanide Monoxides. *J. Mol. Model.* **2019**, *25* (2). https://doi.org/10.1007/s00894-019-3924-8.

(67) Aravena, D.; Neese, F.; Pantazis, D. A. Improved Segmented All-Electron Relativistically Contracted Basis Sets for the Lanthanides. *J. Chem. Theory*

Comput. **2016**, *12* (3), 1148–1156. https://doi.org/10.1021/acs.jctc.5b01048.
(68) Dolg, M. *Computational Methods in Lanthanide and Actinide Chemistry*; Wiley, 2015.
(69) Dolg, M.; Cao, X. Relativistic Pseudopotentials: Their Development and Scope of Applications. *Chem. Rev.* **2012**, *112* (1), 403–480. https://doi.org/10.1021/cr2001383.
(70) Reiher, M. Relativistic Douglas–Kroll–Hess Theory. *WIREs Comput. Mol. Sci.* **2012**, *2* (1), 139–149. https://doi.org/https://doi.org/10.1002/wcms.67.
(71) Neese, F. Software Update: The ORCA Program System, Version 4.0. *Wiley Interdiscip. Rev. Comput. Mol. Sci.* **2018**, *8* (1), 4–9. https://doi.org/10.1002/wcms.1327.
(72) Neese, F.; Wennmohs, F.; Hansen, A.; Becker, U. Efficient, Approximate and Parallel Hartree-Fock and Hybrid DFT Calculations. A "chain-of-Spheres" Algorithm for the Hartree-Fock Exchange. *Chem. Phys.* **2009**, *356* (1–3), 98–109. https://doi.org/10.1016/j.chemphys.2008.10.036.
(73) Guillaumont, R.; Desire, B.; Galin, M. Première Constante d'hydrolyse Des Lanthanides. *Radiochem. Radioanal. Lett* **1971**, *8* (3), 189–197.
(74) Chirkst, D. E.; Lobacheva, O. L.; Dzhevaga, N. V. Thermodynamic Properties of Lanthanum(III) and Holmium(III) Hydroxo Compounds. *Russ. J. Phys. Chem. A* **2011**, *85* (11), 1872–1875. https://doi.org/10.1134/S0036024411110057.
(75) Nazarenko, V. A., Antonovich, V. P., and Nevskaya, E. M. *Hydrolysis of Metal Ions in Dilute Solutions*; Atomizdat: Moscow, 1979.
(76) Wheelwright, E. J.; Spedding, F. H.; Schwarzenbach, G. The Stability of the Rare Earth Complexes with Ethylenediaminetetraacetic Acid. *J. Am. Chem. Soc.* **1953**, *75* (17), 4196–4201.
(77) Mishustin, A. I. Estimate of the Stability Constants of Trivalent Actinide and Lanthanide Complexes with O-Donor Ligands in Aqueous Solutions. *Russ. J. Inorg. Chem.* **2010**, *55* (5), 746–752. https://doi.org/10.1134/S0036023610050141.
(78) İçhedef, Ç.; Şişmanoğlu, T.; Teksöz, S. Hydrolytic Behavior of La3+ and Sm3+ at Various Temperatures. *J. Solution Chem.* **2018**, *47* (2), 220–230. https://doi.org/10.1007/s10953-018-0727-y.
(79) Yakubovich, Y. Y.; Alekseev, V. G. Hydrolysis Constants of Tervalent Lanthanum and Lanthanide Ions in 0.1 M KNO3 Solution. *Russ. J. Inorg. Chem.* **2012**, *57* (6), 911–915. https://doi.org/10.1134/S0036023612060265.
(80) Fatin-Rouge, N.; Bünzli, J. C. G. Thermodynamic and Structural Study of Inclusion Complexes between Trivalent Lanthanide Ions and Native Cyclodextrins. *Inorganica Chim. Acta* **1999**, *293* (1), 53–60. https://doi.org/10.1016/S0020-1693(99)00227-3.
(81) Kragten, J.; Decnop-Weever, L. G. Hydroxide Complexes of Lanthanides—VIII: Lanthanum (III) in Perchlorate Medium. *Talanta* **1987**, *34* (10), 861–864.
(82) Klungness, G. D.; Byrne, R. H. Comparative Hydrolysis Behavior of the Rare Earths and Yttrium: The Influence of Temperature and Ionic Strength. *Polyhedron* **2000**, *19* (1), 99–107. https://doi.org/10.1016/S0277-5387(99)00332-0.
(83) Ramírez-García, J. J.; Solache-Ríos, M.; Jiménez-Reyes, M.; Rojas-Hernández, A. Solubility and Hydrolysis of La, Pr, Eu, Er, and Lu in 1 M NaCl Ionic Strength at

303 K. *J. Solution Chem.* **2003**, *32* (10), 879–896. https://doi.org/10.1023/B:JOSL.0000013431.95283.56.

(84) Ekberg, Christian, Brown, P. L. Scandium , Yttrium and the Lanthanide Metals. **2016**, No. 1966.

(85) Usherenko, L. N.; Skorik, N. A. Ion Hydrolysis of Rare-Earth Elements, Yttrium, Scandium and Thorium in Water and Water-Ethanol Mixtures. *Zhurnal Neorg. Khimii* **1972**, *17* (11), 2918--+.

(86) Ciavatta, L.; Iuliano, M.; Porto, R. The Hydrolysis of the La (III) Ion in Aqueous Perchlorate Solution at 60 C. *Polyhedron* **1987**, *6* (6), 1283–1290.

(87) Frolova, U. K.; Kumok, V. N.; Serebrennikov, V. V. Hydrolysis of Ions of the Rare Earth Elements and Yttrium in Aqueous Solutions. *Khim. i Khim. Tekhnol* **1966**, *9*, 176–179.

(88) Luo, Q.-H., Shen, M.-C., Bao, X.-L., Ding, Y. A Study on Hydrolytic Polymerization of Lanthanide Ions. *Chin. J. Chem.* **1990**, *5*, 412–422.

(89) Amaya, T.; Kakihana, H.; Maeda, M. The Hydrolysis of Y3+, La3+, Gd3+, and Er3+ Ions in an Aqueous Solution Containing 3 M (Li) ClO4 as an Ionic Medium. *Bull. Chem. Soc. Jpn.* **1973**, *46* (6), 1720–1723.

(90) Moeller, T. Observations on the Rare Earths. LV. Hydrolysis Studies upon Yttrium, and Certain Rare Earth (III) Sulfate Solutions at 25° C. *J. Phys. Chem.* **1946**, *50* (3), 242–250.

(91) Biedermann, G.; Ciavatta, L. *Studies on the Hydrolysis of Metal Ions, Part 35. The Hydrolysis of the Lanthanum Ion, La3+*; 1961.

(92) Burkov, K. A.; Busko, E. A.; Pichugina, I. V. State of Lanthanum, Praeseodymium and Ytterbium Ions in Aqueous Solution. *Russ. J. Inorg. Chem.* **1982**, *27*, 643–647.

(93) Kragten, J.; Decnop-Weever, L. G. Hydroxide Complexes of Cerium (III). *Talanta* **1978**, *25* (3), 147–150.

(94) Teksöz, S.; Acar, Ç.; Ünak, P. Hydrolytic Behavior of Th4+, UO22+, and Ce3+ Ions at Various Temperatures. *J. Chem. Eng. Data* **2009**, *54* (4), 1183–1188. https://doi.org/10.1021/je800601m.

(95) Ciavatta, L.; Porto, R.; Vasca, E. The Hydrolysis of the Cerium (III) Ion, Ce3+, in Aqueous Perchlorate Solutions at 50° C. *Polyhedron* **1988**, *7* (15), 1355–1361.

(96) Sillen, L. G.; Martell, A. E.; Bjerrum, J. *Stability Constants of Metal-Ion Complexes.*; 1964.

(97) Tobias, R. S.; Garrett, A. B. The Thermodynamic Properties of Neodymium Hydroxide Nd (OH) 3, in Acid, Neutral and Alkaline Solutions at 25°; the Hydrolysis of the Neodymium and Praseodymium Ions, Nd3+, Pr3+. *J. Am. Chem. Soc.* **1958**, *80* (14), 3532–3537.

(98) González-Mendoza, R.; López-González, H.; Rojas-Hernández, A. Spectrophotometric Determination of the First Hydrolysis Constant of Praseodymium (III). *Journal of the Mexican Chemical Society*. 2010, pp 51–58. https://doi.org/10.29356/jmcs.v54i1.965.

(99) Kragten, J.; Decnop-Weever, L. G. Hydroxide Complexes of Lanthanides. 7. Neodymium (III) in Perchlorate Medium. *Talanta* **1984**, *31* (9), 731–733.

(100) Wood, S. A., Palmer, D. A., Wesolowski, D. J., & Bénézeth, P. A. The Aqueous

Geochemistry of the Rare Earth Elements and Yttrium. Part XI. The Solubility of Nd (OH) 3 and Hydrolysis of Nd3+ from 30 to 290 C at Saturated Water Vapor Pressure with in-Situ PHm Measurement. *Water–rock Interact. ore Depos. Environ. geochemistry a Tribut. to David Crerar* **2002**, *7*, 229–256.

(101) Makino, H., Yajima, T., Yoshikawa, H., Yui, M., and Sasaki, N. Neodymium(III) Hydrolysis Constants and Solubilities of Nd(III) Hydroxide. *Nippon Kagaku Kaishi* **1993**, *5*, 445–450.

(102) Silva, R. J. Thermodynamic Properties of Chemical Species in Nuclear Waste. Topical Report. The Solubilities of Crystalline Neodymium and Americium Trihydroxides. **1982**.

(103) Neck, V.; Altmaier, M.; Rabung, T.; Lützenkirchen, J.; Fanghänel, T. Thermodynamics of Trivalent Actinides and Neodymium in NaCl, MgCl 2, and CaCl2 Solutions: Solubility, Hydrolysis, and Ternary Ca-M(III)-OH Complexes. *Pure Appl. Chem.* **2009**, *81* (9), 1555–1568. https://doi.org/10.1351/PAC-CON-08-09-05.

(104) Burkov, K. A.; Lilich, L. S.; Ngo, N. D.; Smirnov, A. Y. Potentiometry of Hydrolysis of Neodymium Ions (Nd3+) in 3 Mol (Na)ClO4 Solution. *Russ. J. Inorg. Chem.* **1973**, *18*, 1513–1518.

(105) Kragten, J.; Decnop-Weever, L. G. Hydroxide Complexes of Lanthanides—II Samarium (III) in Perchlorate Medium. *Talanta* **1979**, *26* (12), 1105–1109.

(106) M'Halla, J., Chemla, M., Bury, R., and David, F. Étude Conductimétrique de l'hydrolyse Des Ions Lanthanides Dans l'eau. *J. Chim. Phys.* **1988**, *85*, 121–133.

(107) Caceci, M. S.; Choppin, G. R. The Determination of the First Hydrolysis Constant of Eu (Lll) and Am (Lll). *Radiochim. Acta* **1983**, *33* (2–3), 101–104.

(108) Jiménez-Reyes, M.; Solache-Ríos, M.; Rojas-Hernández, A. Application of the Specific Ion Interaction Theory to the Solubility Product and First Hydrolysis Constant of Europium. *J. Solution Chem.* **2006**, *35* (2), 201–214. https://doi.org/10.1007/s10953-006-9363-z.

(109) Lundqvist, R.; Chen, A.-T.; Suurkuusk, J.; Wadsö, I.; Sokolov, V. B.; Spiridonov, V. P.; Strand, T. G. Hydrophilic Complexes of the Actinides. I. Carbonates of Trivalent Americium and Europium. *Acta Chemica Scandinavica*. 1982, pp 741–750. https://doi.org/10.3891/acta.chem.scand.36a-0741.

(110) Nair, G. M.; Chander, K.; Joshi, J. K. Hydrolysis Constants of Plutonium (Lll) and Americium (Lll). *Radiochim. Acta* **1982**, *30* (1), 37–40.

(111) Ramírez-García, J. J.; Jiménez-Reyes, M.; Solache-Ríos, M.; Fernández-Ramírez, E.; López-González, H.; Rojas-Hernández, A. Solubility and First Hidrolysis Constants of Europium at Different Ionic Strength and 303 K. *J. Radioanal. Nucl. Chem.* **2003**, *257* (2), 299–303. https://doi.org/10.1023/A:1024723527305.

(112) Chirkst, D. E.; Lobacheva, O. L.; Berlinskii, I. V.; Sulimova, M. I. The Thermodynamic Properties of Hydroxo Compounds and the Mechanism of Ion Flotation for Cerium, Europium, and Yttrium. *Russ. J. Phys. Chem. A* **2009**, *83* (12), 2022–2027. https://doi.org/10.1134/S0036024409120036.

(113) Schmidt, K. H.; Sullivan, J. C.; Gordon, S.; Thompson, R. C. Determination of Hydrolysis Constants of Metal Cations by a Transient Conductivity Method. *Inorg. Nucl. Chem. Lett* **1978**, *14* (11), 429–434.

(114) Kragten, J.; Decnop-Weever, L. G. Hydroxide Complexes of Lanthanides—III Gadolinium (III) in Perchlorate Medium. *Talanta* **1980**, *27* (12), 1047–1050.
(115) Garcia Rodenas, L. and Liberman, S. J. Hydrolysis of Gadolinium(III) in Light and Heavy Water. *Talanta* **1991**, *38*, 313–318.
(116) Moutte, A. and Guillaumont, R. Complexes Citriques d'actinium et de Curium. *Rev. Chim. Miner.* **1969**, *6*, 603–610.
(117) Ngo, N. D.; Burkov, K. A. State of Gadolineum Ions in Aqueous Solution. *Russ. J. Inorg. Chem.* **1974**, *19*, 1249–1251.
(118) Vasca, E.; Ferri, D.; Manfredi, C.; Fantasma, F.; Caruso, T.; Fontanella, C.; Vero, S. On the Hydrolysis of the Dysprosium(III) Ion. *Chem. Speciat. Bioavailab.* **2004**, *16* (1–2), 71–77. https://doi.org/10.3184/095422904782775135.
(119) Stepanchikova, S. A.; Biteikina, R. P. Spectrophotometric Study of Holmium Complexation in KOH Solutions at 25°C. *Russ. J. Inorg. Chem.* **2006**, *51* (8), 1315–1319. https://doi.org/10.1134/S0036023606080201.
(120) Kragten, J.; Decnop-Weever, L. G. Hydroxide Complexes of Lanthanides—V: Erbium (III) in Perchlorate Medium. *Talanta* **1983**, *30* (2), 131–133.
(121) Rizkalla, E. N.; Choppin, G. R. Chapter 103 Hydration and Hydrolysis of Lanthanides. *Handb. Phys. Chem. Rare Earths* **1991**, *15*, 393–442. https://doi.org/10.1016/S0168-1273(05)80009-1.
(122) Stepanchikova, S. A.; Biteykina, R. P.; Sava, A. A. An Experimental Study of Hydrolytic Behavior of Thulium in Basic and Near-Neutral Solutions. *Open J. Inorg. Chem.* **2013**, *03* (02), 42–47. https://doi.org/10.4236/ojic.2013.32006.
(123) Kragten, J.; Decnop-Weever, L. G. Hydroxide Complexes of Lanthanides—IV Ytterbium (III) in Perchlorate Medium. *Talanta* **1982**, *29* (3), 219–222.
(124) Lvanov-Emin, B. N.; Egorov, A. M.; Romanyuk, V. I.; Siforova, E. N. Formation Constants of Anion Hydroxo-Complexes of Elements of Group-III in Periodic System. *Russ. J. Inorg. Chem.* **1970**, *15*, 1224.
(125) López-González, H.; Jiménez-Reyes, M.; Solache-Ríos, M.; Rojas-Hernández, A. Solubility and Hydrolysis of Lutetium at Different [Lu3+] Initial. *J. Radioanal. Nucl. Chem.* **2007**, *274* (1), 103–108. https://doi.org/10.1007/s10967-006-6910-4.
(126) Zhan, C.-G.; Dixon, D. A. Absolute Hydration Free Energy of the Proton from First-Principles Electronic Structure Calculations. *J. Phys. Chem. A* **2001**, *105* (51), 11534–11540. https://doi.org/10.1021/jp012536s.
(127) Namazian, M.; Kalantary-Fotooh, F.; Noorbala, M. R.; Searles, D. J.; Coote, M. L. Møller–Plesset Perturbation Theory Calculations of the PKa Values for a Range of Carboxylic Acids. *J. Mol. Struct. THEOCHEM* **2006**, *758* (2), 275–278. https://doi.org/https://doi.org/10.1016/j.theochem.2005.10.024.
(128) Charif, I. E.; Mekelleche, S. M.; Villemin, D.; Mora-Diez, N. Correlation of Aqueous PKa Values of Carbon Acids with Theoretical Descriptors: A DFT Study. *J. Mol. Struct. THEOCHEM* **2007**, *818* (1), 1–6. https://doi.org/https://doi.org/10.1016/j.theochem.2007.04.037.
(129) Ho, J.; Coote, M. L. A Universal Approach for Continuum Solvent PKa Calculations: Are We There Yet? *Theor. Chem. Acc.* **2009**, *125* (1), 3. https://doi.org/10.1007/s00214-009-0667-0.
(130) Wander, M. C. F.; Rustad, J. R.; Casey, W. H. Influence of Explicit Hydration

Waters in Calculating the Hydrolysis Constants for Geochemically Relevant Metals. *J. Phys. Chem. A* **2010**, *114* (4), 1917–1925. https://doi.org/10.1021/jp908938p.

(131) Galstyan, G.; Knapp, E.-W. Computing PKA Values of Hexa-Aqua Transition Metal Complexes. *J. Comput. Chem.* **2015**, *36* (2), 69–78. https://doi.org/https://doi.org/10.1002/jcc.23764.

(132) Giard, A.; Filhol, J. S.; Jolibois, F.; Cavelier, F.; Berthomieu, D. Prediction of PKa Using DFT: The Nicotianamine Polyacid Example. *J. Chem. Theory Comput.* **2016**, *12* (11), 5493–5500. https://doi.org/10.1021/acs.jctc.6b00404.

(133) Yu, D.; Du, R.; Xiao, J.-C.; Xu, S.; Rong, C.; Liu, S. Theoretical Study of PKa Values for Trivalent Rare-Earth Metal Cations in Aqueous Solution. *J. Phys. Chem. A* **2018**, *122* (2), 700–707. https://doi.org/10.1021/acs.jpca.7b12074.

(134) Tomasi, J. Thirty Years of Continuum Solvation Chemistry: A Review, and Prospects for the near Future. *Theor. Chem. Acc.* **2004**, *112* (4), 184–203. https://doi.org/10.1007/s00214-004-0582-3.

(135) Cramer, C. J.; Truhlar, D. G. Implicit Solvation Models: Equilibria, Structure, Spectra, and Dynamics. *Chem. Rev.* **1999**, *99* (8), 2161–2200.

Supporting Information for Chapter 5

Table 5-S1. Ln^{III} electronic configuration and multiplicities

Ln^{III}	Electronic configuration	Multiplicity
La	$5s^25p^6$	1
Ce	$4f^1$	2
Pr	$4f^2$	3
Nd	$4f^3$	4
Pm	$4f^4$	5
Sm	$4f^5$	6
Eu	$4f^6$	7
Gd	$4f^7$	8
Tb	$4f^8$	7
Dy	$4f^9$	6
Ho	$4f^{10}$	5
Er	$4f^{11}$	4
Tm	$4f^{12}$	3
Yb	$4f^{13}$	2
Lu	$4f^{14}$	1

Discussion on vibrational frequencies in electronic structure calculations

It is difficult to identify the energy minimum of Ln^{III} aqua ions because they are highly flexible, fluxional species. For the thermodynamic integration, despite exhaustive geometry optimization calculations [M06 functional, Stuttgart RSC Segmented effective core potentials and corresponding basis sets for Ln^{III} ions, cc-PVTZ basis sets other atoms] few imaginary frequencies remained for some compounds. We chose to optimize geometries with small-core effective core potentials and corresponding basis sets, rather than using a less rigorous approach, without relativistic effects, and observe geometries no imaginary frequencies. All optimizations were taken to a point where the energy did not change significantly (>6 kJ/mol, ~pK_a unit at 298 K) which is within the accuracy of

density functional theory used to calculate pK_{a1} values from which pK_{a2} and pK_{a3} values are based on. All remaining imaginary frequencies are below 500 cm^{-1} (6 kJ/mol, 1.4 kcal/mol). Finally, the numerical Hessian was used, most errors (< ~150 cm^{-1}) are within numerical noise.

Discussion on basis sets with diffuse functions in geometry optimizations

We calculated pK_{a2} and pK_{a3} for La, Ce, Pr, Nd, Ho, Er, Lu using the ma-def2-TZVPP basis set in the optimizations. This resulted in pK_a values that are further from experiment (mean absolute deviations MAD values) than those reported in the manuscript (see Methods). The specific numbers are given in the table below.

Table 5-S2

Element	pK_{a2} MAD in manuscript	pK_{a2} MAD using ma-def2-TZVPP in optimization	pK_{a3} MAD in manuscript	pK_{a3} MAD using ma-def2-TZVPP in optimization
La	4.5	5.5 (did not improve)	7.1	8.6 (did not improve)
Ce	0.8	5.1 (did not improve)	5.3	5.9 (did not improve)
Pr	-	-	4.9	9.6 (did not improve)
Nd	3.8	4.0 (did not improve)	6.6	5.7 (improvement)
Ho	1.1	2.1 (did not improve)	3.9	2.7 (improvement)
Er	4.2	8.7 (did not improve)	6.8	5.8 (improvement)
Lu	1.2	2.3 (did not improve)	4.3	1.4 (improvement)

CHAPTER 6

The Effect of Lanthanum Ions on the Brønsted Acidity of Faujasite and Implications for Hydrothermal Stability

Richard C. Shiery, Stuart J. McElhany, David C. Cantu

Department of Chemical and Materials Engineering, University of Nevada, Reno

Modified from a manuscript that was published in *The Journal of Physical Chemistry C, 125, 13649 – 13657*, with the same title and authors

6.1. Introduction

Faujasite (FAU) has applications as a catalyst, molecular sieve, adsorbent, and ion exchanger. Faujasite, chiefly as zeolite Y with Si/Al ratios greater than 5, is the principal catalytic component in most fluid cracking catalysts, which operates under harsh heat and steam conditions, resulting in their destabilization by dealumination which most often begins in Brønsted acid sites.[1] As a result, the average lifetime of fluid catalytic cracking catalysts is one month and is a significant cost contributor in the production of gasoline.[2,3]

The presence of lanthanum, even in relatively small quantities, significantly improves the hydrothermal stability of fluid catalytic cracking catalysts, mainly by decreasing FAU dealumination.[4–7] The location, and atomic configuration, of rare earth elements in faujasite affects framework stability.[8] Lanthanum distributions in FAU are known[9], indicating lanthanum ions will adsorb in multiple FAU sites; however, the exact atomic configurations of lanthanum in FAU remains unclear; they are likely to vary by Si/Al ratio and conditions, since lanthanum, most commonly as ion in the +III state (La^{3+}), can undergo hydrolysis and form hydroxide species which react with each other.[10] Atomic configurations have been proposed, based both in experimental and computational results.[11,12]

Despite that much work has been done on lanthanides and FAU,[13] and that lanthanum will form coordination bonds with FAU,[12] the fundamental role of lanthanum in preventing dealumination remains poorly understood. A proposed mechanism is that lanthanum raises the activation energy of dealumination reactions in faujaiste.[14] Similarly, other cations have been proposed to hinder dealumination in other zeolites.[15]

Regardless of the mechanism by which lanthanum stabilizes faujasite, dealumination most likely happens by water-mediated mechanisms.[14–24] In this work, we discuss additional putative mechanisms based on how La^{3+} ions change the Brønsted acidity of faujasite.

Brønsted acid sites in zeolites reduce their hydrothermal stability since they attract water molecules to Al tetrahedra,[25–27] which can start dealumination reactions. Despite affecting zeolite hydrothermal stability,[28] Brønsted acid sites on zeolites are of great interest due to their catalytic activity in various reactions, not only for petroleum cracking.[11,29–41] Upon binding lanthanum, changes in the acid strength of the remaining zeolite Brønsted acid sites have been observed, increasing zeolite stability as well.[16,42,43]

Modeling lanthanum in faujasite, as well as proton transfer reactions (i.e., Brønsted acidity), requires considering the electronic structure because of forming/breaking La-O coordination bonds as well as O-H bonds. Further, due to the large conformational space that water molecules and La ions can occupy in faujasite, and the effects of temperature, sampling needs to be considered as well. Therefore, we employ density functional theory-based molecular dynamics simulations to identify the binding configurations of water and La^{3+} ions in faujasite. We use a rare event simulation technique to perform constrained *ab initio* molecular dynamics simulations and obtain potentials of mean force of proton transfer reactions in lanthanum-exchanged faujasite. In this work, we quantify how La^{3+} binding changes the acidity of faujasite Brønsted acid sites, and discuss its implications regarding the hydrothermal stability of faujasite.

6.2. Computational Methods

All density functional theory (DFT) calculations and *ab initio* molecular dynamics (AIMD) simulations were performed in mixed a Gaussian and plane wave approach with the CP2K[44,45] package, within the generalized gradient approximation using the PBE functional,[46] which has been tested for water[47,48] and lanthanides.[49,50] Core electrons were modeled with norm-conserving GTH pseudopotentials,[51] valence electrons were modelled with polarizable double-zeta basis sets.[52] For lanthanum, our LnPP1 pseudopotential and basis set was used.[53] Long range electrostatics were calculated using a supplementary plane wave basis set with a 500 Ry cutoff. To account for van der Waals interactions, Grimme's D3 corrections[54] were used with a 6.0 Å radius. We recently employed AIMD simulations, with our LnPP1 pseudopotential and basis sets,[53] to resolve the solution structure of all Ln^{3+} aqua ions,[55] and europium-ligand complexes,[56] with Ln^{3+}-O distances within ~0.05 Å of experiment.

6.2.1. Preparing faujasite model for simulation

The coordinates of all-silica FAU were obtained from the Database of Zeolite Structures,[57] and a rhombohedral cell was constructed, as done by Schüßler and co-workers,[12] to reduce the cell size (a=b=c: 17.6975 Å; α=β=γ: 60 degrees) and number of FAU atoms (144). Si tetrahedra were replaced with Al tetrahedra, using an Si/Al ratio of five, and a hydrogen atom was added in an oxygen atom binding each Al atom to neutralize the charge, resulting in hydrogen-exchanged faujasite with Si/Al=5 (H-FAU5). Protons were added preferably on the oxygen atoms of Al tetrahedra that form part of sodalite hexagonal windows, or that form part of the supercage for the Al tetrahedra that

are not in hexagonal windows, see additional discussion in the Supporting Information (SI). We optimized the cell coordinates and geometry in CP2K, as described above. We tested five random Al distributions in FAU, discarded those that violated Lowenstein's rule in periodic conditions, optimized the cell size and geometry for each Al distribution H-FAU-5 model independently, and chose the structure with the lowest energy, see **Figure 6-1**. The H-FAU-5 model with the energetically favored Al distribution has the resulting cell dimensions (a=b=c: 17.53 Å; α=β=γ: 60 degrees), contains eight Al-tetrahedra, eight H atoms, forty Si tetrahedra.

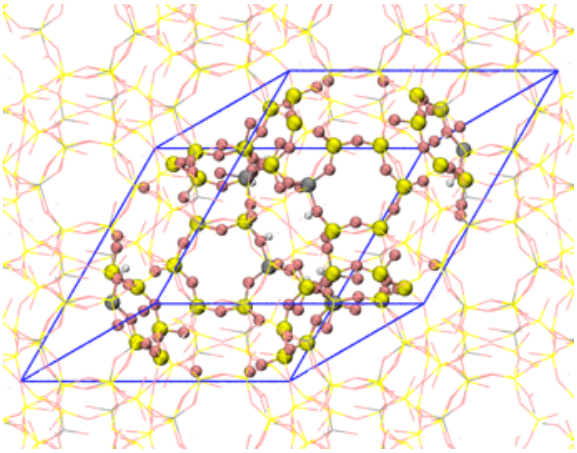

Figure 6-1: Rhombohedral cell of faujasite, only atoms in the unit cell show in ball-and-stick for clarity. Si (yellow), Al (gray), H (white), faujasite O atoms (pink).

6.2.2. Water binding energies

Starting from the optimized H-FAU-5 model (Section 6.2.1), the binding energies of water were determined through geometry optimizations of water molecules bound in the following FAU sites: hexagonal prism (S1), sodalite cage (S1'), hexagonal window of the super cage (S2), and square window of the super cage (S3). For each site, binding energies were quantified with water molecule(s) binding directly on the aluminum atom,

and independently on the hydroxyl group (-OH), see **Figure 6-2**. For each site (S1, S1', S2, S3) and FAU binding atom(s) (Al, OH), the binding energies of one to four water molecules were quantified, each water added sequentially forming hydrogen bonds with the previous water added. To quantify water binding energies on the Al atom, the position of the first water was constrained, because in unconstrained optimizations the first water molecule changed position to bind the -OH group. The binding energy of water was determined from the energy of water-bound FAU with respect to FAU without water and a single gas phase water molecule in the same periodic box size, and calculated with:

$$Binding\ Energy\ of\ Water\ (BE_{\mathrm{WAT}}) = E[\mathrm{FAU} + (\mathrm{H_2O})_n] - E[\mathrm{FAU}] - n \cdot E[\mathrm{H_2O}] \quad (6.1)$$

For each site (S1, S1', S2, S3) and FAU binding atom(s) (Al, OH), the energy (E) of each species in **equation 6.1** was obtained with DFT calculations as described above and independent geometry optimizations. The initial water binding position in the Al tetrahedra depends on which FAU site the water binding energies are being calculated.

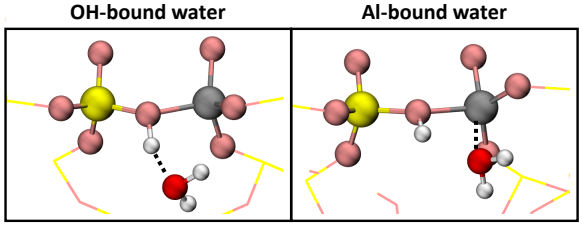

Figure 6-2: In each FAU site, water binding energies were independently calculated bound to the -OH group (**left**) and the -Al- atom (**right**). Only relevant atoms shown in ball-and-stick for clarity. Si (yellow), Al (gray), H (white), faujasite O atoms (pink), water O atoms (red).

6.2.3. Lanthanum ion binding energies

Starting from the optimized H-FAU-5 model, a $[La\cdot(H_2O)_9]^{3+}$ ion was placed in middle of the supercage, and three protons (H^+) removed to maintain a neutral simulation box (La-H-FAU-5); five protons remained because our model structure has eight Al-tetrahedra (Section 6.2.1). The position of La^{3+} was constrained in the middle of the supercage (S4) and the geometry of FAU with $[La\cdot(H_2O)_9]^{3+}$ in the S4 site optimized to determine the energy of the reference point, see **Figure 6-3**. The water molecules, which were unconstrained, remained coordinated to the lanthanum ion in the optimization. In other FAU sites, in which the La^{3+} ion directly coordinates to FAU, water molecules originally coordinated to the La^{3+} ion are replaced with O_{FAU} atoms, the displaced water molecules were placed in the simulation box, so to contain the same number of atoms and be able to compare energies. Due to the large conformational space, we determined the energy of La^{3+} bound to other FAU sites using AIMD simulations with the following protocol: (i) an initial geometry optimization, (ii) followed by 2 ps of AIMD simulation in the NVT ensemble at high temperature (1000 K), this was followed by (iii) annealing to 0K over 4ps of AIMD simulation in the NVE ensemble, and lastly (iv) a final geometry optimization. Although this protocol does not guarantee a global minimum, it identifies the minimum in a large conformational space sampled during the high temperature AIMD. The high temperature simulation also ensures that La^{3+} finds the energetically favored conformation in each site. The coordinates of La^{3+} were not constrained during the high temperature AIMD, simulated annealing, nor final optimization.

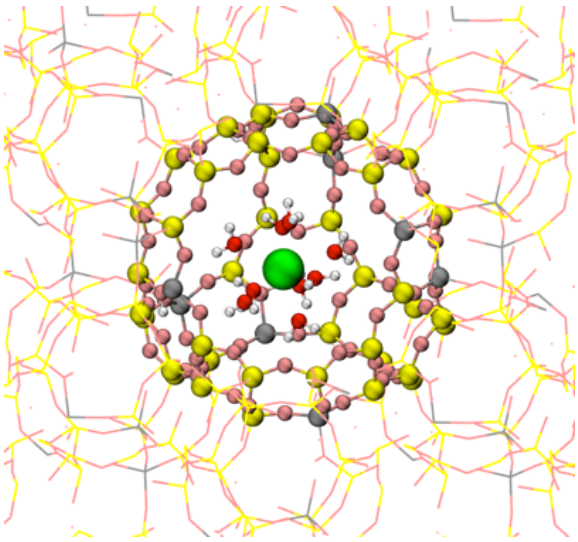

Figure 6-3: $[La\cdot(H_2O)_9]^{3+}$ in FAU in the middle of the supercage (S4 site). Only large pore and $[La\cdot(H_2O)_9]^{3+}$ atoms shown in ball-and-stick for clarity. Si (yellow), Al (gray), H (white), faujasite O atoms (pink), water O atoms (red), La (green).

The molecular conformations of single lanthanum ions (La^{3+}) in FAU were independently determined in sites were La^{3+} ions are known[9] to bind: the hexagonal prism, (S1) sodalite cage (S1'), the hexagonal window of the super cage (S2), the square window of the super cage (S3), the middle of the supercage (S4), and in the window between two supercages (S5). Since La^{3+} ions are nine-coordinate in water, the starting conformation of La^{3+} in each site was set to be a nine-coordinate species, with La^{3+} forming coordination bonds with faujasite oxygen atoms (O_{FAU}) and coordination bonds with water oxygen atoms (O_{WAT}) with water molecules coordinated on La^{3+} sites not bound to FAU. Nine water molecules were present in all La^{3+}/FAU calculations and simulations, water molecules not directly coordinating La^{3+} ion were placed in other FAU locations. To determine which site is energetically favored for La^{3+} ions to bind, we calculated the binding energy of La^{3+} ions on each site using the energy of $[La\cdot(H_2O)_9]^{3+}$

in the middle of the supercage (S4) as the reference point to calculate binding energies on each site.

$$Binding\ energy\ of\ \mathrm{La^{3+}}(BE_{\mathrm{La}}) = E[\mathrm{La^{3+}}\ in\ \mathrm{FAU}\ site] - E[\mathrm{La^{3+}}\ in\ \mathrm{FAU}\ S4] \quad (6.2)$$

6.2.4. Quantification of Brønsted acidity

To quantify Brønsted acidity, we calculated free energies of proton transfer ($\Delta \boldsymbol{F}_{\mathbf{prot}}$) from potentials of mean force of proton transfer obtained from constrained Bluemoon[58,59] AIMD simulations. To quantify how bound $[La\cdot(H_2O)_n]^{3+}$ ions affect the acidity of FAU (Section 6.3.2), potentials of mean force were obtained for the following cases. Case 1: A proton from the -OH group in an Al tetrahedron adjacent to a sodalite-bound $[La\cdot(H_2O)_n]^{3+}$ ion was transferred to a water molecule. Case 2: The same potential of mean force as Case 1 was obtained without the $[La\cdot(H_2O)_n]^{3+}$ ion as a reference curve to Case 1. Case 3: A proton from the -OH group in an Al tetrahedron *not* adjacent to a sodalite-bound $[La\cdot(H_2O)_n]^{3+}$ ion was transferred to a water molecule. Case 4: The same potential of mean force as Case 3 was obtained but without the $[La\cdot(H_2O)_n]^{3+}$ ion as a reference curve to Case 3.

For each case, we pulled a proton from a water molecule to a neighboring water molecule in 0.05 Å increments, along O-H bond distances ($\boldsymbol{r}_{\mathbf{O\text{-}H}}$) ranging from ~1.00 Å to ~1.40 Å. Our reaction coordinate ($\boldsymbol{r}_{\mathbf{O\text{-}H}}$), or collective variable, has been found to be an adequate constraint to describe Brønsted in inorganic compounds.[60] Potentials of mean force of proton transfer from Bluemoon ensemble AIMD simulations are an accurate way

to quantify Brønsted acidity,[61–63] and this approach has been employed on oxide surfaces,[64] organic compounds,[65–69] and transition metal complexes.[60]

For each case, nine independent AIMD simulation boxes, with varying O-H distances ($\boldsymbol{r_{O\text{-}H}}$), were generated. For each AIMD simulation box, $\boldsymbol{r_{O\text{-}H}}$ was constrained, and 15 ps of NVT (T=298 K) simulation were performed with 1 fs time steps. The forces on the constraint (SHAKE Lagragian multipliers) were averaged over the last 10 ps (5 to 15 ps) of NVT simulation, to generate an average force on the constraint ($\boldsymbol{r_{O\text{-}H}}$). An integration of the forces on the constraint over $\boldsymbol{r_{O\text{-}H}}$ was done to obtain potentials of mean force, i.e., free energy profile. Helmholtz free energies are obtained from the potentials of mean force, and $\Delta\boldsymbol{F_{prot}}$ values can be calculated as the difference in free energy between unprotonated and protonated states.

$$\Delta F_{\text{prot}} = F_{unprotonated} - F_{protonated} \quad (6.3)$$

To estimate the error in $\Delta\boldsymbol{F_{prot}}$ values, we took the absolute difference between $\Delta\boldsymbol{F_{prot}}$ values calculated with the first half of equilibrated trajectory (5 to 10 ps) with those calculated with second half (10 to 15 ps) of the equilibrated trajectory.

6.3. Results and Discussion

6.3.1. Sodalite is the energetically favored binding site for water and lanthanum ions

The binding energies of water are reported in **Table 6-1**. The two main findings are that it is energetically favored for water molecule(s) to bind the hydroxyl group rather than the

Al atom in all FAU sites (S1, S1', S2, S3); and that the sodalite cage is the energetically preferred binding site for water molecule(s).

Table 6-1: Water binding energies in hydrogen-exchanged faujasite with an Si/Al ratio of 5.

	Binding Energies of Water BE_{WAT} (kJ/mol)							
	1st Water Molecule		2nd Water Molecule		3rd Water Molecule		4th Water Molecule	
Site/Bound to	Al	OH	Al	OH	Al	OH	Al	OH
S1 (hexagonal prism)	14	-35	26	15	47	51	-	-
S1' (sodalite cage)	32	-82	-14	-85	-24	-85	-37	-84
S2 (supercage, hexagonal window)	4	-84	-40	-85	-46	-79	-45	-78
S3 (supercage, square window)	30	-81	-18	-55	-17	-65	-24	-50

For single water molecules, favorable binding energies are observed in hydroxyl groups of all sites, with similar magnitudes for the sodalite cage and supercage binding sites. As the number of water molecules increases, hydroxyl group binding energies favor the sodalite cage over the supercage, while remaining energetically favorable for both cages. **Figure 6-4** shows how water molecules bind on the OH-group in the sodalite cage. Repulsive energies are found for additional water molecules in the hexagonal prism hydroxyl site, in which space allows for up to three water molecules.

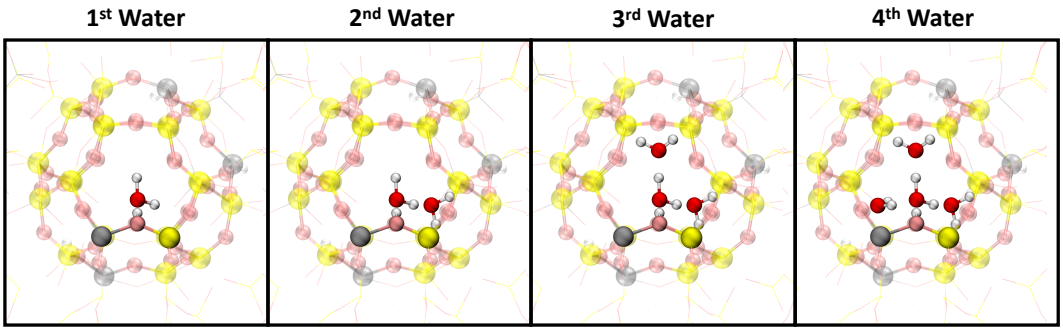

Figure 6-4: Water binding on the OH-group in a FAU sodalite cage. Only relevant atoms shown in ball-and-stick, and some transparent, for clarity. Si (yellow), Al (gray), H (white), faujasite O atoms (pink), water O atoms (red).

On Al atoms, repulsive energies are found for single water molecules in all sites. Additional water molecules, which are hydrogen-bound to the first Al-bound water molecule, are energetically favored to bind, with the exception of the hexagonal prism. However, for all sites and number of water molecules, binding to the hydroxyl group is energetically favored over the Al atom. Excluding the hexagonal prism, water binding energies for hydroxyl group increased slightly as more water is added, while water binding energies for the Al tetrahedron decreased or remained similar in magnitude.

Studies with SSZ,[19] LTA[15] and ZSM[24] zeolites also observed that water is energetically favored to bind on the OH-group over the Al atom in Brønsted acid sites. This is relevant to the hydrothermal stability of faujasite since water placement has been shown to affect dealumination mechanisms and energetics in zeolites SSZ,[19] LTA[15] and ZSM.[24]

Table 6-2 includes the binding energies of complexed $La{\cdot}(H_2O)_n^{3+}$ ions in FAU, and are reported as relative to the energy of $La{\cdot}(H_2O)_9^{3+}$ in the S4 site. We found that La^{3+} ions will energetically favor binding in the sodalite cage. Binding energies for the remaining sites are much lower in magnitude than that for S1', however, still preferred over the S4 site.

Table 6-2: Energetics of La3+ binding in FAU sites.

Site	Binding Energy of La^{3+} BE_{La} (kJ/mol)
S1 (hexagonal prism)	-241
S1' (sodalite cage)	-314
S2 (supercage, hexagonal window)	-74
S3 (supercage, square window)	-259
S4 (middle of supercage)	0
S5 (window between two supercages)	-240

$La{\cdot}(H_2O)_n^{3+}$ ions in the sodalite cage have a coordination number of seven, with five O_{FAU} atoms forming coordination bonds with the La^{3+} ion along with two water molecules directly coordinated, **Figure 6-5**. A third water molecule remains in the sodalite cage which forms hydrogen bonds with both La^{3+}-coordinated water molecules. This La^{3+} binding conformation, identified through annealing AIMD simulations, is in qualitative agreement with previous studies that report La^{3+} ion binding in the sodalite cage.[9,11,12,14,42]

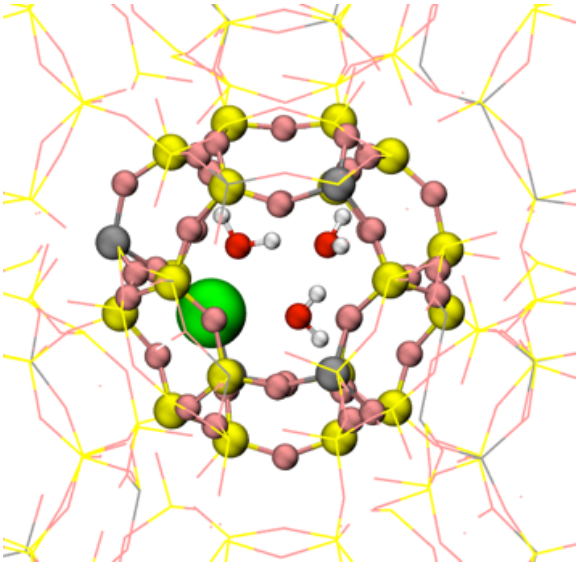

Figure 6-5: $[La{\cdot}(H_2O)_n]^{3+}$ in the S1' site in FAU in. Only sodalite and $[La{\cdot}(H_2O)_n]^{3+}$ atoms shown in ball-and-stick for clarity. Si (yellow), Al (gray), H (white), faujasite O atoms (pink), water O atoms (red), La (green).

Recent studies propose that cations increase zeolite hydrothermal stability by heightening dealumination energy barriers: (i) Louwen et al., showed that La^{3+} ions increase dealumination energy barriers in faujasite,[14] and (ii) Sun et al., showed that alkali and alkaline earth cations increase dealumination barriers in LTA.[15] In addition to mechanisms by which La^{3+} increases dealumination energy barriers, we hypothesize, that, La^{3+} ions may stabilize faujasite by competing with water molecules for sodalite

binding sites, since both water molecules and La^{3+} ions are energetically favored to bind in sodalite cages. Proposed zeolite dealumination mechanisms explicitly involve water molecules.[14–24] Therefore, La^{3+} ions in sodalite, by occupying preferred water binding sites, may slow faujasite dealumination by inhibiting the access of water molecules to Al tetrahedra.

6.3.2. La^{3+} ions increase the acidity of Brønsted acid sites in faujasite

Figures 6-6 and **6-7** show potentials of mean force that describe how $[La\cdot(H_2O)_n]^{3+}$ ions bound in sodalite affect the Brønsted acidity of FAU. In **Figure 6-6**, we compare the Brønsted acidity of an Al tetrahedra (i.e., -Al-OH-Si-) adjacent to the La^{3+}-bound sodalite, with (Case 1) and without (Case 2) La^{3+} bound to FAU. In **Figure 6-7**, we compare the Brønsted acidity of an Al tetrahedra *not* adjacent to the La^{3+}-bound sodalite, with (Case 3) and without (Case 4) La^{3+} bound to FAU, see descriptions in Section 6.2.4. We found that La^{3+} ions make FAU Brønsted sites more acidic, with significant changes in the free energy profiles due to the inclusion of La^{3+} ions, with a more pronounced effect for Brønsted sites adjacent to the La^{3+} binding site.

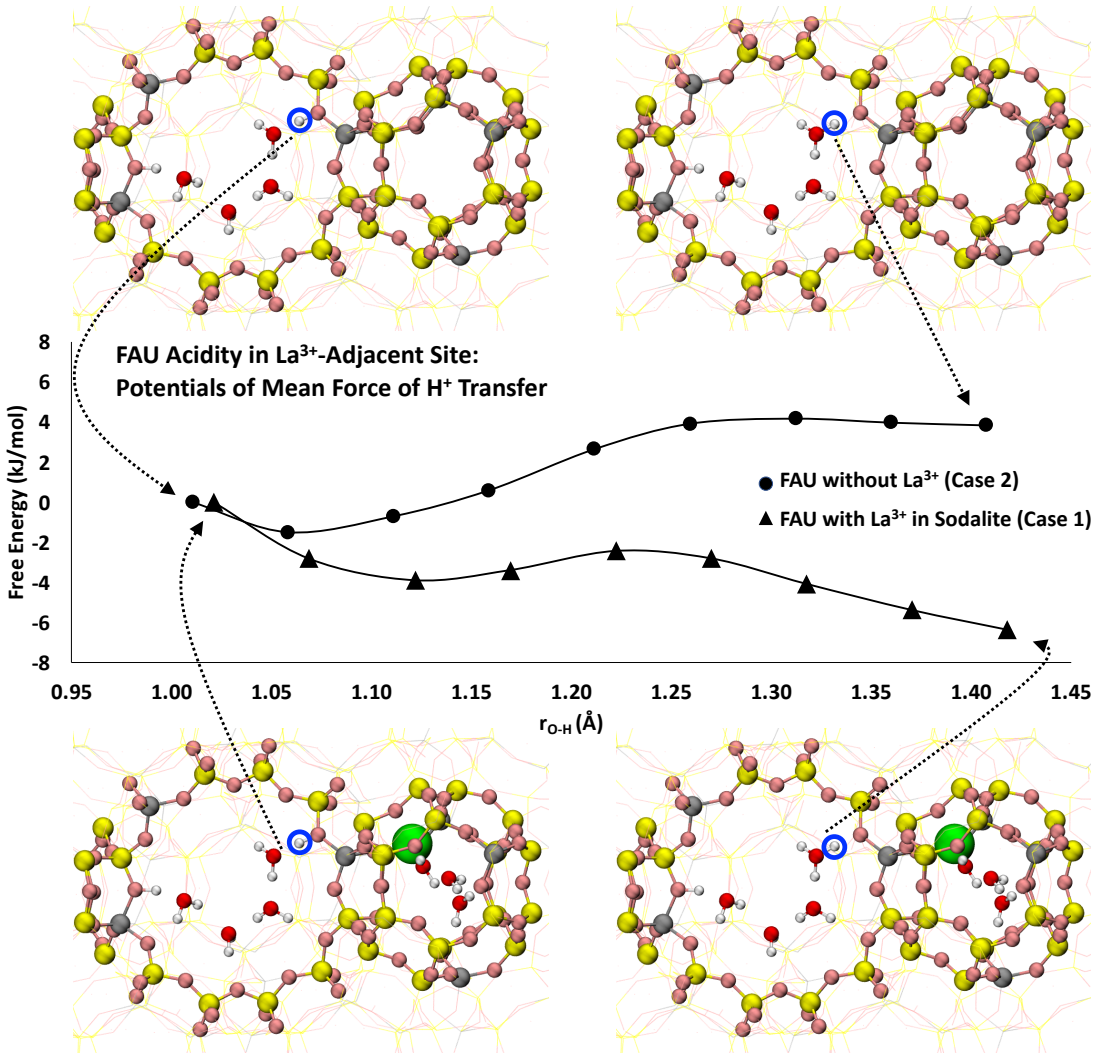

Figure 6-6: Potentials of mean force of proton transfer from a FAU acid site to a neighboring water molecule, for FAU without La^{3+} (**circles, top**) and for FAU with La^{3+} bound in sodalite adjacent to the Al tetrahedra with the Brønsted acid site (**triangles, bottom**). Only cage, water molecules, and $[La{\cdot}(H_2O)_n]^{3+}$ atoms shown in ball-and-stick for clarity. Si (yellow), Al (gray), H (white), faujasite O atoms (pink), water O atoms (red), La (green). The transferred proton is circled in blue.

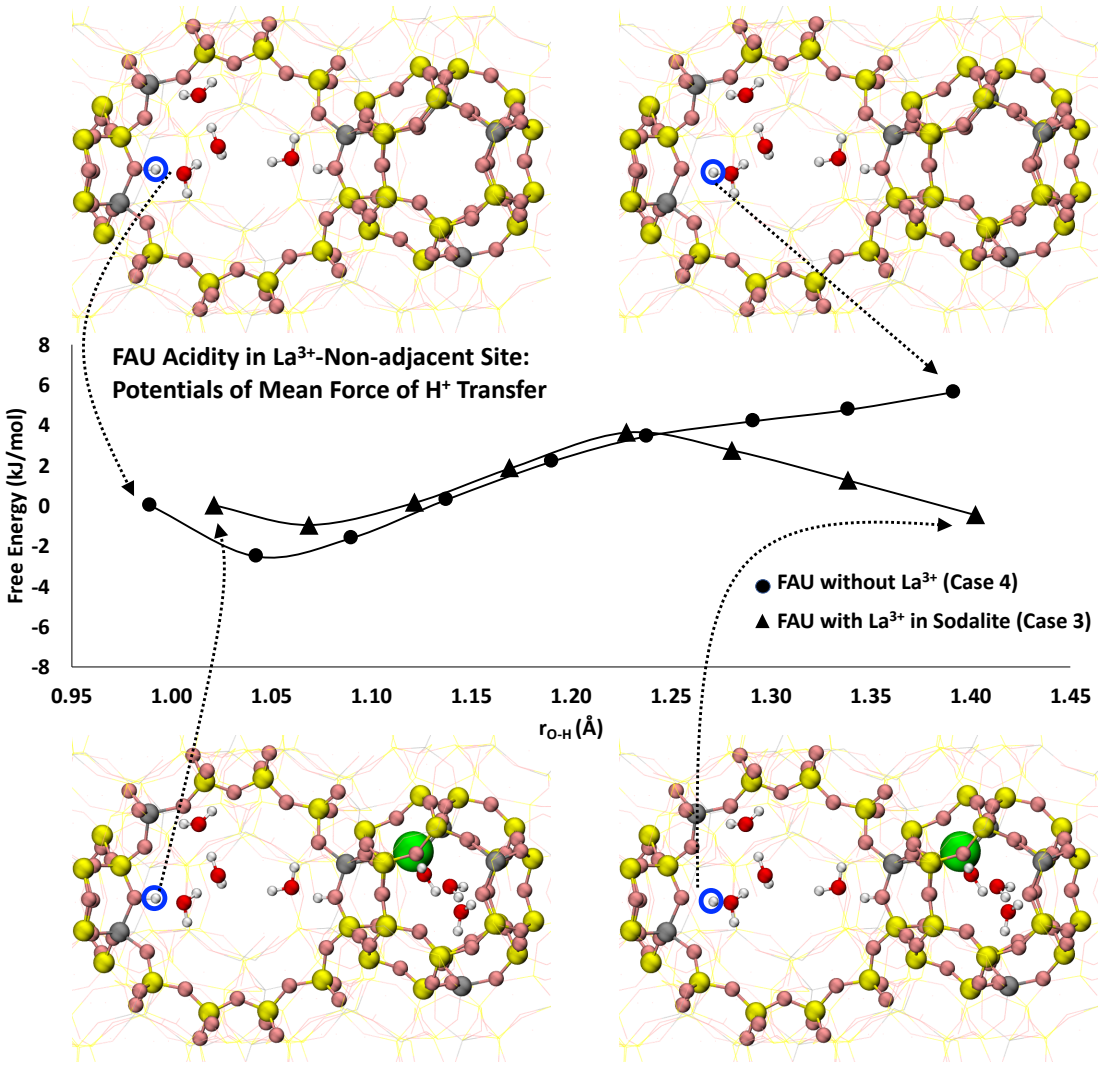

Figure 6-7: Potentials of mean force of proton transfer from a FAU acid site to a neighboring water molecule, for FAU without La^{3+} (**circles, top**) and for FAU with La^{3+} bound in sodalite *not* adjacent to the Al tetrahedra with the Brønsted acid site (**triangles, bottom**). Only cage, water molecules, and $[La{\cdot}(H_2O)_n]^{3+}$ atoms shown in ball-and-stick for clarity. Si (yellow), Al (gray), H (white), faujasite O atoms (pink), water O atoms (red), La (green). The transferred proton is circled in blue.

For the La^{3+}-adjacent Brønsted acid sites (**Figure 6-6**), the free energies of proton transfer ($\Delta \boldsymbol{F}_{\mathbf{prot}}$) changed from 4 ±1 kJ/mol without a La^{3+} ion in FAU to -6 ±3 kJ/mol with a La^{3+} ion in FAU: most noteworthy, a sign change is observed, meaning that, for La^{3+}-adjacent sites, the proton on FAU Brønsted acid sites will not remain in FAU, but

rather it is energetically favorable for it to readily form H_3O^+ species with water molecules. The change is less pronounced for FAU Brønsted acid sites not adjacent to a FAU-bound La^{3+} ion (**Figure 6-7**): $\Delta \boldsymbol{F}_{\mathbf{prot}}$ values changed less than for the adjacent site, from 6 ±2 kJ/mol without a La^{3+} ion in FAU to 0 ±3 kJ/mol with a La^{3+} ion in FAU. However, still a meaningful change is observed, because, when La^{3+} binds FAU, Al tetrahedra will become more acidic, even for sites not adjacent to the sodalite-bound La^{3+} ion. The small margins of error in $\Delta \boldsymbol{F}_{\mathbf{prot}}$ values show that sufficient sampling was obtained in the AIMD simulations.

Both potentials of mean force without La^{3+} in FAU (circles in **Figures 6-6** and **6-7**) show similar FAU acidity, and that the protons on FAU Brønsted acid sites have an energetically preferred O-H distance of ~1.05 Å. The small energy difference between protonated and unprotonated states of Brønsted acid sites suggest that H_3O^+ species will form, in agreement with previous experimental and computational studies.[27,70–74] The potential of mean force for the La^{3+} adjacent site (triangles in **Figure 6-6**) show proton dissociation from Al tetrahedra, and is a clear indication of increased Brønsted acidity due to the presence of La^{3+} ions. The potential of mean force for the site *not* adjacent to La^{3+} (triangles in **Figure 6-7**) shows that the protonated and unprotonated states of the Brønsted acid site are isoenergetic, and that between states (i.e., a proton not bound to FAU nor H_3O^+) is energetically unfavorable.

The increase of Brønsted acidity in La-exchanged faujasite (La-H-FAU) compared to hydrogen-exchanged faujasite (H-FAU) is consistent with experimental results indicative of fewer acid sites with greater acid strength upon lanthanum adsorption.[42] Zeolites with mostly Si tetrahedra are hydrophobic,[75–78] however those with

an increased number of Al tetrahedra are hydrophilic, with water sorption near Brønsted acidic sites.[26,27] Further, Prodinger et al., found that the concentration of Al tetrahedra plays an important role to determine water concentrations in zeolites and their stability.[25] Also, the proton on Brønsted acid sites has been proposed to start dealumination in faujasite.[28] To test the effect of deprotonation on the hydrophilicity of Al tetrahedra, we calculated the binding energy of a water molecule on the Al tetrahedra that undergo proton transfer in **Figures 6-6** and **6-7**; in their unprotonated state (La^{3+}-bound FAU), and their protonated state (without La^{3+} ion binding in FAU). We found that, upon La^{3+}-induced deprotonation, the binding energy of a water molecule changed from -85 kJ/mol to -37 kJ/mol on the La^{3+}-adjacent Al tetrahedron, and changed from -85 kJ/mol to -44 kJ/mol on the non-adjacent Al tetrahedron, which makes water less energetically favorable to bind by 56% and 48% for the La^{3+}-adjacent and non-adjacent Al tetrahedral sites, respectively. Therefore, we hypothesize that increased Brønsted acidity is another mechanism by which La^{3+} ions increase the hydrothermal stability of faujasite: La^{3+} ions decrease the hydrophilicity of Al tetrahedra by making the Al tetrahedra more likely to be in the unprotonated state, which makes water-mediated dealumination mechanisms less likely to occur.

6.4. Conclusions

From our study, two conclusions are made regarding La^{3+} ions in faujasite and Brønsted acidity: (i) La^{3+} ions and water molecules prefer binding in the sodalite cage; and (ii) La^{3+} ions make Brønsted acid sites more acidic even for those not adjacent to the FAU-bound La^{3+} ions. These have implications on understanding how La^{3+} ions stabilize faujasite.

Cations, including La^{3+}, have been proposed to increase the hydrothermal stability of zeolites by raising the energetic barriers of dealumination.[14,15] Based on our conclusions, and that dealumination occurs via water-mediated mechanisms,[14–24] we propose that, in addition to raising dealumination energy barriers, La^{3+} ions stabilizes faujasite in two other ways. First, La^{3+} ions impede water molecules from binding in La^{3+}-occupied sodalite cages, therefore preventing water molecules from interacting with Al tetrahedra coordinated to La^{3+} ions. Second, by increasing the acidity of Brønsted acid sites, Al tetrahedra become deprotonated which reduces their hydrophilicity, especially since water molecules prefer to bind on the OH groups, which makes water molecules less likely to interact with Al tetrahedra and start water-mediated dealumination reactions.

Chapter 6 References

(1) Kühl, G. H. The Coordination of Aluminum and Silicon in Zeolites as Studied by X-Ray Spectrometry. *J. Phys. Chem. Solids* **1977**, *38*, 1259–1263.

(2) Vogt, E. T. C.; Weckhuysen, B. M. Fluid Catalytic Cracking: Recent Developments on the Grand Old Lady of Zeolite Catalysis. *Chem. Soc. Rev.* **2015**, *44*, 7342–7370.

(3) Cerqueira, H. S.; Caeiro, G.; Costa, L.; Ramôa Ribeiro, F. Deactivation of FCC Catalysts. *J. Mol. Catal. A Chem.* **2008**, *292*, 1–13.

(4) Woltermann, G. M.; Magee, J. S.; Griffith, S. D. Chapter 4 Commercial Preparation and Characterization of FCC Catalysts. In *Fluid Catalytic Cracking: Science and Technology*; Magee, J. S., Mitchell, M. M., Eds.; Elsevier, 1993; Vol. 76, pp 105–144.

(5) Akah, A. Application of Rare Earths in Fluid Catalytic Cracking: A Review. *J. Rare Earths* **2017**, *35*, 941–956.

(6) Zhang, L.; Qin, Y.; Zhang, X.; Gao, X.; Song, L. Further Findings on the Stabilization Mechanism among Modified y Zeolite with Different Rare Earth Ions. *Ind. Eng. Chem. Res.* **2019**, *58*, 14016–14025.

(7) Roelofsen, W.; Mathies, H.; De Groot, R. L.; Van Woerkom, P. C. M.; Angad Gaur, H. Effect of Rare Earth Loading in Y-Zeolite on Its Dealumination during Thermal Treatment. In *Studies in Surface Science and Catalysis*; Elsevier Inc., 1986; Vol. 28, pp 337–344.

(8) Du, X.; Gao, X.; Zhang, H.; Li, X.; Liu, P. Effect of Cation Location on the Hydrothermal Stability of Rare Earth-Exchanged y Zeolites. *Catal. Commun.* **2013**, *35*, 17–22.

(9) Frising, T.; Leflaive, P. Extraframework Cation Distributions in X and Y Faujasite Zeolites: A Review. *Microporous Mesoporous Mater.* **2008**, *114*, 27–63.

(10) Housecroft, C. E.; Sharpe, A. G. *Inorganic Chemistry*, Second.; Pearson Education Limited, 2005.

(11) Noda, T.; Suzuki, K.; Katada, N.; Niwa, M. Combined Study of IRMS-TPD Measurement and DFT Calculation on Brønsted Acidity and Catalytic Cracking Activity of Cation-Exchanged Y Zeolites. *J. Catal.* **2008**, *259*, 203–210.

(12) Schüßler, F.; Pidko, E. A.; Kolvenbach, R.; Sievers, C.; Hensen, E. J. M.; van Santen, R. A.; Lercher, J. A. Nature and Location of Cationic Lanthanum Species in High Alumina Containing Faujasite Type Zeolites. *J. Phys. Chem. C* **2011**, *115*, 21763–21776.

(13) Sousa-Aguiar, E. F.; Trigueiro, F. E.; Zotin, F. M. Z. The Role of Rare Earth Elements in Zeolites and Cracking Catalysts. *Catal. Today* **2013**, *218–219*, 115–122.

(14) Louwen, J. N.; Simko, S.; Stanciakova, K.; Bulo, R. E.; Weckhuysen, B. M.; Vogt, E. T. C. Role of Rare Earth Ions in the Prevention of Dealumination of Zeolite Y for Fluid Cracking Catalysts. *J. Phys. Chem. C* **2020**, *124*, 4626–4636.

(15) Sun, J.; Fang, H.; Ravikovitch, P. I.; Sholl, D. S. Understanding Dealumination Mechanisms in Protonic and Cationic Zeolites. *J. Phys. Chem. C* **2020**, *124*, 668–676.

(16) Yu, S.; Yan, J.; Lin, W.; Long, J.; Liu, S. Bin. Effects of Lanthanum Incorporation on Stability, Acidity and Catalytic Performance of Y Zeolites. *Catal. Letters* **2021**, *151*, 698–712.
(17) Agostini, G.; Lamberti, C.; Palin, L.; Milanesio, M.; Danilina, N.; Xu, B.; Janousch, M.; van Bokhoven, J. A. In Situ XAS and XRPD Parametric Rietveld Refinement To Understand Dealumination of Y Zeolite Catalyst. *J. Am. Chem. Soc.* **2010**, *132*, 667–678.
(18) Malola, S.; Svelle, S.; Bleken, F. L.; Swang, O. Detailed Reaction Paths for Zeolite Dealumination and Desilication From Density Functional Calculations. *Angew. Chemie Int. Ed.* **2012**, *51*, 652–655.
(19) Fjermestad, T.; Svelle, S.; Swang, O. Mechanistic Comparison of the Dealumination in SSZ-13 and the Desilication in SAPO-34. *J. Phys. Chem. C* **2013**, *117*, 13442–13451.
(20) Nielsen, M.; Brogaard, R. Y.; Falsig, H.; Beato, P.; Swang, O.; Svelle, S. Kinetics of Zeolite Dealumination: Insights from H-SSZ-13. *ACS Catal.* **2015**, *5*, 7131–7139.
(21) Silaghi, M.-C.; Chizallet, C.; Petracovschi, E.; Kerber, T.; Sauer, J.; Raybaud, P. Regioselectivity of Al–O Bond Hydrolysis during Zeolites Dealumination Unified by Brønsted–Evans–Polanyi Relationship. *ACS Catal.* **2015**, *5*, 11–15.
(22) Silaghi, M.-C.; Chizallet, C.; Sauer, J.; Raybaud, P. Dealumination Mechanisms of Zeolites and Extra-Framework Aluminum Confinement. *J. Catal.* **2016**, *339*, 242–255.
(23) Nielsen, M.; Hafreager, A.; Brogaard, R. Y.; De Wispelaere, K.; Falsig, H.; Beato, P.; Van Speybroeck, V.; Svelle, S. Collective Action of Water Molecules in Zeolite Dealumination. *Catal. Sci. Technol.* **2019**, *9*, 3721–3725.
(24) Stanciakova, K.; Ensing, B.; Göltl, F.; Bulo, R. E.; Weckhuysen, B. M. Cooperative Role of Water Molecules during the Initial Stage of Water-Induced Zeolite Dealumination. *ACS Catal.* **2019**, *9*, 5119–5135.
(25) Prodinger, S.; Shi, H.; Eckstein, S.; Hu, J. Z.; Olarte, M. V; Camaioni, D. M.; Derewinski, M. A.; Lercher, J. A. Stability of Zeolites in Aqueous Phase Reactions. *Chem. Mater.* **2017**, *29*, 7255–7262.
(26) Eckstein, S.; Hintermeier, P. H.; Zhao, R.; Baráth, E.; Shi, H.; Liu, Y.; Lercher, J. A. Influence of Hydronium Ions in Zeolites on Sorption. *Angew. Chemie Int. Ed.* **2019**, *58*, 3450–3455.
(27) Wang, M.; Jaegers, N. R.; Lee, M.-S.; Wan, C.; Hu, J. Z.; Shi, H.; Mei, D.; Burton, S. D.; Camaioni, D. M.; Gutiérrez, O. Y.; et al. Genesis and Stability of Hydronium Ions in Zeolite Channels. *J. Am. Chem. Soc.* **2019**, *141*, 3444–3455.
(28) Kim, J. T.; Kim, M. C.; Okamoto, Y.; Imanaka, T. Acid Attack Theory of Dealumination in Cation-Exchanged Faujasite. *J. Catal.* **1989**, *115*, 319–325.
(29) Xu, T.; Munson, E. J.; Haw, J. F. Toward a Systematic Chemistry of Organic Reactions in Zeolites: In Situ NMR Studies of Ketones. *J. Am. Chem. Soc.* **1994**, *116*, 1962–1972.
(30) Arora, S. S.; Nieskens, D. L. S.; Malek, A.; Bhan, A. Lifetime Improvement in Methanol-to-Olefins Catalysis over Chabazite Materials by High-Pressure H2 Co-Feeds. *Nat. Catal.* **2018**, *1*, 666–672.

(31) Koehle, M.; Zhang, Z.; Goulas, K. A.; Caratzoulas, S.; Vlachos, D. G.; Lobo, R. F. Acylation of Methylfuran with Brønsted and Lewis Acid Zeolites. *Appl. Catal. A Gen.* **2018**, *564*, 90–101.
(32) Ravi, M.; Sushkevich, V. L.; Knorpp, A. J.; Newton, M. A.; Palagin, D.; Pinar, A. B.; Ranocchiari, M.; van Bokhoven, J. A. Misconceptions and Challenges in Methane-to-Methanol over Transition-Metal-Exchanged Zeolites. *Nat. Catal.* **2019**, *2*, 485–494.
(33) Li, S.; Zheng, A.; Su, Y.; Zhang, H.; Chen, L.; Yang, J.; Ye, C.; Deng, F. Brønsted/Lewis Acid Synergy in Dealuminated HY Zeolite: A Combined Solid-State NMR and Theoretical Calculation Study. *J. Am. Chem. Soc.* **2007**, *129*, 11161–11171.
(34) Haag, W. O. Catalysis by Zeolites – Science and Technology. In *Zeolites and Related Microporous Materials: State of the Art 1994 - Proceedings of the 10th International Zeolite Conference, Garmisch-Partenkirchen, Germany, 17-22 July 1994*; Weitkamp, J., Karge, H. G., Pfeifer, H., Hölderich, W. B. T., Eds.; Elsevier, 1994; Vol. 84, pp 1375–1394.
(35) Lercher, J. A.; van Santen, R. A.; Vinek, H. Carbonium Ion Formation in Zeolite Catalysis. *Catal. Letters* **1994**, *27*, 91–96.
(36) Corma, A. Inorganic Solid Acids and Their Use in Acid-Catalyzed Hydrocarbon Reactions. *Chem. Rev.* **1995**, *95*, 559–614.
(37) Gounder, R.; Iglesia, E. The Catalytic Diversity of Zeolites: Confinement and Solvation Effects within Voids of Molecular Dimensions. *Chem. Commun.* **2013**, *49*, 3491–3509.
(38) Hemelsoet, K.; Van der Mynsbrugge, J.; De Wispelaere, K.; Waroquier, M.; Van Speybroeck, V. Unraveling the Reaction Mechanisms Governing Methanol-to-Olefins Catalysis by Theory and Experiment. *ChemPhysChem* **2013**, *14*, 1526–1545.
(39) Bui, L.; Luo, H.; Gunther, W. R.; Román-Leshkov, Y. Domino Reaction Catalyzed by Zeolites with Brønsted and Lewis Acid Sites for the Production of γ-Valerolactone from Furfural. *Angew. Chemie* **2013**, *125*, 8180–8183.
(40) Primo, A.; Garcia, H. Zeolites as Catalysts in Oil Refining. *Chem. Soc. Rev.* **2014**, *43*, 7548–7561.
(41) Göltl, F.; Michel, C.; Andrikopoulos, P. C.; Love, A. M.; Hafner, J.; Hermans, I.; Sautet, P. Computationally Exploring Confinement Effects in the Methane-to-Methanol Conversion Over Iron-Oxo Centers in Zeolites. *ACS Catal.* **2016**, *6*, 8404–8409.
(42) Deng, C.; Zhang, J.; Dong, L.; Huang, M.; Li, B.; Jin, G.; Gao, J.; Zhang, F.; Fan, M.; Zhang, L.; et al. The Effect of Positioning Cations on Acidity and Stability of the Framework Structure of y Zeolite. *Sci. Rep.* **2016**, *6*, 1–13.
(43) Vu, X. H.; Marschall, M. S.; Tran, V. T.; Ngo, T. P.; Dang, T. T.; Dinh, D. M.; Dao, T. K. T.; Busse, O.; Weigand, J. J. Enhanced Thermal Stability of Hierarchical Y Zeolites Obtained by Acid and Subsequent Base Treatments. *J. Phys. Chem. Solids* **2021**, *152*, 109962.
(44) VandeVondele, J.; Krack, M.; Mohamed, F.; Parrinello, M.; Chassaing, T.; Hutter, J.; Fast, Q. Fast and Accurate Density Functional Calculations Using a Mixed

Gaussian and Plane Waves Approach. *Comput. Phys. Commun.* **2005**, *167*, 103–128.

(45) Hutter, J.; Iannuzzi, M.; Schiffmann, F.; VandeVondele, J. CP2k: Atomistic Simulations of Condensed Matter Systems. *Wiley Interdiscip. Rev. Comput. Mol. Sci.* **2014**, *4*, 15–25.

(46) Perdew, J. P.; Burke, K.; Ernzerhof, M. Generalized Gradient Approximation Made Simple. *Phys. Rev. Lett.* **1996**, *77*, 3865–3868.

(47) Lin, I. C.; Seitsonen, A. P.; Tavernelli, I.; Rothlisberger, U. Structure and Dynamics of Liquid Water from Ab Initio Molecular Dynamics-Comparison of BLYP, PBE, and RevPBE Density Functionals with and without van Der Waals Corrections. *J. Chem. Theory Comput.* **2012**, *8*, 3902–3910.

(48) Chen, M.; Ko, H. Y.; Remsing, R. C.; Calegari Andrade, M. F.; Santra, B.; Sun, Z.; Selloni, A.; Car, R.; Klein, M. L.; Perdew, J. P.; Wu, X. Ab Initio Theory and Modeling of Water. *Proc. Natl. Acad. Sci. U. S. A.* **2017**, *114*, 10846–10851.

(49) Grimmel, S.; Schoendorff, G.; Wilson, A. K. Gauging the Performance of Density Functionals for Lanthanide-Containing Molecules. *J. Chem. Theory Comput.* **2016**, *12*, 1259–1266.

(50) Jaoul, A.; Nocton, G.; Clavaguéra, C. Assessment of Density Functionals for Computing Thermodynamic Properties of Lanthanide Complexes. *ChemPhysChem* **2017**, *18*, 2688–2696.

(51) Goedecker, S.; Teter, M.; Hutter, J. Separable Dual-Space Gaussian Pseudopotentials. *Phys. Rev. B - Condens. Matter Mater. Phys* **1996**, No. 54, 1703–1710.

(52) VandeVondele, J.; Hutter, J. Gaussian Basis Sets for Accurate Calculations on Molecular Systems in Gas and Condensed Phases. *J. Chem. Phys.* **2007**, *127*, 114105.

(53) Lu, J. B.; Cantu, D. C.; Nguyen, M. T.; Li, J.; Glezakou, V. A.; Rousseau, R. Norm-Conserving Pseudopotentials and Basis Sets to Explore Lanthanide Chemistry in Complex Environments. *J. Chem. Theory Comput.* **2019**, *15*, 5987–5997.

(54) Grimme, S.; Antony, J.; Ehrlich, S.; Krieg, H. A Consistent and Accurate Ab Initio Parametrization of Density Functional Dispersion Correction (DFT-D) for the 94 Elements H-Pu. *J. Chem. Phys.* **2010**, *132*, 154104.

(55) Shiery, R. C.; Fulton, J. L.; Balasubramanian, M.; Nguyen, M.-T.; Lu, J.-B.; Li, J.; Rousseau, R.; Glezakou, V.-A.; Cantu, D. C. Coordination Sphere of Lanthanide Aqua Ions Resolved with Ab Initio Molecular Dynamics and X-Ray Absorption Spectroscopy. *Inorg. Chem.* **2021**, *60*, 3117–3130.

(56) Kaliakin, D. S.; Sobrinho, J. A.; Monteiro, J. H. S. K.; de Bettencourt-Dias, A.; Cantu, D. C. Solution Structure of a Europium–Nicotianamine Complex Supports That Phytosiderophores Bind Lanthanides. *Phys. Chem. Chem. Phys.* **2021**, *23*, 4287–4299.

(57) Baerlocker, C.; McCusker, L. B. Database of Zeolite Structures http://www.iza-structure.org/databases/ (accessed May 25, 2021)

(58) Carter, E. A.; Ciccotti, G.; Hynes, J. T.; Kapral, R. Constrained Reaction Coordinate Dynamics for the Simulation of Rare Events. *Chem. Phys. Lett.* **1989**,

156, 472–477.
(59) Sprik, M.; Ciccotti, G. Free Energy from Constrained Molecular Dynamics. *J. Chem. Phys.* **1998**, *109*, 7737–7744.
(60) Schilling, M.; Luber, S. Determination of PKa Values via Ab Initio Molecular Dynamics and Its Application to Transition Metal-Based Water Oxidation Catalysts. *Inorganics* **2019**, *7*, 73.
(61) Sprik, M. Computation of the PK of Liquid Water Using Coordination Constraints. *Chem. Phys.* **2000**, *258*, 139–150.
(62) Sulpizi, M.; Sprik, M. Acidity Constants from DFT-Based Molecular Dynamics Simulations. *J. Phys. Condens. Matter* **2010**, *22*, 284116.
(63) Cheng, J.; Liu, X.; VandeVondele, J.; Sulpizi, M.; Sprik, M. Redox Potentials and Acidity Constants from Density Functional Theory Based Molecular Dynamics. *Acc. Chem. Res.* **2014**, *47*, 3522–3529.
(64) Hass, K. C.; Schneider, W. F.; Curioni, A.; Andreoni, W. The Chemistry of Water on Alumina Surfaces: Reaction Dynamics from First Principles. *Science (80-.).* **1998**, *282*, 265–268.
(65) Ivanov, I.; Chen, B.; Raugei, S.; Klein, M. L. Relative PKa Values from First-Principles Molecular Dynamics: The Case of Histidine Deprotonation. *J. Phys. Chem. B* **2006**, *110*, 6365–6371.
(66) De Meyer, T.; Ensing, B.; Rogge, S. M. J.; De Clerck, K.; Meijer, E. J.; Van Speybroeck, V. Acidity Constant PKa Calculation of Large Solvated Dye Molecules: Evaluation of Two Advanced Molecular Dynamics Methods. *Chemphyschem* **2016**, *17*, 3447–3459.
(67) Kılıç, M.; Ensing, B. Acidity Constants of Lumiflavin from First Principles Molecular Dynamics Simulations. *Phys. Chem. Chem. Phys.* **2014**, *16*, 18993–19000.
(68) Chen, Y.-L.; Doltsinis, N. L.; Hider, R. C.; Barlow, D. J. Prediction of Absolute Hydroxyl PKa Values for 3-Hydroxypyridin-4-Ones. *J. Phys. Chem. Lett.* **2012**, *3*, 2980–2985.
(69) Tummanapelli, A. K.; Vasudevan, S. Dissociation Constants of Weak Acids from Ab Initio Molecular Dynamics Using Metadynamics: Influence of the Inductive Effect and Hydrogen Bonding on PKa Values. *J. Phys. Chem. B* **2014**, *118*, 13651–13657.
(70) Smith, L.; Cheetham, A. K.; Morris, R. E.; Marchese, L.; Thomas, J. M.; Wright, P. A.; Chen, J. On the Nature of Water Bound to a Solid Acid Catalyst. *Science (80-.).* **1996**, *271*, 799 LP – 802.
(71) Termath, V.; Haase, F.; Sauer, J.; Hutter, J.; Parrinello, M. Understanding the Nature of Water Bound to Solid Acid Surfaces. Ab Initio Simulation on HSAPO-34. *J. Am. Chem. Soc.* **1998**, *120*, 8512–8516.
(72) Vjunov, A.; Fulton, J. L.; Huthwelker, T.; Pin, S.; Mei, D.; Schenter, G. K.; Govind, N.; Camaioni, D. M.; Hu, J. Z.; Lercher, J. A. Quantitatively Probing the Al Distribution in Zeolites. *J. Am. Chem. Soc.* **2014**, *136*, 8296–8306.
(73) Liu, P.; Mei, D. Identifying Free Energy Landscapes of Proton-Transfer Processes between Brønsted Acid Sites and Water Clusters Inside the Zeolite Pores. *J. Phys. Chem. C* **2020**, *124*, 22568–22576.

(74) Grifoni, E.; Piccini, G.; Lercher, J.; Glezakou, V.-A.; Rousseau, R.; Parrinello, M. Confinement Effects and Acid Strength in Zeolites. *Nat. Commun.* **2021**, *12*, 2630.
(75) Khalid, M.; Joly, G.; Renaud, A.; Magnoux, P. Removal of Phenol from Water by Adsorption Using Zeolites. *Ind. Eng. Chem. Res.* **2004**, *43*, 5275–5280.
(76) Trzpit, M.; Soulard, M.; Patarin, J.; Desbiens, N.; Cailliez, F.; Boutin, A.; Demachy, I.; Fuchs, A. H. The Effect of Local Defects on Water Adsorption in Silicalite-1 Zeolite: A Joint Experimental and Molecular Simulation Study. *Langmuir* **2007**, *23*, 10131–10139.
(77) Humplik, T.; Raj, R.; Maroo, S. C.; Laoui, T.; Wang, E. N. Effect of Hydrophilic Defects on Water Transport in MFI Zeolites. *Langmuir* **2014**, *30*, 6446–6453.
(78) Zhou, T.; Bai, P.; Siepmann, J. I.; Clark, A. E. Deconstructing the Confinement Effect upon the Organization and Dynamics of Water in Hydrophobic Nanoporous Materials: Lessons Learned from Zeolites. *J. Phys. Chem. C* **2017**, *121*, 22015–22024.

Supporting Information for Chapter 6

Placement of H atoms in FAU-5

Table 6-S1. The relative energies of H-FAU-5, with the H atom in the four different oxygen atoms of its Al tetrahedron:

Al tetrahedral oxygen site	**Relative energies (kJ/mol)**
Hexagonal window of a sodalite	0 (lowest energy, reference state)
Large window between two supercages	+8 kJ/mol
Large window between two supercages	+15 kJ/mol
Square window of a hexagonal prism	+40 kJ/mol

Therefore, we placed the H-atoms on the H-FAU-5 models preferably on hexagonal windows, with two exceptions: i) when an Al tetrahedra did not form part of a hexagonal window, in such case they were placed in the supercage, and ii), to calculate the binding energy of water on an -OH group in a particular FAU site (e.g., S1 hexagonal prism).

Table 6-S2. Comparing the energies of different H-FAU-5 model structures

Unit cell dimensions and energies of the optimized structures of H-FAU-5 model structures with different Al distributions

Model Structures	Unit cell dimensions ($\alpha = \beta = \gamma = 60^{o}$)	Relative Energy (kJ/mol)	Lowenstein's Rule
Lowest energy structure	a=b=c=17.530 Å	0	Does not violate
Isomer 1	a=b=c=17.516 Å	1	Does not violate
Isomer 2	a=b=c=17.544 Å	99	Violates
Isomer 3	a=b=c=17.539 Å	132	Violates
Isomer 4	a=b=c=17.533 Å	181	Violates

CHAPTER 7

Cation induced disruption of the local structure of water in faujasite

Richard C. Shiery, David C. Cantu

Department of Chemical and Materials Engineering, University of Nevada, Reno

Modified from a manuscript that was submitted to *The Journal of Physical Chemistry C* with the same title and authors

7.1. Introduction

Faujasite (FAU) is a zeolite that has applications as a catalyst, absorbent, and ion exchanger. The applications of FAU as an ion exchanger range from treatment and separation of radioactive elements from nuclear waste[1] to removal of conventional heavy metal contaminants[2,3] and separations of rare earth metals.[4–8]

For separations in water, for example ion exchange, zeolites will operate under a range of solution pH values.[2,9–11] Hydrogen exchanged zeolites possess Brønsted acid sites that provide catalytic properties, for example in the cracking of petroleum or other conversions of organic compounds.[12–21] Brønsted acid sites increase the hydrophilicity of aluminum tetrahedra and provide binding sites for water molecules, promoting water-mediated dealumination.[22–25] Ion exchange affects the Brønsted acidity of faujasite, for example La^{3+} binding on hydrogen exchanged FAU favors the deprotonation of OH groups in aluminum tetrahedra and reduce their hydrophilicity.[22] The Brønsted acidity of hydrogen-exchanged FAU depends on the number of structural aluminum present, and Si/Al ratio will affect acid catalyzed reactions, shown by optimal Si/Al ratios for catalytic performance.[26] Si/Al ratio is also known to affect the chemical and physical properties of zeolites in liquid water in the context of ion exchange.[27] Therefore, it is important to determine how the structure of liquid water in zeolitic confinement is affected by Si/Al ratio and exchanged cation.

The structure of confined water in zeolites has been quantified through x-ray diffraction measurements,[28,29] and with molecular simulations.[30–35] However, the effect of Si/Al ratio, and that of which counter ion is exchanged, on the structure of water has been studied much less. The work presented here examines how Si/Al ratio (hydrophilicity in

hydrogen-exchanged FAU), as well as which cation is exchanged in FAU, affect the structure of confined water.

7.2. Computational Methods

All density functional theory (DFT) calculations and *ab initio* molecule dynamics (AIMD) simulations were performed with the CP2K[36,37] package utilizing the general gradient approximation and the PBE functional.[38] The core electrons were modeled with norm conserving GTH pseudopotentials,[39] while the valence electrons were modeled with a polarizable double zeta basis set.[40] For lanthanum, we used our LnPP1 pseudopotential and basis set.[41] The long range electrostatics were calculated using a supplementary plane wave basis set with a 500 Ry cutoff. The van der Waals interactions were included with Grimme's D3 corrections[42] within a 6.0 Å radius.

We independently simulated eight different water-containing FAU systems, each including 55 explicit water molecules, as well as different exchange cations, in a rhombohedral periodic box with varying box lengths as seen in **Table 7-1**. A cubic water box containing 55 explicit water molecules was also simulated.

Table 7-1: Simulated systems and optimized periodic box dimensions

System Description	**a=b=c (Å)**	**α=β=γ (°)**
Pure Water, 55 water molecules	11.800	90
FAU, all Si, 55 water molecules	17.254	60
12H-FAU3, Si/Al=3, 55 water molecules	17.485	60
8H-FAU5, Si/Al=5, 55 water molecules	17.412	60
4H-FAU11, Si/Al=11, 55 water molecules	17.279	60
1La5H-FAU5, Si/Al=5, 55 water molecules	17.391	60
2La2H-FAU5, Si/Al=5, 55 water molecules	17.403	60
3Na5H-FAU5, Si/Al=5, 55 water molecules	17.254	60
6Na2H-FAU5, Si/Al=5, 55 water molecules	17.399	60

A consistent number, fifty-five (55), of water molecules was used to better compare the O_{wat}-O_{wat} radial distribution functions between the different systems in **Table 7-1** and avoid the structure of confined water being affected by the number of water molecules, due to the limited sampling inherent in DFT AIMD simulations. The number of water molecules in FAU was determined from a series of canonical ensemble (NVT) simulations (2ps total, 1fs time step) of the all-Si FAU, with the number of water molecules ranging from 45 to 85, and selecting the number of water molecules that produced the lowest non-negative pressure. **Figure 7-1** shows the all-Si FAU structure with 55 water molecules.

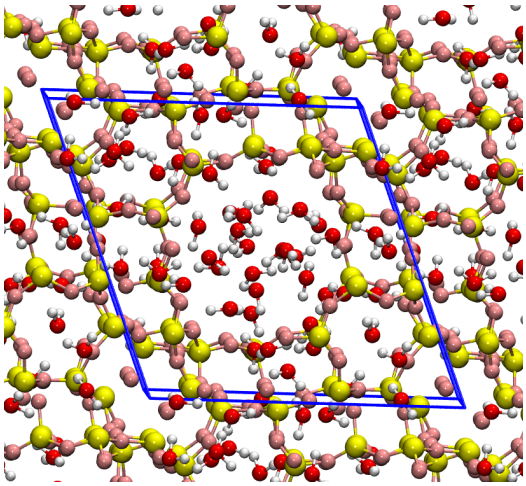

Figure 7-1. All-Si FAU with 55 water molecules, FAU oxygen atoms are pink, silicon atoms are yellow, while water oxygen atoms are red and hydrogen atoms are white.

All faujasite model structures were prepared as described in our previous work.[22] The initial model of an all-Si FAU was obtained from the Database of Zeolite Structures,[43] and converted to a rhombohedral cell to reduce the number of atoms.[44] The 8H-FAU5 model structure was prepared in our previous work,[22] by replacing Si framework atoms with Al, following Löwenstein's rule, and performing a cell

optimization calculation in CP2K. The models of faujasite with a Si/Al ratio of 3 (12H-FAU3) and 11 (4H-FAU11) were constructed from the 8H-FAU5 model (Si/Al ratio of 5), replacing structural aluminum with silica, or vice versa, to increase, or decrease, the Si/Al ratio while following Löwenstein's rule, and optimized the periodic cell dimensions and molecular geometry for each. 12H-FAU3 contains twelve Al tetrahedra, thirty-six silica tetrahedra and twelve hydrogen atoms. 8H-FAU5 contains eight Al tetrahedra, forty silica tetrahedra and eight hydrogen atoms. 4H-FAU11 contains four Al tetrahedra, forty-four silica tetrahedra and four hydrogen atoms. For systems that also contain La^{3+} or Na^{+}, the added ions substituted hydrogen atoms to ensure a net neutral system. The La^{3+} and Na^{+} ions that replaced the hydrogens were placed in the hexagonal window of the sodalite cage and square window of the supercage as to remain near the original aluminum tetrahedra.

AIMD simulations of nine systems in **Table 7-1** were conducted in the NVT ensemble at 298 K, running for at least 20,000 steps with a 1 fs timestep. The last 15 ps were subject to analysis via O_{wat}-O_{wat} radial distribution functions (RDF) to quantify the structure of water in FAU. Changes between the O_{wat}-O_{wat} RDFs of different systems are indicative of how different Si/Al ratios (hydrophilicity) and exchanged ions changes in the structure of water in faujasite.

The Helmholtz free energies of proton transfer were extracted from potentials of mean force of proton transfer produced by constrained Bluemoon[45,46] AIMD simulations to quantity the acidity of H-FAU in regards to water in the gas phase and in the condensed phase. We pulled a proton from a FAU Al tetrahedral site to a neighboring water molecule in increments in 0.05 Å along the O-H bond distance ranging from ~1.00

Å to ~1.40 Å. The reaction coordinate (r_{O-H}) is an adequate constraint to describe proton transfer in inorganic systems,[47–49] and was used to quantify the Brønsted acidity of H-FAU in the gas phase in our previous work.[22] Nine independent AIMD simulations were performed with different O-H distances (r_{O-H}). For each AIMD simulation, r_{O-H} was constrained, and 15 ps of NVT (at 298 K) simulation were generated with a 0.5 fs time step. The forces on the constraint (SHAKE Lagragian multipliers) were averaged over the last 10 ps of the NVT simulation and were used to calculate the average force on the constraint. The potential of mean force was obtained by integrating the forces on the constraint over r_{O-H}.

7.3. Results and Discussion

Changes in the structure of water were quantified by comparing the O_{wat}-O_{wat} RDFs of the nine different systems (**Table 7-1**). The water box provides an unconfined system to compare to the all-Si FAU to examine confinement without Brønsted acidity or contributions from counterions. The RDFs of 12H-FAU3, 8H-FAU5, and 4H-FAU11 captured changes in the structure of water due to changes in Brønsted acidity, and the systems containing lanthanum and sodium were used to quantify the effect of the number of exchanged ions and charge. **Table 7-2** summarizes the results by showing the distance of the first peak and the average number of water molecules in the first coordination sphere of a water molecule. A higher number of water molecules in the first coordination sphere is a measure of a more ordered water structure.

Table 7-2. Maximum of the first peak, and number of water molecules in the first coordination sphere, for the eight water containing systems.

System Description	First peak maximum (Å)	Number of water molecules in first coordination sphere
Pure Water, 55 water molecules	2.72	2.11
FAU, all Si, 55 water molecules	2.77	3.40
12H-FAU3, Si/Al=3, 55 water molecules	2.68	2.54
8H-FAU5, Si/Al=5, 55 water molecules	2.69	2.98
4H-FAU11, Si/Al=11, 55 water molecules	2.73	3.11
1La5H-FAU5, Si/Al=5, 55 water molecules	2.73	3.01
2La2H-FAU5, Si/Al=5, 55 water molecules	2.73	3.02
3Na5H-FAU5, Si/Al=5, 55 water molecules	2.71	2.80
6Na2H-FAU5, Si/Al=5, 55 water molecules	2.73	2.95

Comparing the O_{wat}-O_{wat} RDFs of the water box and the all-Si FAU displayed a greater population of similarly distanced water molecules in the all-Si FAU. The population of water molecules that are within 2.5 Å to 3.0 Å of each other increases for water confined in FAU (**Figure 7-2**). This agrees with experimental and computational studies that report O_{wat}-O_{wat} distances between 2.74 Å to 2.79 Å for confined water.[28,32] Water becomes more hydrogen bound in all-Si FAU confinement as the peak of the O_{wat}-O_{wat} RDF increases from 2.72 Å to 2.77 Å (**Table 7-2**), which is also shown by an increase of molecules in the first coordination sphere from 2.11 to 3.40. FAU confinement produces a more orderly arrangement of water molecules.

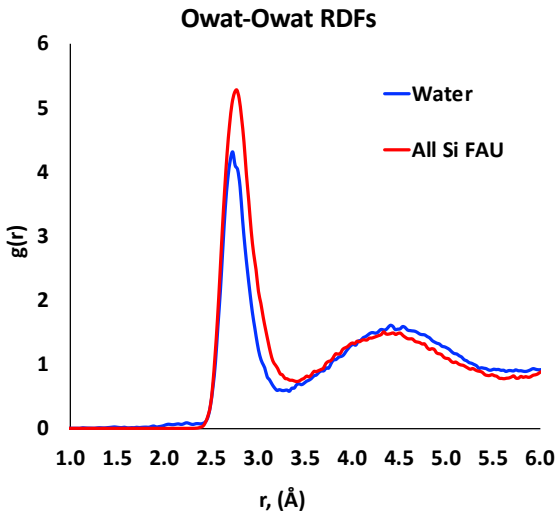

Figure 7-2. The O_{wat}-O_{wat} radial distribution function for the water box (blue) and the all-Si FAU (red). Water confined in FAU has a higher population of similarly distanced water molecules, in the hydrogen-bonding range, compared to pure water.

The addition of aluminum tetrahedra increases the hydrophilicity of hydrogen-exchanged faujasite. As more aluminum is added, the populations of similarly distanced water molecules in the O_{wat}-O_{wat} RDFs of 4H-FAU11 to 12H-FAU decreases, see **Figure 7-3A**. Aluminum tetrahedra in H-FAU attract water molecules, and as the number of Al tetrahedra increases, it disrupts the uniformity of confined water in all-Si H-FAU. This is likely because, in the liquid phase, H-FAU protons dissociate from FAU resulting in solvated H_3O^+ species, which are shown by the H_{FAU}-Al RDFs (**Figure 7-3B**). The increase in hydrophilicity diminishes the number of water molecules in the hydrogen bonding range, as shown by broader O_{wat}-O_{wat} peaks with a lower population between 2.5

and 3.0 Å (**Figure 7-3A**), and by a lower number of water molecules in the first coordination sphere of a water with increasing Al content (**Table 7-2**).

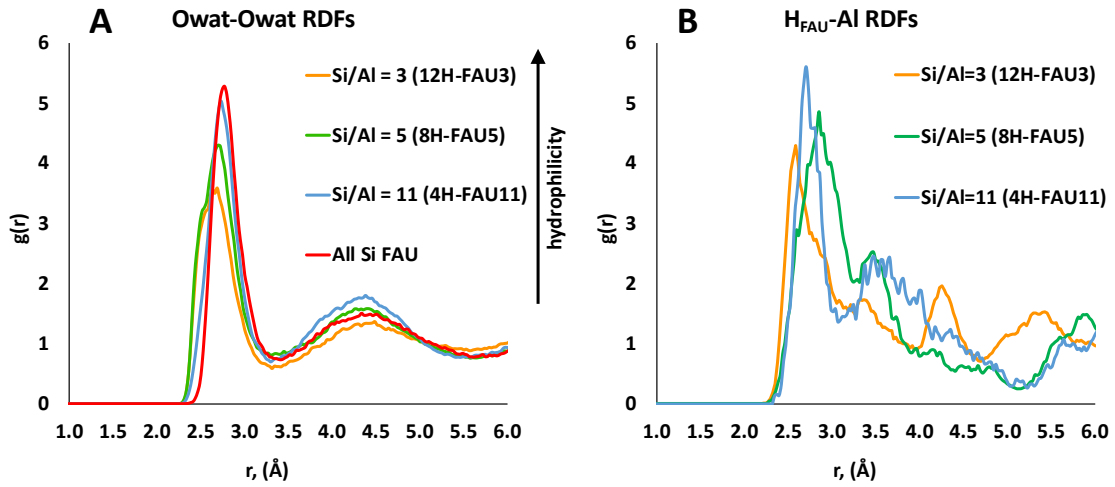

Figure 7-3. A: The O_{wat}-O_{wat} radial distribution function for the all-Si H-FAU compared against the systems with varying Si/Al ratio of 3, 5 and 11. As more Al is added, the population of similarly-distanced water molecules decreases, indicating a more disordered water structure. **B:** The H_{FAU}-Al radial distribution function for hydrogen exchanged FAU for Si/Al ratio of 3, 5, and 11.

Since protons affect the confined water structure, we quantified how liquid water changes the Brønsted acidity of H-FAU. A potential of mean force of proton transfer of an 8H-FAU5 hydrogen on an aluminum tetrahedra to a neighboring water molecule in the supercage was constructed and appears in **Figure 7-4**. **Figure 7-4** also includes the potential of mean force of the same proton transfer, but to a neighboring water molecule in the gas phase, which was published in our previous work.[22] The gas phase free energy profile is that of proton transfer from FAU to three water molecules in the supercage, while the liquid phase free energy profile is that of proton transfer from FAU to water-filled supercage. The potentials of mean force show that, for hydrogen exchanged FAU5, protons are energetically favored to remain bound to Al tetrahedra in the gas phase, but

protons are energetically favored to become unbound in the liquid phase, and form H_3O^+ species in water-filled pores. Therefore, the presence of water increases the Brønsted acidity of hydrogen-exchanged faujasite. Similarly, recent experimental and computational studies have shown that, in the presence of water, protons on Al tetrahedra readily dissociate in other zeolite structures such as ZSM-5 or chabazite.[50,51]

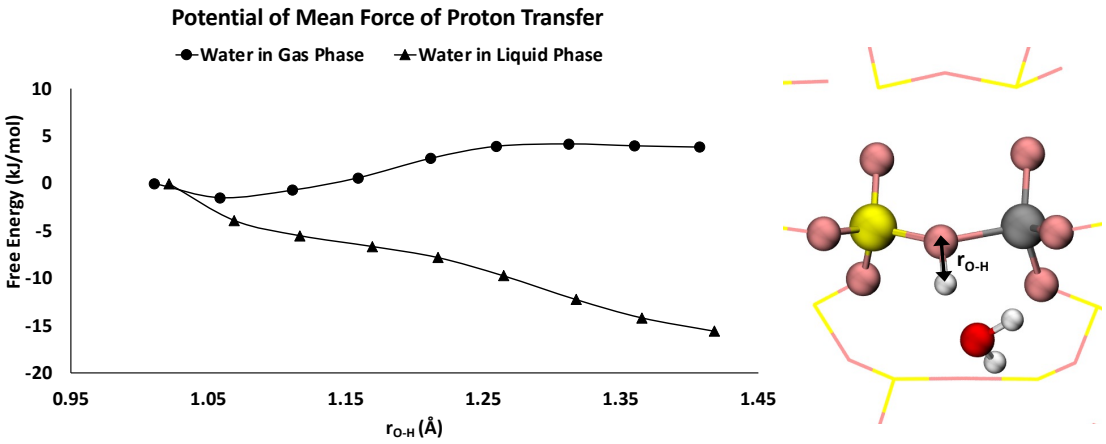

Figure 7-4. Potentials of mean force of proton transfer from an 8H-FAU5 Al tetrahedra to a neighboring water molecule, for a low number of water in the supercage (gas phase) and a water-filled supercage (liquid phase). The graphic on the right shows $r_{O\text{-}H}$, which increases as the proton is slowly moved from FAU to a nearby water molecule.

Figure 7-5 compares the effect of ion charge and number of ions on the structure of water in faujasite. The general trend established by the plot of the O_{wat}-O_{wat} RDF for the systems that contained sodium or lanthanum was that additional exchanged ions resulted in higher water disorder, as observed with H^+ in **Figure 7-3**. However, the number of ions is relevant, and not only the total compensated charge from how many Al tetrahedra are present, as two La^{3+} ions had a less significant change in the population of similarly distanced water molecules compared to the six Na^+ ions (**Figures 7-5A, 7-5C**). Implications for ion exchange are dependent on the disruption in the structure of water,

large highly charged molecules will produce less disruption once bound. A higher number of ions present results in a higher disruption of the local structure of water, since the more ions confined in FAU increases the likelihood of ions being in the large pores and interacting with confined water molecules. However, unlike H^+, Na^+ and La^{3+} remained in the vicinity of Al tetrahedra, as shown by La-Al and Na-Al RDFs.

Due to the higher number of Na^+ ions needed, once the initial Na^+ ions occupy sodalite binding sites, additional Na^+ will bind in the square or hexagonal windows of the supercage. The presence of Na^+ in the supercage disrupts water structure, in contrast to less La^{3+} ions, bound in the sodalite cage, away from the open pore, and thus interacts with fewer water molecules. Ion coordination also contributes to the disruption of local water structure, as large, highly charged ions (La^{3+}) coordinate more water molecules than monovalent Na^+ ions. The disruption in the local structure of water decreases the

population of similarly distanced water molecules, which correlates to the presence of more ions in the open pore with the confined water.

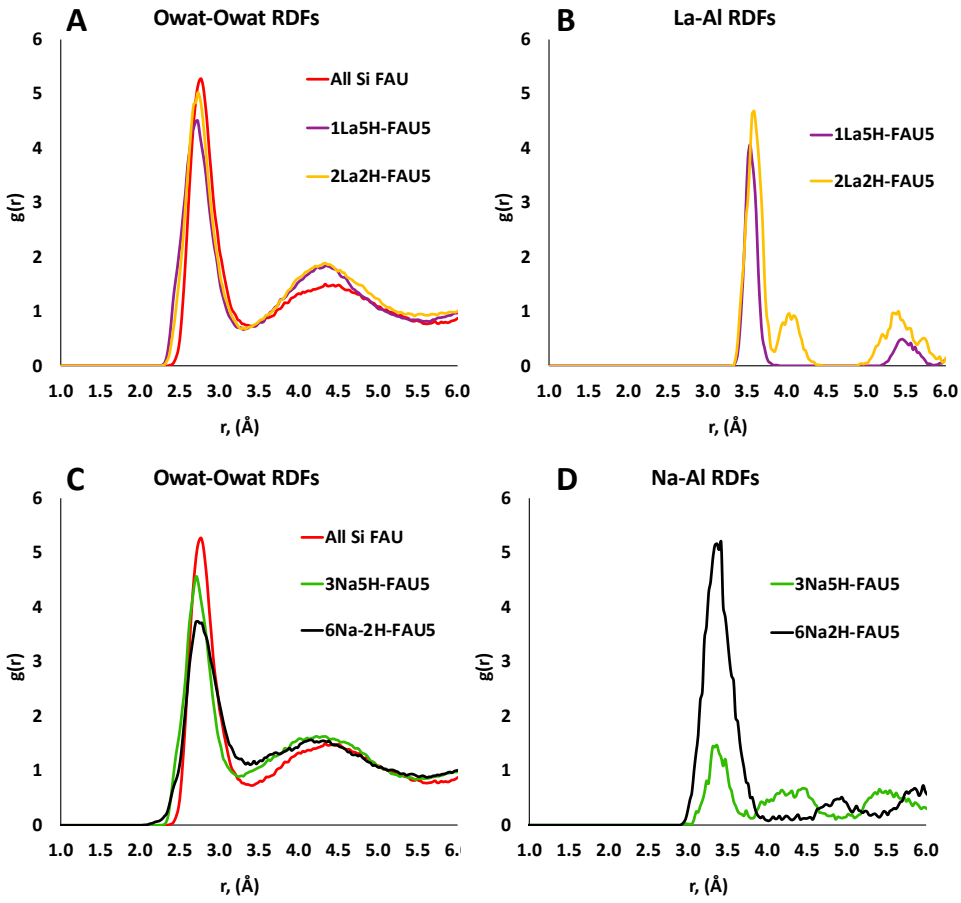

Figure 7-5. A: The O_{wat}-O_{wat} radial distribution function for the all-Si FAU compared with the La^{3+} exchanged FAU5. **B:** La-Al radial distribution function for La^{3+} exchanged FAU5 **C:** The O_{wat}-O_{wat} radial distribution function for the all-Si FAU compared with Na^{+} exchanged FAU5. **D:** Na-Al radial distribution function for La^{3+} exchanged FAU5.

7.4. Conclusion

How confinement, Si/Al ratio, and ion charge alter the structure of water in faujasite was examined by analyzing O_{wat}-O_{wat} radial distribution functions obtained from AIMD simulations. Confinement in the all-Si faujasite resulted in a higher population of

similarly distanced water molecules, and thus more ordered than unconfined liquid water. In hydrogen exchanged FAU, the increase in aluminum content led to the disruption of the confined water structure as more protons entered the liquid water. This is consistent with the free energy profile of proton transfer which shows that it is thermodynamically favored for protons to be in the liquid water rather than bound to FAU Al tetrahedra. Exchanged Na^+ and La^{3+} counterions also disordered the confined water structure, despite remaining in the vicinity of Al tetrahedra in liquid water. The number of counterions to balance the Al in FAU has a larger effect on the structure of water than the charge of the ion itself, as two La^{3+} ions disrupted water less than six Na^+ ions.

Chapter 7 References

(1) Gu, B. X.; Wang, L. M.; Ewing, R. C. Effect of Amorphization on the Cs Ion Exchange and Retention Capacity of Zeolite-NaY. *J. Nucl. Mater.* **2000**, *278* (1), 64–72.

(2) Mekatel, H.; Amokrane, S.; Benturki, A.; Nibou, D. Treatment of Polluted Aqueous Solutions by Ni 2+, Pb 2+, Zn 2+, Cr +6, Cd +2 and Co +2 Ions by Ion Exchange Process Using Faujasite Zeolite. *Procedia Eng.* **2012**, *33* (2011), 52–57.

(3) Woltermann, G. M.; Magee, J. S.; Griffith, S. D. Chapter 4 Commercial Preparation and Characterization of FCC Catalysts. In *Fluid Catalytic Cracking: Science and Technology*; Elsevier, 1993; Vol. 76, pp 105–144.

(4) Zuyi, T.; Quanchang, L. Studies on Ion Exchange Equilibria and Kinetics VII. Tb3+-Na§ Cation Exchange Equilibria and Kinetics in Zeolite-Y. **1997**, *223*, 173–176.

(5) Shy, D. S.; Chen, S. H.; Lievens, J.; Liu, S. Bin; Chao, K. J. Distribution of Cations in Lanthanum-Exchanged NaY Zeolites. *J. Chem. Soc. Faraday Trans.* **1991**, *87* (17), 2855–2859.

(6) Rees, L. V. C.; Zuyi, T. Rare-Earth Ion Exchange in Zeolite Y. *Zeolites* **1986**, *6* (July 1985), 201–205.

(7) Chen, S. H.; Chao, K. J.; Lee, T. Y. Lanthanum-NaY Zeolite Ion Exchange. 1. Thermodynamics and Thermochemistry. *Ind. Eng. Chem. Res.* **1990**, *29* (10), 2020–2023.

(8) Sherry, H. S. Cation Exchange on Zeolites. **1974**, 350–379.

(9) Li, C. Y.; Rees, L. V. C. Ion Exchange in Dealuminated Faujasites. *Zeolites* **1986**, *6* (1), 51–59.

(10) Chang, H. L.; Shih, W. H. A General Method for the Conversion of Fly Ash into Zeolites as Ion Exchangers for Cesium. *Ind. Eng. Chem. Res.* **1998**, *37* (1), 71–78.

(11) Gould, N. S.; Xu, B. Effect of Liquid Water on Acid Sites of NaY: An in Situ Liquid Phase Spectroscopic Study. *J. Catal.* **2016**, *342*, 193–202.

(12) Xu, T.; Munson, E. J.; Haw, J. F. Toward a Systematic Chemistry of Organic Reactions in Zeolites: In Situ NMR Studies of Ketones. *J. Am. Chem. Soc.* **1994**, *116* (5), 1962–1972.

(13) Corma, A. Inorganic Solid Acids and Their Use in Acid-Catalyzed Hydrocarbon Reactions. *Chem. Rev.* **1995**, *95* (3), 559–614.

(14) Li, S.; Zheng, A.; Su, Y.; Zhang, H.; Chen, L.; Yang, J.; Ye, C.; Deng, F. Brønsted/Lewis Acid Synergy in Dealuminated HY Zeolite: A Combined Solid-State NMR and Theoretical Calculation Study. *J. Am. Chem. Soc.* **2007**, *129* (36), 11161–11171.

(15) Noda, T.; Suzuki, K.; Katada, N.; Niwa, M. Combined Study of IRMS-TPD Measurement and DFT Calculation on Brønsted Acidity and Catalytic Cracking Activity of Cation-Exchanged Y Zeolites. *J. Catal.* **2008**, *259* (2), 203–210.

(16) Gounder, R.; Iglesia, E. The Catalytic Diversity of Zeolites: Confinement and Solvation Effects within Voids of Molecular Dimensions. *Chem. Commun.* **2013**, *49* (34), 3491–3509.

(17) Bui, L.; Luo, H.; Gunther, W. R.; Román-Leshkov, Y. Domino Reaction Catalyzed

by Zeolites with Brønsted and Lewis Acid Sites for the Production of γ-Valerolactone from Furfural. *Angew. Chemie* **2013**, *125* (31), 8180–8183.
(18) Hemelsoet, K.; Van der Mynsbrugge, J.; De Wispelaere, K.; Waroquier, M.; Van Speybroeck, V. Unraveling the Reaction Mechanisms Governing Methanol-to-Olefins Catalysis by Theory and Experiment. *ChemPhysChem* **2013**, *14* (8), 1526–1545.
(19) Primo, A.; Garcia, H. Zeolites as Catalysts in Oil Refining. *Chem. Soc. Rev.* **2014**, *43* (22), 7548–7561.
(20) Vogt, E. T. C.; Weckhuysen, B. M. Fluid Catalytic Cracking: Recent Developments on the Grand Old Lady of Zeolite Catalysis. *Chem. Soc. Rev.* **2015**, *44* (20), 7342–7370.
(21) Koehle, M.; Zhang, Z.; Goulas, K. A.; Caratzoulas, S.; Vlachos, D. G.; Lobo, R. F. Acylation of Methylfuran with Brønsted and Lewis Acid Zeolites. *Appl. Catal. A Gen.* **2018**, *564*, 90–101.
(22) Shiery, R. C.; Mcelhany, S. J.; Cantu, D. C. Effect of Lanthanum Ions on the Brønsted Acidity of Faujasite and Implications for Hydrothermal Stability. *J. Phys. Chem. C* **2021**, *125* (24), 13649–13657.
(23) Nielsen, M.; Hafreager, A.; Brogaard, R. Y.; De Wispelaere, K.; Falsig, H.; Beato, P.; Van Speybroeck, V.; Svelle, S. Collective Action of Water Molecules in Zeolite Dealumination. *Catal. Sci. Technol.* **2019**, *9* (14), 3721–3725.
(24) Zhang, L.; Qin, Y.; Zhang, X.; Gao, X.; Song, L. Further Findings on the Stabilization Mechanism among Modified y Zeolite with Different Rare Earth Ions. *Ind. Eng. Chem. Res.* **2019**, *58* (31), 14016–14025.
(25) Sun, J.; Fang, H.; Ravikovitch, P. I.; Sholl, D. S. Understanding Dealumination Mechanisms in Protonic and Cationic Zeolites. *J. Phys. Chem. C* **2020**, *124* (1), 668–676.
(26) Corma, A.; Melo, F. V.; Rawlence, D. Effect of the Nonuniform Dealumination on the Acidity and Catalytic Activity of Faujasite: Part 2. Accessibility of Acid Sites. *Zeolites* **1992**, *12* (3), 261–264.
(27) Colella, C. Ion Exchange Equilibria in Zeolite Minerals. **1996**, *562*, 554–562.
(28) Perez, C. A. C.; De Resende, N. S.; Salim, V. M. M.; Schmal, M. Water Interaction in Faujasite Probed by in Situ X-Ray Powder Diffraction. *J. Phys. Chem. C* **2017**, *121* (5), 2755–2761.
(29) Baur, W. H. On the Cation and Water Positions in Faujasite. *Amercian Mineral.* **1964**, *49* (5–6), 697–704.
(30) Coudert, F.-X.; Vuilleumier, R.; Boutin, A. Dipole Moment, Hydrogen Bonding and IR Spectrum of Confined Water. *ChemPhysChem* **2006**, *7* (12), 2464–2467.
(31) Abrioux, C.; Coasne, B.; Maurin, G.; Henn, F.; Jeffroy, M.; Boutin, A. Cation Behavior in Faujasite Zeolites upon Water Adsorption: A Combination of Monte Carlo and Molecular Dynamics Simulations. *J. Phys. Chem. C* **2009**, *113* (24), 10696–10705.
(32) Calero, S.; Gómez-Álvarez, P. Hydrogen Bonding of Water Confined in Zeolites and Their Zeolitic Imidazolate Framework Counterparts. *RSC Adv.* **2014**, *4* (56), 29571–29580.
(33) Beauvais, C.; Boutin, A.; Fuchs, A. H. Adsorption of Water in Zeolite Sodium-

Faujasite. *Comptes Rendus Chim.* **2005**, *8* (3–4), 485–490.
(34) Bai, P.; Neurock, M.; Siepmann, J. I. First-Principles Grand-Canonical Simulations of Water Adsorption in Proton-Exchanged Zeolites. *J. Phys. Chem. C* **2021**, *125* (11), 6090–6098.
(35) Ammouli, T.; Paillaud, J.-L.; Nouali, H.; Stephan, R.; Hanf, M.-C.; Sonnet, P.; Deroche, I. Insights into Water Adsorption in Potassium-Exchanged X-Type Faujasite Zeolite: Molecular Simulation and Experiment. *J. Phys. Chem. C* **2021**, *125* (35), 19405–19416.
(36) Hutter, J.; Iannuzzi, M.; Schiffmann, F.; VandeVondele, J. CP2k: Atomistic Simulations of Condensed Matter Systems. *Wiley Interdiscip. Rev. Comput. Mol. Sci.* **2014**, *4* (1), 15–25.
(37) VandeVondele, J.; Krack, M.; Mohamed, F.; Parrinello, M.; Chassaing, T.; Hutter, J.; Fast, Q. Fast and Accurate Density Functional Calculations Using a Mixed Gaussian and Plane Waves Approach. *Comput. Phys. Commun.* **2005**, *167* (2), 103–128.
(38) Perdew, J. P.; Burke, K.; Ernzerhof, M. Generalized Gradient Approximation Made Simple. *Phys. Rev. Lett.* **1996**, *77* (18), 3865–3868.
(39) Goedecker. Separable Dual-Space Gaussian Pseudopotentials. *Phys. Rev. B - Condens. Matter Mater. Phys* **1996**, No. 54, 1703–1710.
(40) VandeVondele, J.; Hutter, J. Gaussian Basis Sets for Accurate Calculations on Molecular Systems in Gas and Condensed Phases. *J. Chem. Phys.* **2007**, *127*, 114105.
(41) Lu, J. B.; Cantu, D. C.; Nguyen, M. T.; Li, J.; Glezakou, V. A.; Rousseau, R. Norm-Conserving Pseudopotentials and Basis Sets to Explore Lanthanide Chemistry in Complex Environments. *J. Chem. Theory Comput.* **2019**, *15*, 5987–5997.
(42) Grimme, S.; Antony, J.; Ehrlich, S.; Krieg, H. A Consistent and Accurate Ab Initio Parametrization of Density Functional Dispersion Correction (DFT-D) for the 94 Elements H-Pu. *J. Chem. Phys.* **2010**, *132*, 154104.
(43) Baerlocker, C.; McCusker, L. B. *Database of Zeolite Structures*. http://www.iza-structure.org/databases/.
(44) Schüßler, F.; Pidko, E.; Kolvenbach, R.; Sievers, C.; Hensen, E. .; van Santen, R. A.; Lercher, J. A. Nature and Location of Cationic Lanthanum Species in High Alumina Containing Faujasite Type Zeolites. *J. Phys. Chem.* **2011**, *259*.
(45) Sprik, M.; Ciccotti, G. Free Energy from Constrained Molecular Dynamics. *J. Chem. Phys.* **1998**, *109* (18), 7737–7744.
(46) Carter, E. A.; Ciccotti, G.; Hynes, J. T.; Kapral, R. Constrained Reaction Coordinate Dynamics for the Simulation of Rare Events. *Chem. Phys. Lett.* **1989**, *156* (5), 472–477.
(47) Hass, K. C.; Schneider, W. F.; Curioni, A.; Andreoni, W. The Chemistry of Water on Alumina Surfaces: Reaction Dynamics from First Principles. *Science (80-.).* **1998**, *282* (5387), 265–268.
(48) Schilling, M.; Luber, S. Determination of PKa Values via Ab Initio Molecular Dynamics and Its Application to Transition Metal-Based Water Oxidation Catalysts. *Inorganics* **2019**, *7* (6), 73.

(49) Shiery, R. C.; Cooper, K. A.; Cantu, D. C. Computational Prediction of All Lanthanide Aqua Ion Acidity Constants. *Inorg. Chem.* **2021**, *60* (14), 10257–10266.
(50) Wang, M.; Jaegers, N. R.; Lee, M.-S.; Wan, C.; Hu, J. Z.; Shi, H.; Mei, D.; Burton, S. D.; Camaioni, D. M.; Gutiérrez, O. Y.; Glezakou, V.-A.; Rousseau, R.; Wang, Y.; Lercher, J. A. Genesis and Stability of Hydronium Ions in Zeolite Channels. *J. Am. Chem. Soc.* **2019**, *141* (8), 3444–3455.
(51) Grifoni, E.; Piccini, G.; Lercher, J.; Glezakou, V.-A.; Rousseau, R.; Parrinello, M. Confinement Effects and Acid Strength in Zeolites. *Nat. Commun.* **2021**, *12*, 2630.

CHAPTER 8

Conclusions

The *f*-orbital chemistry of the lanthanides provides them with unique properties that are essential for their applications. However, it is the similar properties of elements in the lanthanide series that provide challenges for rare earth separations: similar ionic radius, oxidation states, and reactions, such as the formation of hydroxides. Modeling the coordination of lanthanide ions is further complicated in porous materials, where the conformational binding space is large, coupled with many possible chemical reactions. Atomic resolution is essential to determine the chemistry of lanthanides in porous materials, and *ab initio* molecular dynamics (AIMD) provides such resolution as well as the ability to account for the *f*-orbital chemistry. Furthermore, *ab initio* molecular dynamics provides the optimal scale to consider both reactivity and dynamics for a bulk system for zeolites.

The solution structure of the lanthanide aqua ions and their acidity constants were replicated to quantify the limits of the computational approach. The use of density functional theory (DFT) and *ab initio* molecular dynamics to quantify the solution structures and acidity constants of the lanthanide aqua ions enabled the simulations to be compared against an extensive collection of experimental findings. The solution structures of the lanthanide aqua ions were determined within ~0.05 Å from experiment, while the first acidity constants for all lanthanide elements were replicated within ~1.1 pK_a units. The *ab initio* molecular dynamics protocol, coupled with Bluemoon rare event

sampling, culminated in a thorough methodology to quantify structure and reactions of the lanthanides in the condensed phase, specifically in porous materials and in solution.

The molecular resolution of water molecules in hydrogen- and lanthanum-exchanged faujasite provided unique insights into the ambiguous mechanism of how lanthanum stabilizes the zeolite. The techniques utilized resulted in the ability to model in periodic conditions, account for reactions, and long-range electrostatic contributions, all of which allows for an in-depth examination of the phenom occurring in lanthanum-exchanged faujasite. Results point toward two general mechanisms by which lanthanum prevents water-mediated dealumination in faujasite: i) the increase in the Brønsted acidity of faujasite as a result of lanthanum exchange makes faujasite favor the deprotonated state, reducing the hydrophilicity of the aluminum tetrahedral sites; and ii) the preferred binding sites of both the lanthanum cation and water in sodalite hinders the access of water molecules to aluminum tetrahedra, inhibiting dealumination reactions.

Modeling liquid water in faujasite, with explicit water molecules, enabled resolving the local structure of water and changes within the structure due to confinement, hydrophilicity of faujasite, and the exchanged cation. The $O_{wat} - O_{wat}$ radial distribution function obtained from AIMD simulations quantify how the local structure of water changes in zeolitic confinement. In hydrogen-exchanged faujasite, the addition of liquid water results in the deprotonation of aluminum tetrahedra, which results in hydronium ions that cause disorder in the local structure of water. In the case of sodium- and lanthanum-exchanged faujasite, monovalent cations have an increased likelihood of occupying windows of the supercage, disrupting the local structure of water. The number

of exchanged cations had a more significant effect on the structure of confined water than the charge of the cations.

The study of zeolites as ion exchangers for rare earth elements requires an understanding of the selectivity of the zeolite, with the structure of confined water playing an important role. The ability to accurately model and predict structures and reactions that occur in the liquid phase, within rare earth-exchanged zeolites, provides a computational approach to study lanthanides in solution in porous confinement, with relevance to ion exchange-based separations for rare earth elements.